Microwave Kinetic Inductance Detectors for the Mid-Infrared

W.G. Ras

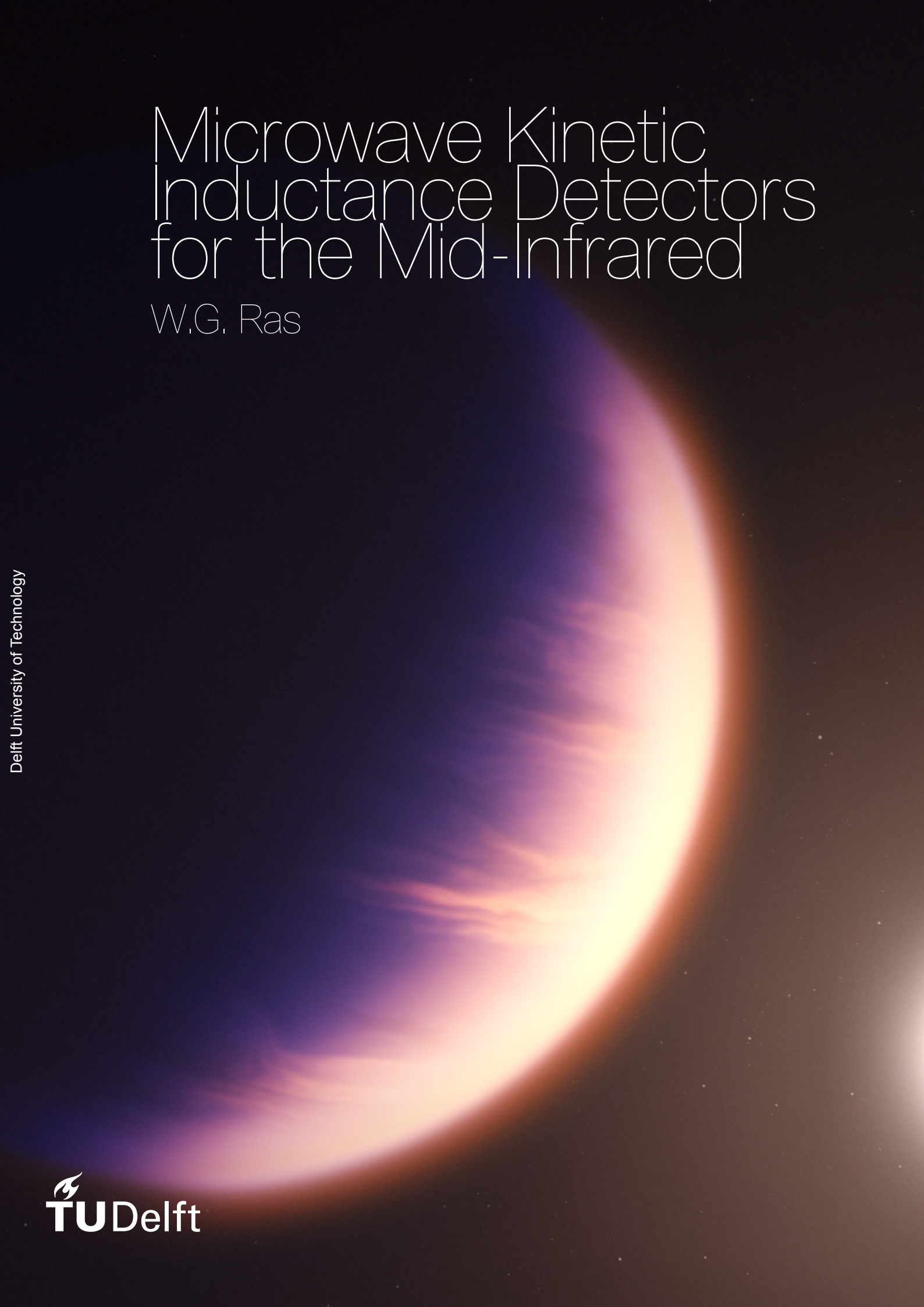

Delft University of Technology

TU Delft

Microwave Kinetic Inductance Detectors for the Mid-Infrared

by

W.G. Ras

to obtain the degree of Master of Science
at the Delft University of Technology,
to be defended publicly on Monday November 28, 2022 at 01:00 PM.

Student number:	4456572	
Project duration:	January 1, 2022 – November 28, 2022	
Thesis committee:	Prof. dr. ir. J.J.A. Baselmans,	TU Delft/SRON, supervisor
	Dr. P.J. de Visser,	SRON, supervisor
	Dr. A. Endo,	TU Delft
	Dr. A.F. Otte,	TU Delft
	Ir. K. Kouwenhoven,	TU Delft/SRON, daily supervisor

TU Delft

SRON

Preface

The Cavendish Laboratory in Cambridge is famous for many extraordinary discoveries in the late 19^{th} and early 20^{th} such as the electron and neutron. It has also laid the foundations for the discovery of quantum mechanics and the double-helix structure of the DNA molecule. If we could go back in time to the old Cavendish Lab we would see an inscription carved in Latin above the great oak door. Translated in English it said:

Great are the works of the Lord, studied by all who delight in them

The inscription was put there by the first Cavendish Professor, James Clark Maxwell. Maxwell was the first to show that electricity, magnetism and light are different manifestations of the same phenomenon which has become one of the most successful theories in the history of science. Many will recognise (and struggle to re-derive) the famous Maxwell equations derived by himself over 150 years ago. The inscription is a verse from the bible, Psalm 111:2. Just as Maxwell was reminded of these words before entering the lab, these words are placed at the beginning of the thesis as a reminder to me, and perhaps even to you. This thesis is in honour of the many great scientists that have gone before us and to the infinitely greater, Creator of All.

W.G. Ras
Delft, November 2022

Abstract

Today, one of the major goals of modern astronomy is the search for other habitable worlds and the presence of life on them. Crucial in this search is the atmospheric characterisation of small, rocky planets orbiting in the habitable zone around solar type stars. The LIFE initiative will be able to perform atmospheric characterisation of a sizeable subset of these planets in the mid-infrared (mid-IR) wavelength regime (5-20 μm). The mid-IR is an important bandwidth as it contains some important atmospheric biosignatures. Extremely sensitive and highly efficient detectors are required to detect the faint signal from these small exoplanets. Current state-of-the-art detectors based on semiconductor technology are unable to meet these requirements. Microwave Kinetic Inductance Detectors (MKIDs) are superconducting pair-breaking detectors able of single-photon detection with no readout noise or dark current. This makes MKIDs a promising candidate for mid-IR detectors for the LIFE initiative. In this thesis we investigate what development is necessary to meet the detector requirements set by the LIFE initiative. We also investigate how the performance of MKIDs can be reliably measured in the mid-IR.

Currently, there are no single-photon counting MKIDs designed for the mid-IR. Measurements are done with two MKID devices that originally have been designed for the near- and far-IR bandwidths. Prior to this work the near-IR detector has shown single-photon counting 1545 nm and the far-IR detector at 38 μm. In this work we show the single-photon counting ability of MKIDs 3.8 and 8.5 μm. This is the first time that single-photon counting has been shown at 8.5 μm. The resolving power ($E/\delta E$) at 8.5 μm is found to be about 4. Experiments are planned at 18.5 μm for which a setup has been designed with a cryogenic black-body radiator as the source. This is the longest wavelength required for the LIFE spectrometer.

We also perform an optimisation of the near-IR detector geometry to see if a realistic device can be made that is sufficiently sensitive to 18.5 μm radiation. The results show that a realistic design could in theory be made but this strongly depends on how the detector is limited by the noise.

Next steps are to design a dedicated MKID for the mid-IR to determine its efficiency and dark current. This will also require us to improve the current measurement setup as measurements show that we suffer from thermal background radiation which limits the detector performance.

Contents

1 Introduction

This thesis aims to research the performance of Microwave Kinetic Inductance Detectors (MKIDs) in the mid-infrared (mid-IR) wavelength regime. The mid-IR wavelength regime, which we define to be between 5-20 micrometers, is important for finding signs of life on earth-like exoplanets. Highly sensitive and efficient detectors are required for this purpose and a promising one is the MKID, which is a superconducting, pair-breaking detector. This provides the relevance of the work done in this thesis. The following section of this introductory chapter will give a more elaborate introduction to the exoplanet research in the mid-IR and the challenges that accompany it. In section 1.2, it is explained why the MKID is a promising detector for this application. In section 1.3 we look at the the challenges that we are faced with in the mid-IR with MKIDs. This chapter closes with the thesis outline.

1.1. Finding Habitable Worlds

Who knows for how long humans have looked up to the night sky wondering about their place in this universe and the possibility of life out there. For long, the question 'Are we alone?' has mainly been the area of philosophers and science fiction writers as no means existed to find an actual answer. However, this has changed in the last couple of decades as technology has advanced greatly allowing for revolutionary ground- and space-based observatories able to image across the wide electromagnetic spectrum of light with extreme sensitivity. Today, one of the major goals of modern astronomy is the search for other habitable worlds and the presence of life on them [1].

A key role in this search for life are exoplanets; planets orbiting stars other than the sun. Since the discovery of the first exoplanet by [2] in 1992, we have now discovered more than 5000 confirmed exoplanets [3] and more are added every week. In our search for life we look for earth-like planets orbiting sun-like stars since the earth is the only place in the universe where we know life to exist. These exo-earths, or terrestrial planets, are rocky, relatively small and orbit in the habitable zone of their host star. The habitable zone (HZ) is the range of distances to the star where liquid water can exist on the planets surface which is thought to be crucial for life. Our observational methods of the last 30 years have been biased towards finding mostly large exoplanets, close to their host star at distances too great to study them in more detail [4]. However, from statistical models is estimated that the prevalence of small planets around Sun-like stars is particularly frequent [5], [6]. We have even discovered extra-solar, planetary systems with multiple planets orbiting in the HZ of their host star, see 1.1 The James Webb Space Telescope or the upcoming Extremely Large Telescope, will increase our capabilities but will still not be able to detect these smaller planets in the HZ of their host star. New flagship mission concepts have been presented for the next decade that will be able to do this. These are the Habitable Exoplanet Observatory (HabEx) [7], Large UV/Optical/IR Surveyor (LUVOIR) [8] and Large Interferometry For Exoplanets (LIFE) [9]–[12]. The LIFE initiative is unique among these concepts as it aims to do atmospheric characterisation of large number of terrestrial exoplanets in the mid-IR, whereas LUVoIR and HabEx aim to do this in reflected light of the host star. The LIFE initiative requires detectors that are highly sensitive and have very low noise properties as the planet signal is extremely dim [10]. The current state-of-the-art detectors based semi-conducting technology are not expected to meet these demanding requirements, whereas the superconducting MKIDs have the

potential to do so. This is the motivation for the work in this thesis. In section 2.1 we will look more into the LIFE mission concept, the detector requirements that follow from it and how current detectors measure up to those requirements. In the next section we will explain the key differences between semiconducting detectors and MKIDs.

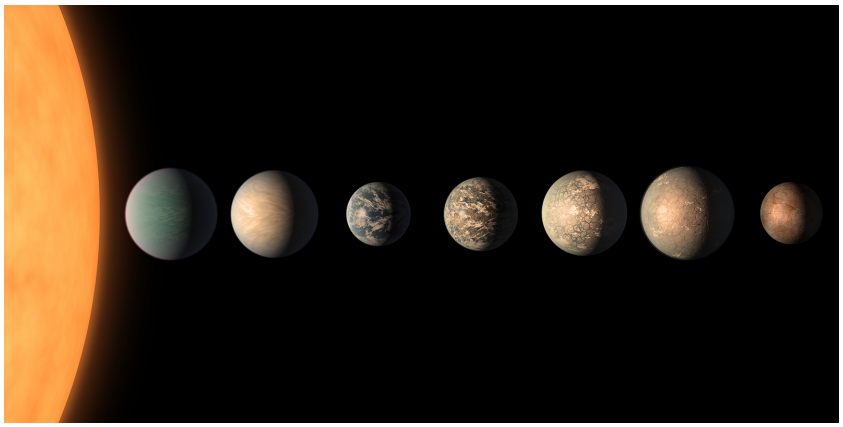

Figure 1.1: An artist's impression of the plenatary system orbiting Trappist-1. This is the largest extra-solar, planetary system discovered to this day. Some of these planets have orbits within the habitable zone (the zone where life might exist) of the host star. Extremely sensitive detectors are necessary to characterise the atmosphere of such planets in the thermal infrared [10].

1.2. Microwave Kinetic Inductance Detectors

Semiconducting detectors have been the standard in industry for the last decades. Their technology has matured greatly allowing for low noise, megapixel arrays to be used for various astronomical purposes. Semiconducting detectors are based on the creation of electron-hole pairs by absorbed photons that excite electrons from the valence to the conduction band, see 1.2a. The excitation energy necessary is equal to the bandgap energy of the semiconducting material, which is typically 1 eV. In an array of such detectors, the excited electrons are captured per pixel during a certain exposure time, building up charge which can be digitized and readout per detector. Semiconductors, however, have a major downside: the gap energy is high. This means that most photons above the gap energy can only excite one electron. This has three implications: firstly, photons that have an energy lower than the gap energy cannot be detected. Secondly, the detector cannot distinguish between photons with different energies, as all photons will only excite a single electron. Lastly, an excitation arising from inherent detector noise (dark current) cannot be distinguished from an excitation by an absorbed photon. In other words, a semiconducting detector is colour blind, is only sensitive to high-energetic photons and is effected by dark current.

MKIDs are different, making use of superconducting materials. Superconductors behave as normal conductors except when they are cooled below a certain critical temperature, which is typically only a few degrees above absolute zero. Below this point the electrons pair up in so-called Cooper pairs and the normal state resistance drops to zero, hence the name superconductor. Incident photons can break up the Cooper pairs and increase the kinetic inductance and with that the complex impedance of the superconductor, see 1.2. This change is rather small, but gives a large response if the superconductor is embedded as a variable inductor in a microwave resonator circuit. The big difference with semiconductor detectors is that the binding energy, that needs to be overcome in order to break up the Cooper pairs, is of the order 1 meV, which means that the same photon can break thousands of Cooper pairs in a superconductor instead of just exciting a single electron in a semiconductor. This makes a superconducting detector able to detect photons with much lower energies, longer wavelengths, than a semiconducting detector; up to the mm wavelengths. Pair-breaking detectors are also energy resolving, i.e. they see colour, as photons with different energies give rise to a different response.

Furthermore, because of the low temperature at which these MKIDs operate, the noise levels within the detector are very low, much lower than the signal a single photon would produce. This effectively leads to MKIDs having zero dark current and read noise. And last but not least, due to the inherent detector design, MKIDs can be easily configured into large detector arrays and be read-out without

adding much complexity to the system architecture. This multiplexing ability of MKIDs is a great advantage when compared to other types superconducting detectors.

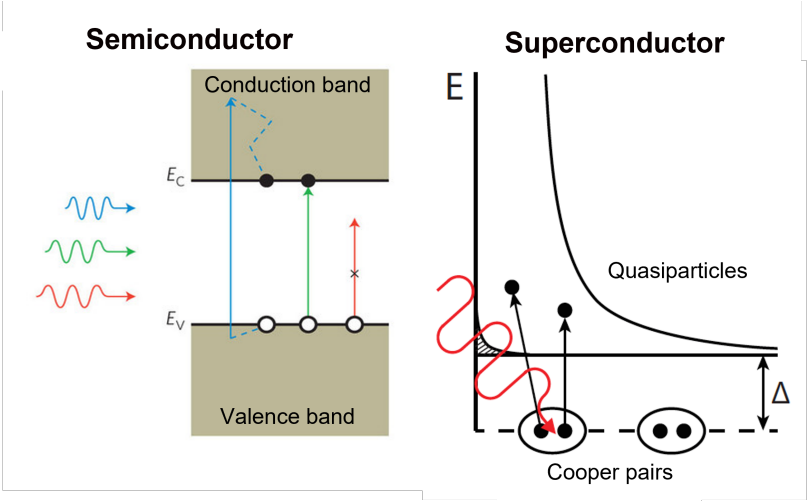

Figure 1.2: Schematic overview of the fundamental difference between semi- and superconductors. The semiconductor has a bandgap energy in the order of 1 eV and every high energetic photon can only excite 1 electron from the valence to the conduction band. In a superconductor electrons pair up in Cooper pairs with a binding energy that is about a thousand times lower than the bandgap energy of a semiconductor. The same incident photon will therefore break order thousand more Cooper pairs than it will excite electrons in an semiconductor. Superconducting detectors have no readout noise and have the potential to have zero dark current; both of which are limitations to the performance of semiconducting detectors.

1.3. Closing the Mid-IR gap

As of today, a great variety of MKIDs have been developed both at wavelengths longer (mm/sub-mm:[13], [14] far-IR:[15], [16]), and shorter (optical/near-IR:[17]–[21]) than the mid-IR, but there has not been much development within the mid-IR. The key difference in these two regimes is how radiation is coupled to the detector: long wavelength radiation can be coupled to the detector using antennas, while short wavelength radiation cannot, since the antenna structure, which has a characteristic dimension in the order of the wavelength, would become too small to manufacture with our current methods[22]. Instead, optical MKIDs are directly coupled to free space, or in other words, they have an absorber design. Other general differences are that (sub-)mm MKIDs are often photon-integrating detectors and have distributed resonators, whereas optical MKIDs are single-photon counting detectors and have lumped element resonators. An MKID was actually developed in the mid-IR, at 10μm, [23], but as a photon-integrating detector, whereas we want to develop a single-photon counting for the mid-IR. In the mid-IR it is uncertain what general MKID design would work best and it might very well be that different designs are necessary to cover the complete mid-IR bandwidth. In this thesis we perform measurements with two different devices developed in the Terahertz Sensing group to investigate their performance in the mid-IR. The devices are the near-IR LEKID [18] and a far-IR MKID[16], both are seen in Figure 1.3 and are further explained in chapter 6 and chapter 7 respectively. The far-IR MKID is an antenna-coupled device, optimised as a photon integrating detector at 200 μm, but but this design property

Key parameters in the performance of MKIDs are their response, sensitivity and optical efficiency. The single-photon response of a MKID scales with the energy of the photon: the lower the energy, the lower the response. The far-IR MKID is designed as a photon-integrating at 200μm, but it starts to show single-photon detection at 38μm [24]. As the response will only increase for the more energetic, mid-IR photons, it is very likely that it will be able to do single-photon detection across the mid-IR. This will be harder for the near-IR LEKID as its response will decrease for longer wavelengths. The near-IR LEKID must make up a factor 20 decrease in photon energy to detect single photons up to 20μm, whereas it will be a factor 8 increase for the far-IR MKID to detect single photons all the way down at 5μm. On the other hand, the optical efficiency of the far-IR MKID is expected to be very low

because the the antenna is of no use in the mid-IR and it has a highly reflective, aluminium inductor, while the near-IR LEKID has a β-Ta inductor that couples better to free space. Lastly, the far-IR MKID is extremely sensitive because of several dedicated design choices to reduce the noise, for example by using an interdigitated capacitor (IDC) with very wide structures and by suspending the inductor on a phonon capturing membrane (why this reduces noise can be read in section 3.4). However, the far-IR MKID is not a realistic detector design for imaging arrays because of its large dimensions, but it could still be used in spectrometer applications that have less strict requirements for the dimensions of the detector.

As the reader can tell, the race has not been won by neither the near- nor the far-IR design. To cover the mid-IR bandwidth the best of both designs might have to be combined. The main research question of this thesis is as following: how do the near- and far-IR MKIDs perform in the mid-IR and what developments are still necessary to design a MKID spectrometer for the LIFE initiative? An immediate question is then: how do we measure the performance of MKIDs across the mid-IR? MKIDs are extremely sensitive, cryogenic detectors, and require a highly characterised, cryogenic setup and a well defined source. This is extra challenging in the mid-IR, as everything with a finite temperature emits mid-IR radiation. Therefore, additional goals of this thesis are: develop an experimental setup that can accurately measure the performance of the MKIDs in the mid-IR and devise a theoretical model to characterise the measurement setup.

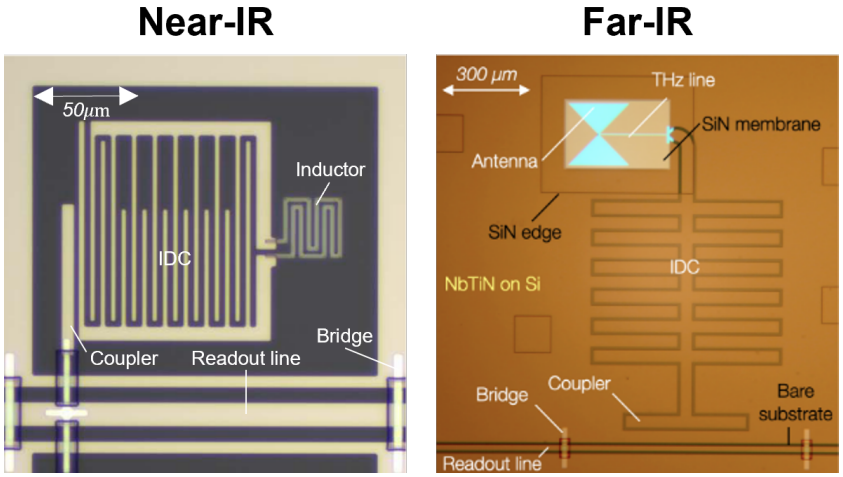

Figure 1.3: Illustrations of the the near-IR and far-IR MKIDs that are investigated in this thesis as they have proven single-photon detection closest to the mid-IR regime. Their performance in the mid-IR is unknown and this will be investigated in the remainder of this thesis. The near-IR LEKID is a lens coupled, lumped element MKID with a NbTiN interdigitated capacitor (IDC) and a β-Ta inductor. Single-photon detection has been demonstrated with this device up to 1545nm[18]. The far-IR MKID is designed as a photon-integrating detector at 200μm [16], but it also has shown single-photon detection at 38μm [24]. It combines a leaky-slot antenna with a lens to effectively couple THz radiation to the Al inductor (THz line). The antenna does not work in the mid-IR making the THz line the effective absorber for radiation. The device is ultra-sensitive to THz radiation because it has a large, NbTiN IDC and has its inductor suspended on a thin, SiN membrane to reduce phonon loss, similar to [17].

1.4. Thesis Outline

This thesis is structured as following. In Chapter 2 we explore the LIFE initiative and distill the requirements that it poses on the detectors. We also investigate how current state-of-the-art detectors measure up to these requirements. In Chapter 3 we provide the reader with the relevant theoretical background on superconductivity, kinetic inductance and microwave resonators; topics that are crucial to understand the working principle of MKIDs and how its performance is measured and affected. In Chapter 4 we present the different experimental setups that will be used in the experiments and a theoretical model that is used to characterise the setups. Chapter 5 explains how we analyse the data from our measurements. Chapter 6 and 7 present the results from measurements with the near-IR LEKID and far-IR MKID respectively. In Chapter 8 optimisation is performed to design a LEKID at 18.5 μm. We conclude with a discussion of the results and recommendations for future work.

2

Thermal Spectroscopy in the Mid-IR

2.1. Large Interferometery For Exoplanets (LIFE)

The LIFE initiative aims to perform atmospheric characterization of dozens of terrestrial planets in the mid-infrared to help answer the big, scientific questions about the development and existence of life on Earth and other planets. The MKIDs, that are the subject of this thesis, are a very promising solution for the stringent detector requirements coming forth from this mission objective. This chapter will first explain the LIFE initiative and its relevancy. Then, the detector requirements are discussed that arise from the objectives set by the LIFE initiative. Lastly, we will look at how state-of-the-art detectors using semi-conducting technology measure up to these requirements.

Exoplanet spectroscopy

Atmospheric characterization means to perform spectroscopy on light that has propagated through the atmosphere. The molecular composition of the atmosphere can be determined from the absorption lines present in the spectrum. Certain molecules or combinations of molecules are designated as atmospheric biosignatures, they indicate the presence of biological activity. Detecting these biosignatures is the objective of exoplanet spectroscopy.

Two very distinct categories can be distinguished in exoplanet spectroscopy: direct and indirect spectroscopy, see 2.1.Indirect spectroscopy makes use of the light of the host star that is transmitted through the atmosphere when the planet transits in front of the star. This method is heavily biased towards planets that block a lot of starlight and transit (frequently). With direct spectroscopy the planet can be observed outside of its transit. This is possible by suppressing the starlight, reducing the star planet contrast. A larger set of exoplanets can be studied using direct spectroscopy as there are more planets that do not have a transiting orbit than ones that do. To put this in perspective, we now have 5000+ confirmed exoplanets of which the majority has been discovered in transit and only 20-25 of them have been directly imaged. However, even though their low numbers, the directly imaged planets constitute a significant part of the 175 planets that we have spectroscopic data from [25]. Direct spectroscopy can be done with either the reflected starlight or with the planets thermal emission.

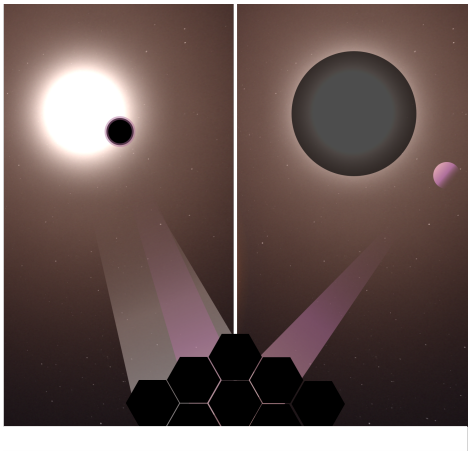

Figure 2.1: Illustration of the different between (left) direct and (right) indirect spectroscopy. Indirect spectroscopy used the light of the host star that is transmitted through the atmosphere when the exoplanet transits in front of the star. In direct spectroscopy the starlight is suppressed, improving the star-planet contrast, such that the planet can be observed outside of transit. Direct spectroscopy can be done with either the reflected starlight or with the planets thermal emission.

Thermal spectroscopy

Earth-like planets emit most of their radiation in the mid-IR regime. The LIFE initiative focuses on the mid-IR because it is particularly rich in molecular absorption bands of the main constituents of terrestrial exoplanet atmospheres and also contains several strong biosignatures not present in the optical regime, see Figure 2.2a and also puts more direct constraints on the planet's effective temperature and radius[9]. An additional advantage is that the star-to-planet contrast ratio is much more favourable in the mid-infrared as compared to the optical regime, see Figure 2.2b.

The thermal emission for a black body is given by Planck's radiation law, which is dependent on the wavelength and the temperature of the object. Generally, objects with higher temperatures emit radiation at shorter wavelengths. The black body emission of a sun-like star (T=6000 K) peaks at $\lambda \approx 0.5\ \mu$m whereas the emission of a earth-like planet (T=260 K) peaks at $\lambda \approx 10\ \mu$m. The contrast ratio therefore can be a factor 1000 better in the mid-infrared as compared to the optical regime. However, the mid-infrared also brings two challenges. Firstly, a much (optically) larger telescope is required to obtain the same spatial resolution at longer wavelengths. The spatial resolution of a telescope is fundamentally limited by diffraction and scales in that case as $\theta \propto \lambda/D$ with θ is the spatial resolution and D the aperture diameter. This means that at λ=10 μm (mid-IR) the telescope needs to be a factor 40 larger than at λ=0.5 μm (optical) to obtain the same resolution. Secondly, the mid-infrared is challenging because the telescope and instruments also emit thermal radiation which increases the background noise. The telescope and instruments should therefore be cooled more than necessary in the optical regime.

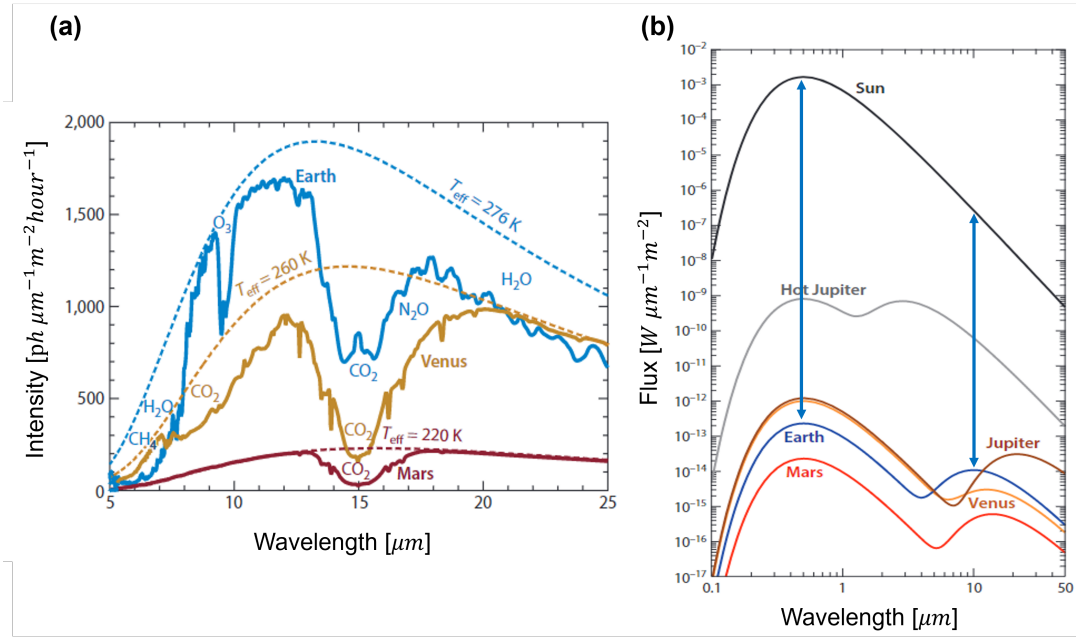

Figure 2.2: (a) (solid) Spectra of Earth, Venus, and Mars at a spectral resolution ($\lambda/\Delta\lambda$) of 100 in the thermal emission spectrum of the planets and (dotted) black-body emission of a planet of the same radius at the maximum brightness temperature of the spectrum. The presence of important biosignatures is seen, like ozone (O_3), methane (CH_4) and nitrous oxide (N_2O). [26], [27]. (b) Absolute flux comparison of Jupiter, Venus, Earth, and Mars in our Solar System as well as a hot extrasolar giant planet (hot jupiter) shown here as black-bodies for the Sun at a distance of 10 pc on a log-logscale, assuming constant reflectivity and temperature. The two dark blue arrows indicate the star-planet contrast at 0.5 and 10 μm. The star-planet contrast is an order 1000 lower in the mid-IR. Images are adapted from [27]

Interferometry

The LIFE initiative will use formation-flying interferometry for two purposes: to obtain the desired spatial resolution and star-planet contrast in the mid-IR, see Figure 2.3. This was already thought of back in 1978 [28] and has been seriously researched for ESA's Darwin and NASA's TPF-I concepts from the early/mid 2000s. However, these did not move forward as technology was not sufficiently advanced and our knowledge of the exoplanet population was insufficient to construct proper models for the estimated detection yields. Today, as technology has advanced and our exoplanet archive has grown,

the concept of formation-flying interferometry should be re-assessed [9].

The simplest configuration of an interferometer combines the signals of two collector apertures separated by a distance, called the baseline, b, see 2.3. When the signal arrives coherently (having the same phase) at both apertures, the response of the instrument will give a sinusoidal fringe pattern with spacing λ/b, as projected on the plane of the sky. When a π phase shift is applied on one of the signals, the centre of the response will destructively interfere and can thus be used to null the star's light. The 'spatial resolution' of an interferometer is thus determined by the baseline and not by the diameter of the collecting apertures. As the baseline generally is much larger than the diameter of a single-aperture telescope, interferometry can obtain lower spatial resolutions. Furthermore, the baseline can also be re-configured in-flight to meet the required spatial resolution. The interference pattern obtained is related to the spatial image by the 2D Fourier transform. The coverage in the Fourier plane, also called uv plane, and thereby of the image plane, can be increased by rotating the interferometer around its line of sight, by adding more baselines to the configuration and/or by performing multi-wavelength observations.

LIFE envisions an X-array configuration with four collector spacecraft and a combiner spacecraft in the middle, flying perpendicular to the line of sight. Having four collecting spacecraft in a rectangle removes the $180°$ ambiguity of the planets position that exists when having only two collecting apertures and also allows for having a 'nulling' and 'imaging' baseline that can be optimized separately.[10]

Scientific output

The most important scientific output of the LIFE initiative is the number of potential habitable worlds detected in our stellar neighbourhood, meaning small, rocky planets in the habitable zone of main sequence stars within 20 parsec of our sun.

LIFE defines an initial search phase of 2.5 years and estimates, depending on the observing scenario, that an interferometer consisting of four 2 m apertures covering a wavelength range between 4 and 18.5 μm could detect about 25–45 habitable worlds and about 550 exoplanets total [9]. This is similar to the estimates of the reflected light missions HabEx and LUVOIR. For comparison, the JWST will be able to obtain spectroscopic data in the mid-infrared from only a handful of potentially habitable exoplanets. This shows that the LIFE initiative is important for obtaining a statistically relevant sample of potentially habitable exoplanets.

2.2. Detector requirements

Even if we can do high-precision formation flying, achieve a good star-planet contrast and have sufficient spatial resolution, we still need to detect the planet signal. We investigate the requirements posed on these mid-IR detectors based on the LIFE initiative. We also look into how the state-of-the-art mid-IR detectors today measure up to these requirements.

Quantum efficiency, dark current, and readout noise are the three most important parameters that describe high performance detectors. The requirements for these parameters following from the LIFE initiative are compared to the state-of-the-art detectors of today. Figure 2.4 shows us the wavelength dependent noise contributions for the observation of an Earth-twin located at 10 pc with LIFE in the baseline scenario where a optical efficiency of 70% was assumed. In panel (a) the contributions of three fundamental, background noise sources are plotted against wavelength which, when added up, give a total noise contribution of $<10^{-1}$ photons/s. The dark current requirement of the detector is given in panel (b) where we obtain a constant value of about 10^{-2} photons/s[1] across the whole bandwidth. Furthermore, the planet signal is obtained from panel (c) and gives a contribution of $<10^{-1}$ photons/s. Nothing explicit is mentioned in [10] about the readout noise of the detectors, but it should not dominate the contributions from the fundamental noise sources. Therefore, as a safe estimate, we set the readout noise equal to the dark current: $<10^{-2}$ photons/s.

There are two general types of detectors available for the mid-infrared. The first uses Mercury Cadmium Telluride (HgCdTe). HgCdTe achieves the highest optical efficiency and lowest dark current of any infrared detector material[29]. By changing the ratio of mercury to cadmium, the bandgap energy, and therefore cutoff wavelength can be tuned to the desired value. HgCdTe detector are for example used in the JWST and will be used in the RST (f.k.a WFIRST) and ELT/METIS, however only for

[1] Normally, the dark current is given as e^-/s, but here we follow the notation of the [10].

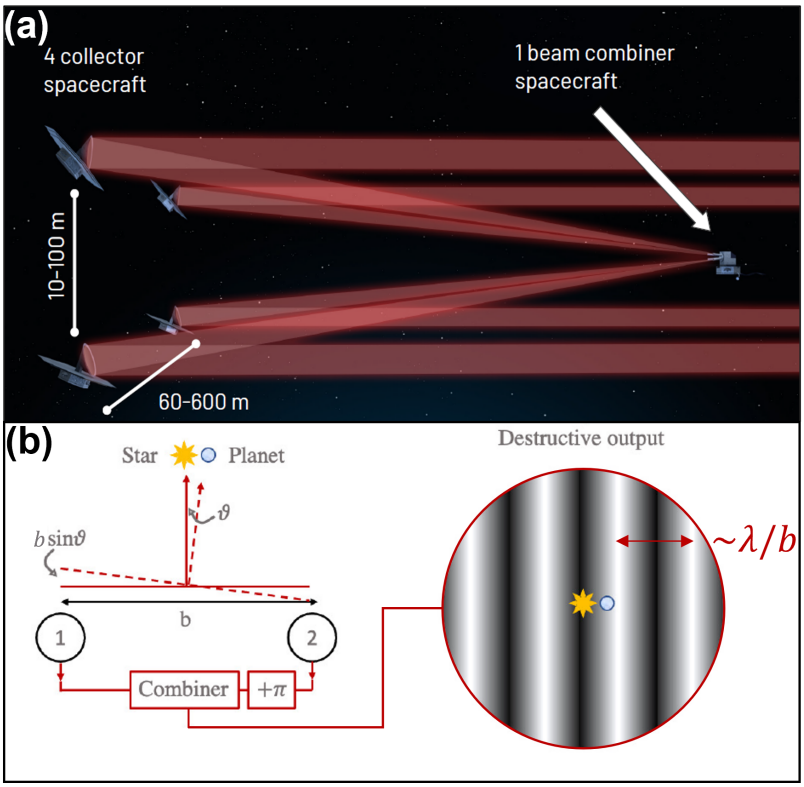

Figure 2.3: (a) Artist illustration of the LIFE concept. The four collector and beam combiner spacecrafts are seen in a X-array configuration, perpendicular to the line of sight. The two baselines can be optimised separately. [credit: LIFE initiative] (b) A schematic overview of interferometric nulling with a single baseline. The signal received from the star and planet differ in phase as the planet is slightly off centre. Combining both signals with a π phase shift difference will result in a sinusoidal fringe pattern with spacing λ/b, as projected on the plane of the sky.

wavelengths up to $5\ \mu$m. For longer wavelengths another detector type is preferred which is the arsenic-doped Silicon (As:Si) impurity-band conduction (IBC) detector, which has a longer wavelengths cutoff (28 μm, [30]) than the HgCdTe. As:Si IBC detectors are used in the JWST/MIRI and will be used in the ELT/METIS instruments to cover the mid-infrared regime. Let us now compare the detector performance of these HgCdTe and As:Si IBC detectors to the requirements following from the LIFE initiative. The results are listed inTable 2.1

The HgCdTe detectors cannot cover the whole LIFE wavelength range. Even for <10 μm their dark current is a factor 10 more than for the As:Si IBC detectors. As:Si IBC detectors are the only real alternative for the mid-infrared. The dark current in the order of 10^{-2} e^-/s might eventually meet the LIFE requirements in the future. The same holds for the optical efficiency. However, the readout noise will dominate the total fundamental background noise and planet signal.

MKIDs are a promising solution to the stringent requirements that LIFE poses on the detector performance as they have no readout noise and potentially no dark current. Yet, no MKIDs exist yet for the mid-infrared regime, and therefore, in the remaining of this thesis, experiments and simulations are done to investigate the performance of MKIDs across the mid-infrared. In chapter 9 we compare our results to the LIFE requirements in column 1 of Table 2.1.

Table 2.1: Overview of the LIFE detector requirements and the performance of state-of-the art mid-infrared detectors based on semiconducting technology.

	LIFE$^{(a)}$ [10]	HgCdTe [31]	Si:As IBC$^{(b)}$ [32]
Wavelength range [μm]	4-18.5	1-16	<28
Optical efficiency [%]	70	>55	>50 (<19 μm), >60 (12-24 μm)
Dark current [e$^-$/s]	0.01	<0.3$^{(c)}$ (<10 μm, [33]), <1$^{(d)}$ (∼15 μm, [34])	0.03$^{(e)}$ (<19 μm), 0.17$^{(e)}$ (12-27 μm)
Readout noise [e^-]	0.01$^{(f)}$	12-18	14$^{(g)}$

Notes: (a) Requirements for the observation of an Earth-twin located at 10 pc with LIFE in the baseline scenario. (b) Data obtained is obtained for short wavelength (SW) and long wavelength (LW) part of the IFU spectrometer in JSWT/MIRI. (c) Measured at T=40 K. (d) Measured at T=28 K. (e) Measured at T =7.2 K. (f) [10] does not mention a specific readout noise. As a safe estimate we set it equal to the dark current. (g) This value is not actually measured but is expected to be of this magnitude [32].

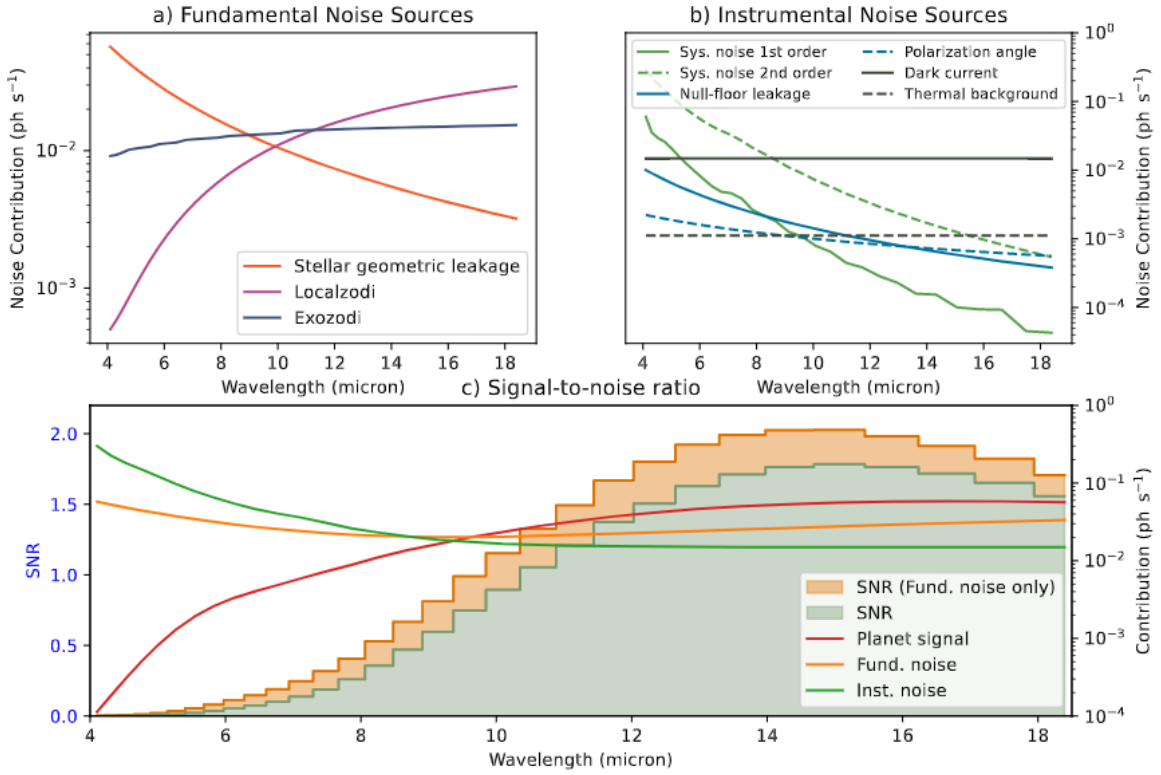

Figure 2.4: Noise and signal contributions across the mid-infrared regime for an observation of an Earth-twin located at 10 pc with LIFE in the baseline scenario. (a) Noise sources due to background radiation. (b) Instrumental noise sources split into systematic noise sources(green) and additional photon noise sources arising from instrumental effects. (c) Planet signal, fundamental noise and instrumental noise contributions resulting in a wavelength dependent SNR for the (orange bars) fundamental noise limited scenario and (green bars) complete scenario. The spectral resolution ($\lambda/\Delta\lambda$) is 20. [figure from [10]]

3

Microwave Kinetic Inductance Detectors

In section 1.2 and 1.3 the (lumped element)kinetic inductance detector has been briefly explained for the relevance of this thesis. In this chapter a more detailed and mathematical description is provided. Firstly, superconductivity and kinetic inductance is explained, which is the fundamental phenomenon on which these KIDs operate. Secondly, the working principal of microwave resonators is explained and how a response is obtained from a KID. Thirdly, we will discuss the limitations to this responsivity.

3.1. Superconductivity

If a conductor is cooled below its critical temperature T_c its resistance drops to zero for DC currents and it becomes superconducting. The mechanism behind this phenomenon is that the electrons in the superconductor, being fermions, pair up to form a new bound state which is energetically favourable as the electron-phonon interaction is stronger than the effective Coulomb force between the electrons. These so-called Cooper pairs can now be considered as bosons, all occupying the same state. A finite energy is necessary to break up a Cooper pair which is given by $\Delta \approx 1.76 k_B T_C$ with k_B the Boltzmann constant and with 2Δ being the binding energy of a single Cooper pair. Δ is much smaller than the bandgap energy of a semiconductor giving rise to the advantages of superconductors over semiconductors mentioned in section 1.2.

When a Cooper pair absorbs energy higher than its binding energy it is split up into two quasiparticles. These quasiparticles are fermions in nature, but can be electron-like or hole-like or a mixture of the two. Vibrations in the lattice due to the finite temperature, also called phonons, can have energies exceeding the binding energy of the Cooper pairs. A thermal distribution of quasiparticles therefore exists in the superconductor that depends on the temperature T. If $k_B T \ll \Delta$ the quasiparticle density within the superconductor can be approximated by

$$n_{qp} \approx 2N_0\sqrt{2\pi k_B T \Delta}\, \exp(-\Delta/k_B T) \tag{3.1}$$

where N_0 is the single-spin density of states at the Fermi surface. The total number of quasiparticles is then given by $N_{qp} = n_{qp} V$ with V the volume.

As phonons continuously break Cooper pairs into quasiparticles, they also recombine into Cooper pairs as the system tends towards the lowest energy state. The time scale related to this process is the recombination time and can be described by

$$\tau_{qp} = \frac{\tau_0}{n_{qp}} \frac{N_0 (k_B T_c)^3}{2\Delta^2} \tag{3.2}$$

which is valid for quasiparticles at the gap edge ($E = \Delta$) in a thermal distribution where $T \ll T_c$. τ_{qp} is inversely related to n_{qp}, thus the recombination time is shorter if there are more quasiparticles present in the superconductor.

This random generation and recombination of quasiparticles gives rise to a noise mechanism intrinsic to the detector: the generation-recombination noise (GR-noise).This noise is present even when no

radiation is incident on the detector. More on this in section section 3.4. The conductivity of the superconductor in the presence of both Cooper pairs and quasiparticles is often described with the two-fluid model using the complex conductivity, $\sigma = \sigma_1 - i\sigma_2$, where the real part, σ_1, governs the conductivity of the normal electrons, which is finite for AC currents, whereas the complex part, σ_2, governs the conductivity of the Cooper pairs. Expressions for σ_1 and σ_2 have been found by Mattis and Bardeen [35], [36]. The change in σ_1 and σ_2 upon a change in quasiparticle density, $d\sigma/dn_{qp}$, is given by [36]

$$\frac{d\sigma_1}{dn_{qp}} \approx \sigma_N \frac{1}{N_0 \hbar\omega}\sqrt{\frac{2\Delta_0}{\pi k_B T}}\sinh\left(\frac{\hbar\omega}{2k_B T}\right) K_0\left(\frac{\hbar\omega}{2k_B T}\right) \tag{3.3}$$

$$\frac{d\sigma_2}{dn_{qp}} \approx \sigma_N \frac{-\pi}{2N_0 \hbar\omega}\left[1 + 2\sqrt{\frac{2\Delta_0}{\pi k_B T}}\exp\left(\frac{-\hbar\omega}{2k_B T}\right) I_0\left(\frac{\hbar\omega}{2k_B T}\right)\right] \tag{3.4}$$

with σ_N the normal state conductivity, $\hbar$ the reduced Planck's constant and ω the angular frequency of the AC field. $I_0(x)$ and $K_0(x)$ are the modified Bessel functions of the first and second kind. Raising the temperature of the superconductor will increase the thermal quasiparticle density, but the absorption of pair breaking radiation does so as well. A continuous radiation power incident on the detector P_{rad} will create a number of quasiparticles N_{qp}^{rad} as given by

$$N_{qp}^{rad} = \frac{\eta_{pb}\eta_{opt}\tau_{qp}P_{rad}}{\Delta} \tag{3.5}$$

with η_{opt} the optical efficiency and η_{qp} the pair-breaking efficiency. η_{opt} is the ratio of the power absorbed in the sensitive part of the detector P_{abs} with respect to P_{rad}. η_{pb} reflects the ratio of the the absorbed power that is converted into the generation of quasiparticles with respect to P_{abs}.

It has been experimentally verified that the change to the complex conductivity due to pair-breaking radiation can also be approximated by a thermal distribution at an effective temperature [36]. We now have a better understanding of Cooper pairs, quasiparticle densities and the complex conductivity. The question now is: how can this be made into a detector for radiation? Three key elements necessary will be discussed in the following sections: kinetic inductance, microwave resonators and the responsivity.

3.2. Kinetic Inductance

We turn to something that is more easily probed experimentally: the complex surface impedance $Z_s = R_s + jX_s$, with R_s the surface resistance and X_s the surface reactance. Cooper pairs are accelerated without experiencing any resistance if a voltage is applied across the superconductor. The Cooper pairs gain kinetic energy and cannot be accelerated in opposite direction instantaneously because of their inertia. If an AC current is applied the superconductor it effectively acts like an inductor, where the current lags the voltage because of the kinetic energy of the Cooper pairs. This is called the Kinetic Inductance of the superconductor, L_k, also expressed as the surface inductance, L_s, in Z_s. The surface impedance in the dirty limit, where the superconducting coherence length ξ is much smaller than the penetration depth ($\xi \ll \lambda$), is given by [37]

$$Z_s = \sqrt{\frac{j\mu_0\omega}{\sigma_1 - \sigma_2}}\coth\left(\frac{d}{\lambda}\sqrt{1 + j\frac{\sigma_1}{\sigma_2}}\right) \tag{3.6}$$

with d the thickness of the film, μ_0 the magnetic permeability of vacuum. In the low temperature regime, $\sigma_2 \gg \sigma_1$, the following expressions for the surface resistance and inductance are obtained

$$R_s = \mu_0\omega\beta\lambda\frac{\sigma_1}{\sigma_2}\coth\left(\frac{d}{\lambda}\right) \tag{3.7}$$

$$L_s = \sqrt{\frac{\mu_0}{\omega\sigma_2}} = \mu_0\lambda\coth\left(\frac{d}{\lambda}\right) \tag{3.8}$$

The complex surface impedance now reads $Z_s = R_s + j\omega L_s$ and is dependent on the complex conductivity. Pair-breaking radiation changes the complex conductivity of the superconductor. This change in Z_s is rather small but can be converted into a detectable response by embedding the superconductor in a microwave resonator circuit.

3.3. Microwave Resonators

The response of the superconductor to pair-breaking radiation can be readout by embedding the superconductor as a variable inductor in a high quality, microwave resonator circuit, see Figure 3.1a+b. The AC probe signal with angular frequency ω_{AC} travels through the coplanar waveguide (CPW) and is capacitively coupled into a parallel resonator circuit with capacitance C, resistance R and inductance L. The CPW has an characteristic impedance of Z_0. The resonance frequency of the parallel RCL circuit is given as

$$\omega_0 = \frac{1}{\sqrt{LC}} \tag{3.9}$$

A change in inductance will cause a change in resonance frequency of the circuit. The resonator quality factor Q described the total power lost in the resonator per cycle with respect to the total power stored

$$Q = \frac{\omega E_{stored}}{P_{loss}} \tag{3.10}$$

This means that, if Q is high, the losses are low. The power in the resonator is either lost through the coupling with the transmission line, which can be described by its own quality factor Q_c, or through internal dissipation, described by Q_i. They relate to Q as following:

$$\frac{1}{Q} = \frac{1}{Q_i} + \frac{1}{Q_c} \tag{3.11}$$

The internal quality factor of the resonator, Q_i, is given by [35]

$$Q_i = \frac{\omega L}{R} = \frac{1}{\alpha_k}\frac{\omega L_s}{R_s} = \frac{2}{\alpha_k \beta}\frac{\sigma_2}{\sigma_1} \tag{3.12}$$

with $\alpha_k = L_k/L$, as the fraction of the kinetic inductance tot the total inductance, and the geometric factor $\beta = 1 + \frac{2d/\lambda}{\sinh(2d/\lambda)}$, which is 1 in the bulk limit ($d \gg \lambda$) and 2 in the thin film limit ($d \ll \lambda$). The effect of pair-breaking on Q_i is visible in its dependence on σ_1 and σ_2. An expression for a change in Q_i, δQ_i, is then found as

$$\frac{\delta Q_i}{Q_i} \approx -\frac{\delta \sigma_1}{\sigma_1} \tag{3.13}$$

where we have used the fact that $\delta\sigma_1 \gg \delta\sigma_2$ for $T \ll T_c$. The effect of pair-breaking on the resonance frequency can be quantified using a small frequency shift, $\delta\omega_0 = \omega_{AC} - \omega_0$, which gives

$$\frac{\delta \omega_0}{\omega_0} = \frac{\alpha_k \beta}{4}\frac{\delta \sigma_2}{\sigma_2} \tag{3.14}$$

The resonator response to pair-breaking is thus visible both in a change in resonance frequency and a change in the internal losses of the resonator. Now we want transform these to a more convenient set of responses; the phase, θ, and amplitude, A, relative to the resonance circle in the complex plane. We derive these in the following. The circuit can be analysed as a two-port network with the forward scattering parameter between ports 1 and 2 as:

$$S_{21} = \frac{2}{2 + Z_0/Z_{in}} = \frac{Q/Q_i + 2jQ\frac{\delta\omega_0}{\omega_0}}{1 + 2jQ\frac{\delta\omega_0}{\omega_0}} \tag{3.15}$$

If ω_{AC} is swept from below the resonance frequency to above, S_{21} traces a circle in complex plane in clockwise directions. The transmission is minimal at resonance, equalling to $S_{21,\min} = Q/Q_i$, which happens at at if $\omega_{AC} = \omega_0$. The centre point of the resonance circle lies at x_c=$(1 + S_{21,\min})/2$. In the in the limits of $\omega_{AC} \to \pm\infty$, no power is coupled in the resonator as $S_{21} \to 1$. The real and imaginary parts of S_{21} are given by

$$\mathrm{Re}(S_{21}) = \frac{S_{21,\min}^2 + 4Q^2(\frac{\delta\omega_0}{\omega_0})^2}{1 + 4Q^2(\frac{\delta\omega_0}{\omega_0})^2} \approx \frac{Q}{Q_i} \tag{3.16}$$

$$\mathrm{Im}(S_{21}) = \frac{2Q\frac{\delta\omega_0}{\omega_0}(1 - S_{21,\min})}{1 + 4Q^2(\frac{\delta\omega_0}{\omega_0})^2} \approx 2Q\frac{\delta\omega_0}{\omega_0}(1 - \frac{Q}{Q_i}) \tag{3.17}$$

where the approximation is to the first non-zero order in $\delta\omega_0/\omega_0$. The magnitude of S_{21} is then given by

$$|S_{21}|^2 = \frac{Q^2/Q_i^2 + 4Q^2(\frac{\delta\omega_0}{\omega_0})^2}{1 + 4Q^2(\frac{\delta\omega_0}{\omega_0})^2} = 1 + \frac{S_{21,\min}^2 - 1}{1 + 4Q^2(\frac{\delta\omega_0}{\omega_0})^2} \tag{3.18}$$

The phase and amplitude response of the resonator are given by $\theta' = \arg(S_{21})$ and $A = |S_{21}|$ respectively. For convenience we do transformation and map the resonance circle onto the unit circle and measure the response in θ from the negative real axis, giving

$$\theta = \pi - \theta' = \tan^{-1}\left(\frac{\mathrm{Im}(S_{21})}{x_c - \mathrm{Re}(S_{21})}\right) \tag{3.19}$$

The response in amplitude A is given as

$$A = \frac{\sqrt{(\mathrm{Re}(S_{21}) - x_c)^2 + \mathrm{Im}(S_{21})^2}}{1 - x_c} \tag{3.20}$$

We have now derived convenient responses for the microwave resonator, but we have to derive the responsivity to see how response in phase and amplitude relates to the pair-breaking in the superconductor.

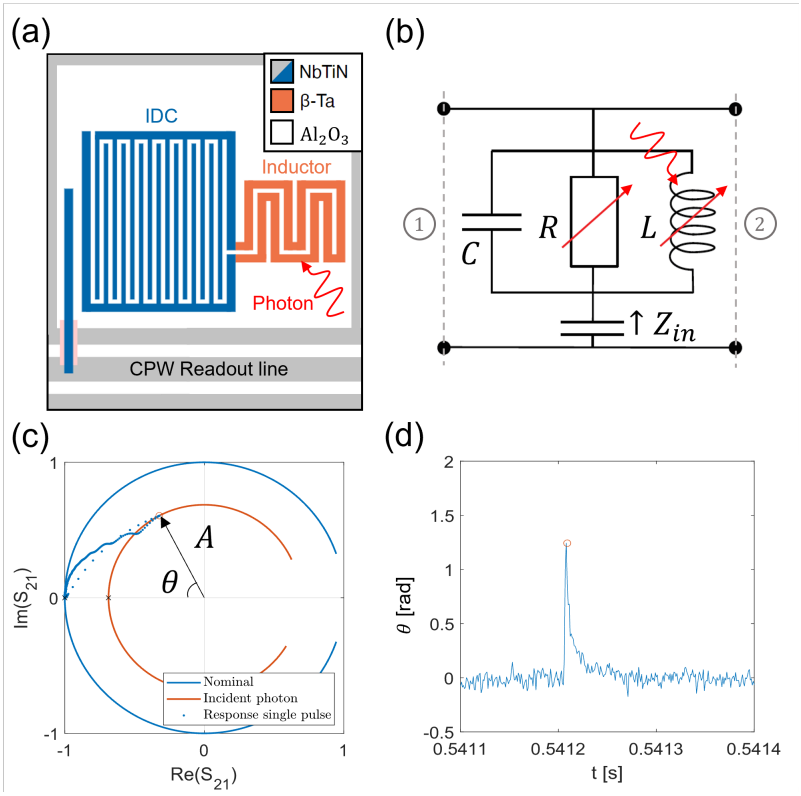

Figure 3.1: Overview of the LEKID readout principle. (a) The hybrid LEKID design with an interdigitated capcitor (IDC) and high resistivity inductor that functions as the absorber for pair breaking photons. The detector is capacitively coupled to the coplanar waveguide (CPW) readout line. (b) Electric circuit equivalent of the LEKID where the absorbed photons change the inductance and resistance of the RLC resonator. (c) Resonance circle in the complex plane as given by the S_{21} transmission. An absorbed photon increases the phase (θ) and decreases the amplitude (A). (d) Phase response of an absorbed photon plotted against time resulting in the characteristic pulse shape.

3.4. Detector Responsivity

We derive the responsivity for a small change in amplitude, $\delta A = 1 - A$, near the equilibrium resonant frequency ω_0 where $\mathrm{Im}(S_{21}) \ll \mathrm{Re}(S_{21})$ and $\tan(\theta) \approx \theta$ and obtain by substituting Equation 3.16 and Equation 3.17 in Equation 3.19 and Equation 3.20

$$\delta A \approx \frac{\delta \mathrm{Re}(S_{21})}{1 - x_c} = \frac{2Q}{Q_i}\frac{\delta Q_i}{Q_i} \tag{3.21}$$

$$\theta \approx 4Q\frac{\delta \omega_0}{\omega_0} \tag{3.22}$$

Substituting Equation 3.14 and Equation 3.13 into Equation 3.22 and Equation 3.21 gives

$$\delta A = \alpha_k \beta Q \frac{\delta \sigma_1}{\sigma_2} \tag{3.23}$$

$$\theta = -\alpha_k \beta Q \frac{\delta \sigma_2}{\sigma_2} \tag{3.24}$$

and, finally, using Using Equation 3.1 we find the responsivity as a function of the change in quasiparticle density [38]

$$\frac{dA}{dN_{qp}} = -\frac{\alpha_k \beta Q}{|\sigma| V}\frac{d\sigma_1}{dn_{qp}} \tag{3.25}$$

$$\frac{d\theta}{dN_{qp}} = -\frac{\alpha_k \beta Q}{|\sigma| V}\frac{d\sigma_2}{dn_{qp}} \tag{3.26}$$

where $|\sigma| \approx \sigma_2$ for $T \ll T_c$ and Q is assumed constant. The latter is usually assured by making the resonated coupling limited ($Q_c \gg Q_i$, such that $Q \approx Q_c$). In this thesis we mainly make use of phase responsivity because this response saturates less quickly.

The responsivity is key in our efforts to design a well performing MKID in the mid-infrared, but, equally so is the noise. In chapter 8 an optimisation method is described to find the MKID design with the optimal signal-to-noise ratio. However, the detector is not always limited by the signal-to-noise ratio, but could also be limited by the loss of hot phonons. These two factors make up the so called resolving power of the detector. This is explained in more detail in the next section.

3.5. Resolving Power and limitations

The responsivity of MKID relates detector response to a change in quasiparticle density. For a single photon response the quasiparticle density can then be related to the energy of the absorbed photon through Equation 3.1. How well an MKID is able to detect the correct photon energy, E_{ph}, is given by the resolving power, R. R can be measured by making a histogram of all the photon energies detected from an statistically relevant number of single photon responses using

$$R = \frac{\langle E_{ph} \rangle}{\delta E_{ph}} \tag{3.27}$$

with $\langle E_{ph} \rangle$ as the average detected photon energy and δE_{ph} as the full width half maximum (FWHM) of the detected photon energy distribution. The resolving power is made up of two parts; the intrinsic resolving power, R_i, and the signal-to-noise resolving power, R_{SN} and relates to those as following

$$\frac{1}{R^2} = \frac{1}{R_i^2} + \frac{1}{R_{SN}^2} \tag{3.28}$$

A detector can thus have a poor resolving power, even though is has great signal-to-noise ratio, if it is limited by the intrinsic resolving power. R_{SN} is determined by the responsivity and noise sources including the Generation Recombination (GR), Two-Level Systems (TLS) and amplifier noise. R_i describes all noise sources that are not contained in R_{SN}. Often, R_i is dominated by hot phonon loss. In 3.2b the different power spectral density contributions of these noise sources is seen. The noise sources are further explained in their appropriate paragraph in the remainder of this section.

GR noise

GR noise is caused by the random process of pair-breaking by thermal photons due the finite temperature in the superconductor. These generated quasiparticles on average recombine after the recombination time τ_{qp}, see Equation 3.2. In equilibrium the generation and recombination processes are in balance, such that the time average quasiparticle number stays constant. In real time, however, there is this constant fluctuation in the quasiparticle number causing noise in the response of the detector, i.e. the GR noise. GR noise can be thought of as a fundamental noise floor for MKIDs, which is often smaller than the other noise sources, but it can be relevant at high temperatures.

TLS noise

TLS noise is caused by atoms tunnelling between two energetically similar sites in a deposited layer of an amorphous solid. These sites are often modelled as two minima in a double-well potential with a difference in minimal energy ε, see Figure 3.2a. At sufficiently low temperatures the atomic tunneling between these sites is driven by an applied electric field. The random arrangement of these tunneling states in the solid causes a time-dependent variation in the dielectric constant of the solid. This introduces frequency noise that is most dominant in the phase response of the resonator. For $T \ll T_c$ TLS noise is seen to decrease with increasing temperature, $\propto T^{-2}$ and is inversely proportional the square root of the internal power in the resonator, $\propto P_{int}^{-1/2}$ [36]. TLS is weighted by the electric field and thus has a larger contribution at the capacitive end of the resonator and to decrease when using larger structures. Methods to decrease the TLS noise in a resonator are then to increase the structure size of the capacitor and choosing a material that does not oxidize well.

Amplifier noise

There are also noise contributions at the system level originating from all instruments in the readout chain, such as attenuators and amplifiers. These noises are generated internally in the instrument and are usually caused by random motions of electrons. The system noise generally has a flat, white spectrum and can therefore be modeled as an equivalent thermal noise source, and characterized with an equivalent noise temperature, T_N. The dominating noise sources is most often the first amplifier right after the detector as it has the largest gain. This is also the case for the measurement setup used in this thesis where the system dominated noise sources originates from a low noise high-electron-mobility transistor (HEMT) amplifier with a noise temperature of 1.5-2 K which is mounted on the 3 K stage [39]. The system noise level in A or θ is related to the (single sideband) T_N as [35]

$$S_{A,\theta} = \frac{k_B T_N}{r^2 P_{read}} \tag{3.29}$$

with P_{read} the microwave readout power and $r = Q/2Q_c = (1 - S_{21,min})/2 \leq 0.5$ the radius of the resonance circle.

Hot phonon loss

There is a fundamental limit to the resolving power of the detector caused by the statistical variation in the number of quasiparticles generated by photons with the exact same energy. It is impossible that 100% of the energy from an absorbed photon can be converted into the breaking of Cooper pairs. After the breaking of the initial Cooper pair the excess energy is converted into momentum of the generated electrons and/or phonons which can cause the breaking of more Cooper pairs. The energy of the photon thus down-converts through these electron-electron and electron-phonon interactions until their energy is insufficient to brake any more Cooper pairs. This down-conversion process is statistical and is captured in the pair-breaking efficiency η_{pb}. η_{pb} is limited to about 0.59 for photons with energy $\gg 2\Delta$. This means that on average an effective energy of 1.7Δ is required to generate a single quasiparticle, instead of the theoretical 1Δ [40]. The resolving power is limited by the variation in this down-conversion process. In the limit, called the Fano limit, the resolving power R_{Fano} is given as [41]:

$$R_{Fano} = \frac{1}{2\sqrt{2\ln(2)}} \sqrt{\frac{\eta_{pb} E_{ph}}{\Delta F}} \tag{3.30}$$

with F (≈ 0.2) the Fano factor, which does not vary significantly across different superconductors [40]. R_{Fano} is thus the maximally attainable resolving power for a superconducting detector.

The Fano limit only holds in the perfect scenario that all energy is contained within the superconductor. If, however, phonons, and especially energetic (hot) phonons escape the superconductor during the down-conversion process the statistical limit is reduced. The effect of excess loss on the resolving power is usually accounted for by introducing a phonon loss factor, J, in Equation 3.30 giving [42]

$$R_i = \frac{1}{2\sqrt{2\ln(2)}}\sqrt{\frac{\eta_{pb}E_{ph}}{\Delta(F+J)}} \tag{3.31}$$

J is dependent on material parameters and detector geometry; it can be reduced by suspending the detector on a thin membrane or by introducing a phonon blocking layer[43]. A factor 8 reduction in J has been shown in NbTiN-Al hybrid coplanar waveguide resonators suspended on a thin SiN membrane. With these devices the highest MKID resolving power has been measured to date R=52 (R_{Fano}=92)[17]
.

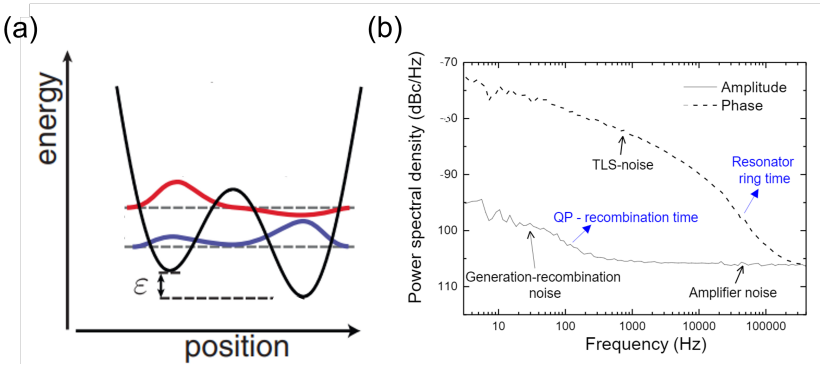

Figure 3.2: (a) Visualisation of TLS tunneling states in an amorphous material. An atom can sit in one of two potential wells. The well differ in minimal energy ε. [44]. (b) Power spectral densities of the phase and amplitude response of an aluminium coplanar waveguide resonator showing the spectral behaviour of the GR, TLS and amplifier noise.[39]

4

Experimental Setup and Modelling

The LIFE initiative requires detectors to operate from 4-18.5 μm, see section 2.1. In this thesis we conduct experiments to measure the performance of MKIDs in this bandwidth at the wavelengths 3.8 μm and 8.5 μm. We also do an additional measurement at 1545 nm. Two different types of detectors are measured: the near-IR LEKID and far-IR MKID, see section 1.3 and Figure 1.3. Results of the first are presented in chapter 6 and of the latter in chapter 7. In this chapter we first explain the general experimental setup and how it varies for the different wavelengths. Then, a theoretical model is introduced that aids in designing and characterising the measurement setup.

4.1. Experimental Setup

All the experiments conducted for this thesis make use of the same cryostat and microwave read-out. These parts are explained first. Then, we explain the variations made on this general setup that accommodate the experiments at different wavelengths.

Cryostat setup

An cross section of the Bluefors® cryostat is seen in Figure 4.1a. It consist of four vacuum pumped temperature stages separated by aluminium shields which are denoted as the '300 K', '40 K', '4 K' and '100 mK' stage. The names of these stages do not indicate their exact temperature, as these very between experiments. The 300K stage is short for the 'room temperature stage'. The detector is contained within an additional light-tight box at the 100 mK stage, called the sample stage. A pulse tube refrigerator cools the stages down to 4 K and a He_3-He_4 dilution refrigerator lowers the temperature to several tens of mK. The detector is very sensitive to the presence of external magnetic fields, like the earth magnetic field, and is therefore protected by a Cryophy and Niobium shield encapsulating the 100 mK stage. It it possible to mount transparent windows in the aluminium shields such that the detector can be exposed to radiation from a source outside of the cryostat.

Microwave readout

The response of the detector is read-out using a homodyne detection scheme, see Figure 4.1b. A microwave signal is generated outside of the cryostat and is split into two; one going directly to IQ mixer and the other is fed into the cryostat. In the cryostat it is attenuated at every temperature stage before entering the sample stage where it is modulated by the microwave resonator. The signal is amplified at the 3 K and 300 K stage with a Low Noise Factory cryogenic LNA and a Miteq, respectively, before it is mixed with the copy of the original microwave signal in the IQ mixer. The IQ mixer delivers the in-phase (I) and quadrature (Q) components of the modulated signal which are converted to the detector phase and amplitude response as described in chapter 5. The sampling rate is 1 MHz.

The general workflow for a measurement is as following. An initial S_{21} scan is made using the vector network analyzer (VNA) to locate all the MKIDs in the frequency domain. The readout powers are then manually optimised per MKID by choosing the maximal power before bifurcation starts to appear in its resonance dip. Now the initialisation is done and the VNA is replaced by the signal generator and I/Q mixer for the measurement. A S_{21} scan is made at the start of every measurement to determine the

resonance frequency and resonance circle in the complex plane which will function as the reference for the response following on this. The S_{21} scan is measured anew for every MKID or readout power. Usually, every MKID is measured at three different readout powers: one being the initially chosen readout power and the other two being 2 dBm above or below it. The data gathered per MKID, per readout power is the I/Q response over time, usually for a duration of 40s and longer if necessary.

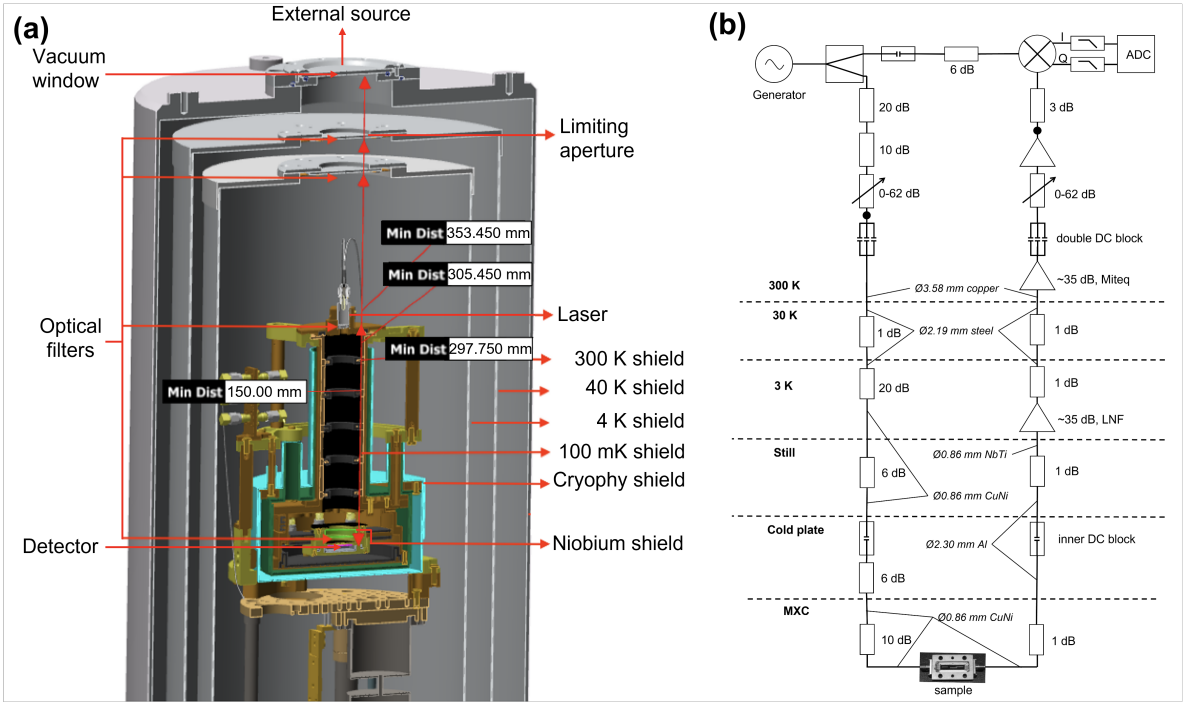

Figure 4.1: An overview of the general experimental setup that is used for the experiments in this thesis. (a) A cross section of the cryostat. The different temperature shields are indicate, as well as the Cryphy and Niobium shields. The laser can be mounted at the 100 mK stage. The cryostat can also be opened up to an external source. For this purpose optical filters are installed at the indicated positions. The limiting aperture for the detector looking at the the 300 K stage is located at the 40 K stage and is equal to 1 inch. (b) The microwave components in the readout system. The signal from the generator is first split feeding one signal direct to the IQ mixer and the other is fed into the cryostat using flexible SMA cables. Within the cryostat the signal is attenuated at every temperature stage and interrupted with double and single DC blocks. After the sample box the signal is amplified at the 3 K and 300 K stages before it is mixed with a copy of the original signal in an IQ mixer. Alternatively the signal generator and IQ mixer can be replaced by a vector network analyser (VNA) for quick characterisation. The VNA replaces the complete system above the thick black dots.

Variations on the experimental setup

Two different experimental setups have been used for the experiments of this thesis: a closed setup for laser measurements at 1545 nm and a open setup for measurements at 3.8 and 8.5 μm. A third setup has been designed for future experiments at 18.5 μm: the black-body setup. A schematic overview of these difference setups is found in Figure 4.2.

Closed setup The closed setup is used for measurement witht the 1545 nm laser. An external source generates a laser that is fed into the cryostat through an optical fiber and collimated at the 100 mk stage where it illuminates the sample stage. The laser power can be attenuated to obtain the desired radiation power. This setup is 'closed' as all higher temperature shield are closed with aluminium lids. This does not mean all stray light is rejected.

Open setup At 3.8 and 8.5 μm the detector is exposed to a source external to the cryostat. Using an external source will expose the detector to the thermal background originating from the 300 K, 40 K and 4 K stages. The thermal background of the 300 K stage will dominate as the radiated power scales with temperature to the fourth. The peak spectral radiance of the 300 K background is at about 10 μm. Optical filters are used to attenuate the radiation at undesired wavelengths as much as possible, while ensuring sufficient power at the desired wavelength. The optical

filters can be installed at all temperature stages and sample stage. At 3.8 μm a monochromator is used as the source to increase the power at the desired wavelength. A monochromator, in essence, is a lamp emitting a black-body like spectrum combined with a set of slits and gratings that allow for the selection of a specific wavelength from the spectrum with a defined bandwidth. The monochromator that is used in this thesis is the Cornerstone^{TM} 260 (model: CS260-USB-4-MC-A) manufactured by Oriel®. The grating (model nr. 74080) has 150 lines/mm and reciprocal dispersion of 25.8 nm/mm at a blaze wavelength of 4000 nm. It covers the bandwidth 2.5-12 μm with >20% efficiency (peak efficiency is 70%). The source is a 100 W, Quartz Tungsten Halogen (QTH) lamp with its peak spectral radiance at 800 nm. The monochromator light is collimated and manually aligned at the centre of the opening of the 300 K shield such that is shines up in to the cryostat onto the detector. The power can be manually adjusted using an variable aperture right before the vacuum window. The spectral radiance of the QTH lamp at 8.5 μm is about a factor 1000 less than at 3.8 μm. Therefore, it is not expected to add significant power on top of the thermal background at 8.5 μm. The thermal background will act as our source of radiation as the 8.5 μm. Attenuating the undesired radiation at 8.5 μm will be more convenient as it is closer to the peak spectral radiance of the 300 K background.

Black-body setup No experiments have been done at 18.5 μm, but a setup has already been designed and manufactured. The setup consists of a cryogenic black-body mounted under the 4 K stage. Its temperature can be externally adjusted which allows us to manipulate the emitted spectrum for the benefit of our measurement. Two holders have been designed that tilt the optical filters to 45°. This prevents standing waves between the filters by reflecting the radiation to an absorbing layer applied on the inside of the tilted holders.

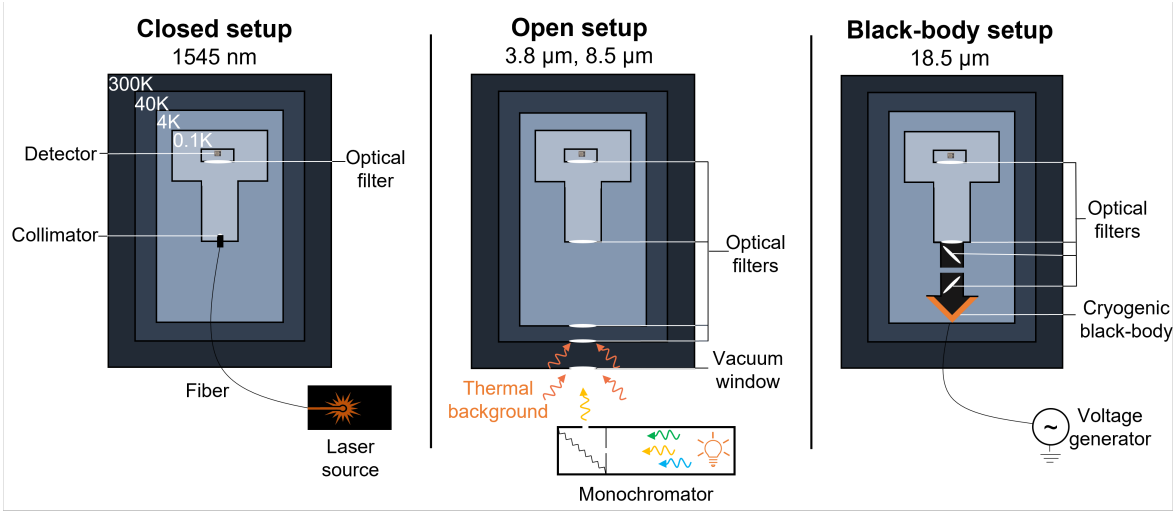

Figure 4.2: Schematic overview of the different experimental setups that are used for measurements at different wavelengths. (left) The open setup used for the laser measurements at 1545 nm. An external source generates a laser that is fed into the cryostat through an optical fiber and collimated at the 100 mk stage where it illuminates the sample stage. The laser power can be attenuated to obtain the desired radiation power. (middle) The open setup that is used at 3.8 μm and 8.5 μm. At 3.8 μm the main source of radiation is a 100 W, quartz tungsten halogen (QTH) lamp. The monochromator selects a specific wavelength with a defined bandwidth from this spectrum using a grating and slits. Optical filters are present at every temperature stage to attenuate the undesired radiation from the thermal background. At 8.5 μm the monochromator is not expected to deliver sufficient power and the thermal background will act as the main source of radiation. (right) The black-body setup used for the experiment at 18.5 μm. A cryogenic black-body is installed at the 4 K stage that can be heated from the outside by running a current through a resistor attached to the black-body. Two filter holders are designed that can be mounted to the black-body and the 100 mK stage. The holders tilt the filters with 45° such that the reflected radiation is absorbed by the absorbing layer applied on the inside of the holders.

4.2. Modelling of the Experimental Setup

In this section we model the open setup that is described Figure 4.2. The model is important as it helps to characterise the contribution of the thermal background radiation in our experiments. The model also helps in optimising the optical filtering configuration. The optical filters should attenuate the undesired radiation as much as possible, while ensuring the right amount of power at the desired wavelength. The model can also give insight into the optical efficiency of the detector. However, this is not meant to be an exact determination, but more an order of magnitude estimate. In this section we describe the model, starting with how we calculate the radiated power on the detector pixel. Then, we explain how the absorbed power is calculated. Next, we explain the different optical filters that are used in the experiments. We concluded by determining the that is used to find the optimal filter configuration for the different experiments. We will start at the source, after which we will characterise the optical filters, then we explain how we model our detector and conclude with how we calculate the power absorbed by the detector.

Radiated and absorbed powers

Every temperature stage emits thermal radiation. We calculate the pair-breaking, radiated power incident on the detector per temperature stage as

$$P_{rad}^{T} = A\Omega \int_{0}^{hc/2\Delta} \Theta(\lambda) B_{\lambda}(\lambda, T) d\lambda \tag{4.1}$$

with

- A the surface of the detector pixel. It is equal to the surface of the detector lens, see Figure 4.5.
- $\Omega = 2\pi \times \left[1 - \cos\left(\tan^{-1}\left(\frac{r}{d}\right)\right)\right]$ is the the opening angle of the detector pixel with r the radius of the limiting aperture as seen by the detector and d the distance from the detector to the limiting aperture. In our experiments we have a limiting aperture with r=12.70 mm at the 40 K stage such that d=353.45 mm, see Figure 4.1.
- $\Theta = \prod_i \vartheta_i$ the product of all the transmission spectra ϑ_i of all the optical filters i that are in between the temperature stage and detector.
- B_{λ} is the spectral radiance emitted by the temperature stage with temperature T. We model the temperature stage as a black body such that its spectral radiance is described by Planck's law:

$$B_{\lambda}(\lambda, T) = \frac{2hc^2}{\lambda^5} \frac{1}{e^{hc/\lambda k_B T} - 1} \tag{4.2}$$

  We realise that the actual spectrum can differ greatly, especially for reflective materials such as Al. Therefore, we estimate a relative uncertainty in B_{λ} of 20% and assume a triangular distribution. The Stefan-Boltzmann law is used to validate the algorithm: $B(T) = \int_0^{\infty} B_{\lambda}(\lambda, T) d\lambda = \sigma T^4$ with σ the Stefan-Boltzmann constant. The exact temperatures used in the model for the different stages are: 292 K, 37.8 K, 2.85 K and 0.1 K. The total radiated power P_{rad} is obtained by summing over P_{rad}^{T} for every stage. As $B(T) \propto T^4$, the radiation emitted by the 300 K stage will dominate the radiation from lower temperature stages. However, this radiation is also subjected to the most optical filtering so we cannot neglect the radiation from the lower temperature stages.

The total absorbed power P_{abs} is calculated from the total $P_{rad} = \sum_T P_{rad}^{T}$ from all temperature stages as

$$P_{abs} = \eta_{opt} P_{rad} \tag{4.3}$$

similar to Equation 3.1. P_{abs} can also be retrieved from measurement as $P_{abs} = E_{ph} N_{ph}$ with N_{ph} the detected photon count rate. We find the standard deviation σ in the radiated and absorbed powers by propagating the uncertainty of their individual variables. For the absorbed power this gives

$$\sigma_{abs} \approx P_{abs} \sqrt{\left(\frac{\sigma_{opt}}{\eta_{opt}}\right)^2 + \left(\frac{\sigma_A}{A}\right)^2 + \left(\frac{\sigma_\Omega}{\Omega}\right)^2 + \left(\frac{\sigma_I}{I}\right)^2} \tag{4.4}$$

with σ_I the standard deviation in the integral part $I = \int_{\lambda} \Theta(\lambda) B_{\lambda}(\lambda, T) d\lambda$.

In-, near- and out-of-band powers

It is necessary to make more specific distinctions in the pair-breaking radiation in Equation 3.5 as not all radiation has the same effect on the detector. We define three distinct wavelength bands: the in-band, the near-band and the out-of-band, see Figure 4.3. We explain these below and also apply them to the near-IR LEKID.

In-band The in-band is defined as the full width of the bandpass filters that are used in the experiment. This bandwidth will ultimately limit the resolving power in case of a perfect detector. The minimum in-band power should provide a statistically relevant set of pulses within the time of measurement. In our experiments we adjust the measurement time to obtain at least a 1000 pulses per detector. The maximum in-band power is set at $E_{ph}/2\tau_{qp}$ which ensures that pulses do not overlap too often. For the near-IR LEKID with τ 50 μm this gives 0.52 and 0.23 aW at 3.8 and 8.5 μm respectively.

Near-band The near-band is defined as the wavelength range which can still result in detectable single photon pulses and thus depends on the resolving power of the detector. This near-band radiation limits the resolving power by introducing an additional variation in the detected pulse heights and by adding photon noise. For a valid measure of the resolving power we need the near-band power to be much lower than the in-band power, i.e. P^{in}/P^{near}> 1000. We estimate the near-band for the near-IR LEKID using the signal-to-noise resolving power obtained for the detector at 1545 nm: R_{SN} 10. If we assume linearity in response, the noise to be constant and require a pulse response to have at least R_{SN}=2, we expect to see single photon pulses up to a 8 μm. Consequently, we define the near-band from 0-8 μm.

Out-band The out-of-band is defined as all wavelengths longer than the near-band and up to $hc/2\Delta$. The out-of-band radiation limits the resolving power of the detector as it increases the quasiparticle density, which lowers τ_{qp}, thereby lowers the response. Furthermore, it contributes additional photon noise. We require the out-of-band power to add only a slight fraction of the number of quasiparticles created by a single, in-band photon. Say we take a factor 1000 difference, we then obtain $E_{ph}/\tau_{qp}P^{out}$> 1000 from Equation 3.1. The factor 1000 is just an illustrative example that allows us to relatively compare out-of-band powers. We stay away from interpreting the values in an absolute manner. For the near-IR LEKID we define the out-of-band is everything from 8 μm up to 4.1 mm. If we use the value of τ_{qp}=53 μs found at 1545 nm, we obtain P^{out}<9.9×10^{-19} W at 3.8 μm.

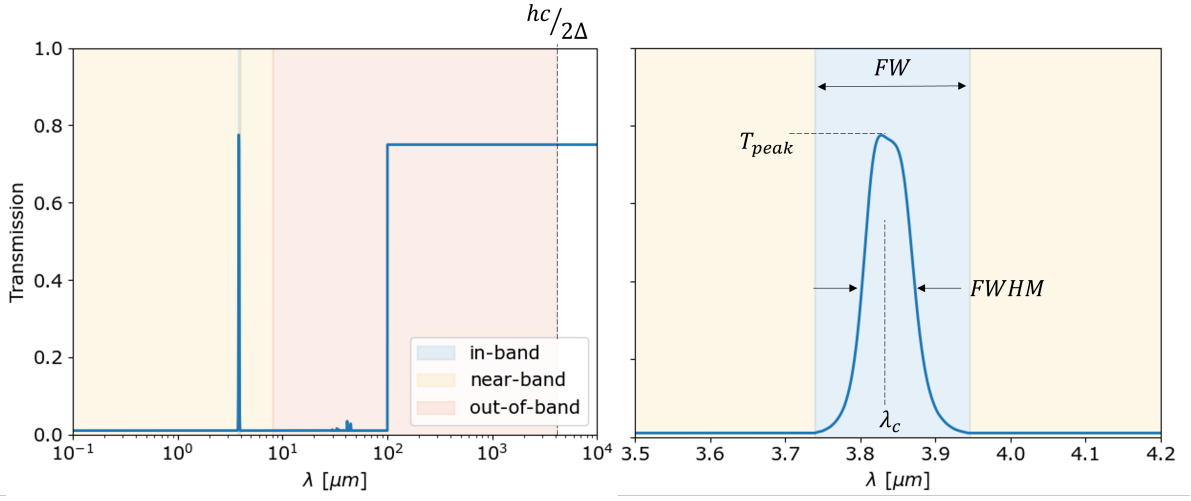

Figure 4.3: Visualisation of the in-, near- and out-of-band regions. The in-band is equal to the full width of the bandpass filter which is the 3.8 μm bandpass filter in this example. The near-band is everything below $\lambda = 8\,\mu$m as longer wavelengths will not result is distinct single photon pulses. The out-of-band is everything shorter than the pair-breaking wavelength $hc/2\Delta$ (4.1 mm for β-Ta, 2.6 mm for Al)

Optical Filtering

The optical filters are characterised by their manufacturer for only a limited spectral range. This suffices to compute the in- and near-band powers, but it does not suffice to compute the out-of-band power. We look to the literature to make an estimation of the transmission at wavelengths much longer than the characterised spectral range. For the bandpass filters we pose a relative uncertainty of 5%, for the neutral density filters 20% and for all other filters 10%. The bandpass filters have lowest uncertainty as they have been specifically characterised for us by their manufacturer. The remaining uncertainty is because they have been characterised at 77 K while we use them at temperatures below 4 K. The neutral density filters have the largest uncertainty. They are reflective filters with a metal substrate so their transmission is expected to be even more dependent on temperature. In all transmission uncertainties we assume a triangular distribution. The filters used in this thesis are seen in Figure 4.4 and are described below:

- The 1mm thick, 3.8μm band pass filter (BP3.8) has a peak transmission of 0.78 at the central wavelength λ=3.828μm and a full width of 209nm. The filter is manufactured by Northumbria Optical Coatings Ltd (NOC) and is characterised at 77K from 0.8-45μm. The filter has an 1 mm thick infrared fused-silica (IR-FS) substrate and based on literature [45] we estimate a transmission of 0.75 for λ>100 μm.
- The 1mm thick, 8.5 μm band pass filter (BP8.5) has a peak transmission of 0.73 at the central wavelength λ=8.473 μm and a full width of 436 nm. The filter is manufactured by Northumbria Optical Coatings Ltd (NOC) and is characterised at 77 K between 0.8-45 μm. The filter has an 1mm thick Germanium substrate and we estimate a transmission of 0.3 for λ>45 μm [46]. In our experiments a BP8.5 filters will always be combined with a CaF_2 filter to attenuate the considerable transmission that is seen between 20-40 μm.
- The 1mm thick, Germanium filter (Ger) is manufactured by Thorlabs and is characterised up to 25 μm and, similar to the BP8.5, we estimate the transmission for the longer wavelengths to be 0.3[46].
- The 1mm thick, CaF_2 filter (CaF2) is manufactured by Eksma Optics and is characterised up to 25μm and, similar to the BP3.8, we estimate its transmission λ>200μm to be equal to 0.5 [47].
- Neutral density filters attenuate the radiation approximately uniformly across the spectrum. They are characterised by their optical density, $OD = \log_{10}(1/T)$ with T the average transmission. We use neutral density filters with OD=2 (ND2) and OD=3 (ND3), meaning that they will attenuate the incident optical power by a factor 10^2 and 10^3, respectively. These filters are manufactured by Thorlabs Inc. and have been characterised for 0.2-18 μm. We do not expect the transmission to increase at longer wavelengths as the neutral density filters have a metal coating. We extend the value found at the end of the characterised region, at 18μm, to all longer wavelengths for both ND2 and ND3.

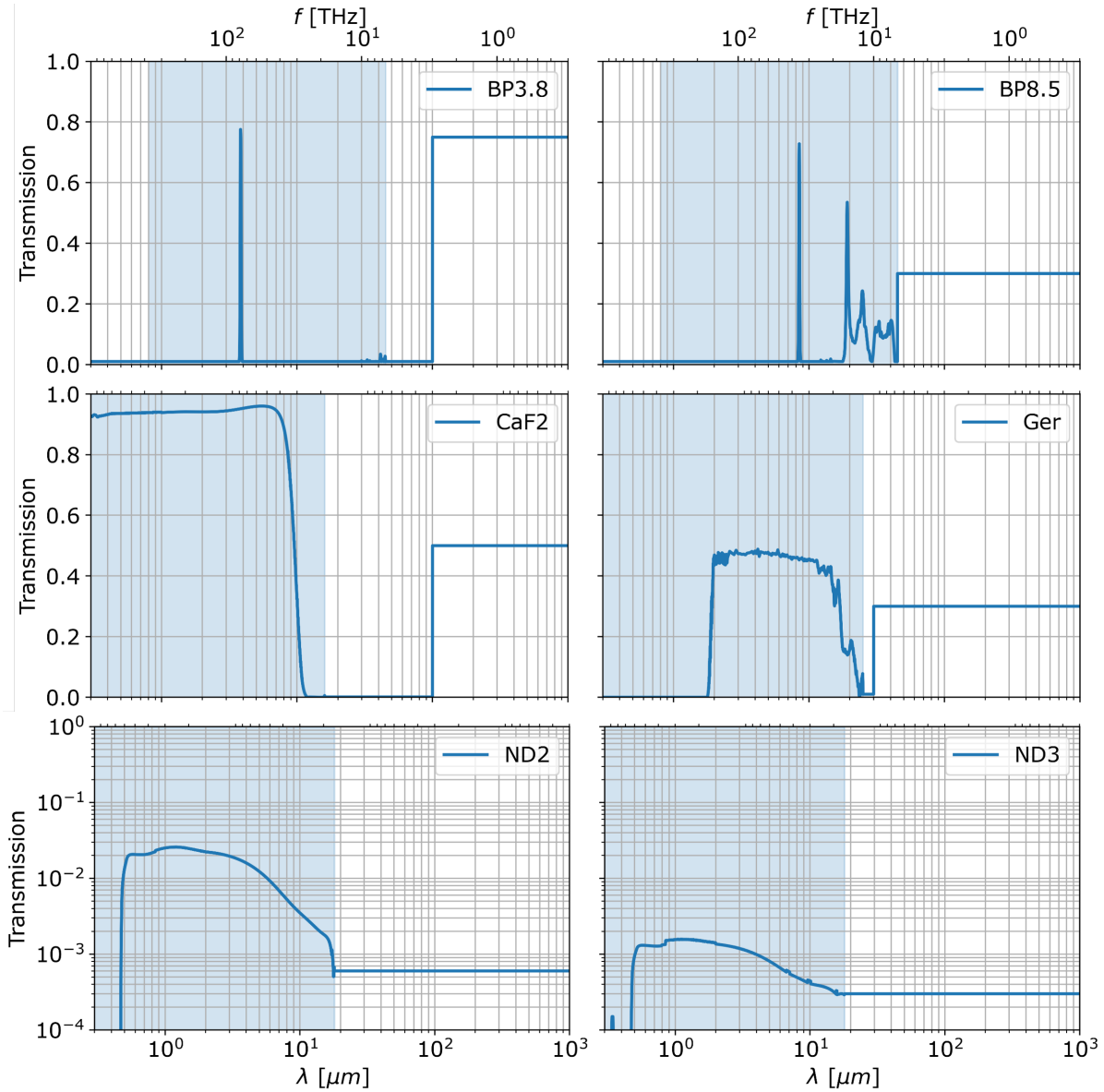

Figure 4.4: Overview of the transmission spectra of the various filters that are used in the experiments and for the modeling of the experimental setup. The blue regions denote the wavelength ranges where the filters have been characterised. Outside of the blue range we have to estimate the transmission based on literature. The top row show the 3.8μm (BP3.8) and 8.5μm (BP8.5) bandpass filters. The middle row shows the CaF_2 (CaF2) and Germanium (Ger) filters whereas the bottom row shows the neutral density filters of order 2 (ND2) and of order 3 (ND3).

Detector model

In this section we estimate η_{opt} and its uncertainty such that we can model P_{abs}. This is supposed to be more of an order of magnitude estimation rather than a definite determination of the true efficiency. The true value of the optical efficiency should be obtained from dedicated measurements. For now we only model the near-IR LEKID. The far-IR MKID was designed for a different wavelengths, so we do not really know anything about the optical coupling in the mid-IR.

η_{opt} is built up of all elements that influence the fraction of P_{abs} in the inductor to P_{rad} at surface of the lens, see Figure 4.5a. Below describe all the elements that are included in the model.

manufacturing tolerances in the microlens array The array (APO-Q-P150-R0.39) is manufactured by Advanced Micro-optics Systems (AMS) and has positive orthogonal lenses with pixel pitch D=150$\pm$1 μm, focal length F=0.85mm$\pm$5% and spectral transmission ϑ_{fs}. The uncertainties in D and F are provided by the manufacturer and assumed to be $\pm 2\sigma$.

transmission of fused silica The microlens array is made of of 1.25mm thick, fused silica. Fused silica is only characterised up to 5μm, however, similar to the BP3.8 filter, we estimate a transmission of 0.75 for λ>100μm, see Figure 4.5b. We estimate a relative uncertainty of 10% in its transmission and assume a triangular distribution.

the inductor surface We model the inductor as a square surface with sides 24 μm (=$\sqrt{2}R$). The uncertainty in R is 2 μm which is introduced because the inductor is not a perfect square. We assume a rectangular distribution for the uncertainty.

diffraction In the diffraction limited case the airy pattern describes the intensity of the light on the focal plane as a function of radius r, D, F and λ. We can obtain the relative enclosed power within the inductor, η_{encl}, as a function of λ, seeFigure 4.5d. The uncertainties in D, F, R are numerically propagated to find the uncertainty in η_{encl}.

lens misalignment We estimate an uncertainty lens alignment dx, dy=5 μm and assume a triangular distribution. These uncertainty are also numerically propagated in η_{encl}.

fill fraction β-Ta does not cover the full inductor area but only about 75% due to the 2 μm separation of the inductor lines. We correct for this by adding a fill fraction η_{fill} in the model. However, η_{fill} is wavelength dependent, but its exact dependency is not modeled here. η_{fill} must between 0.75 and 1, so we estimate η_{fill}=0.88$\pm$0.10.

absorption efficiency The absorption efficiency η_{abs} of β-Ta is approximated to be wavelength independent with a value of 0.25$\pm$0.02. The uncertainty is introduced by extrapolating the value from [48].

Finally, we find

$$\eta_{opt} = \eta_{fill}\eta_{abs}\eta_{encl}\vartheta_{fs} \tag{4.5}$$

and the standard deviation σ_{opt} by analytically propagating the uncertainties of the individual variables, similar to Equation 4.4. We have not considered the optical aberrations introduced by the lens when not in the diffraction limited case. We also have assumed that all the light incident on the square lens is focused onto the detector, even though this is probably not the case. We also approximated Ω to be constant across A and also equal for all temperature stages. These aspect could be implemented in future work.

η_{opt} and σ_{opt} are wavelength dependent and are plotted in Figure 4.5d. The relative standard deviation in η_{opt} is 13%. At 3.8 μm we find η_{opt}=0.08$\pm$0.02. At 8.5 μm $\eta_{opt} \ll$0.01 due to the low transmission of the lens and diffraction. Furthermore, we find that the contribution to σ_{opt} is largest from the uncertainty in η_{encl} and the other contributions are similar, see Table 4.1. Overall, we find the relative standard uncertainty in P_{abs} to be 21%. We find that σ_{opt} and σ_I have similar contributions to σ_{abs}, both dominating σ_A and σ_I.

Table 4.1: Overview of the contributions to the uncertainty in P_{abs}, see Equation 4.4. The have also split up the different contributions to eta_{opt}, see Equation 4.5.

		Rel. σ [%]	*Rel. contr. to σ_{abs} [%]*
	η_{fill}	*5.8*	*7.7*
	η_{abs}	*4.9*	*5.5*
η_{opt}	ϑ_{fs}	*4.1*	*3.8*
	η_{encl}	*10*	*24*
	Subtotal	13	41
A		<1	≪1
Ω		<1	≪1
I		16	59
Total			100

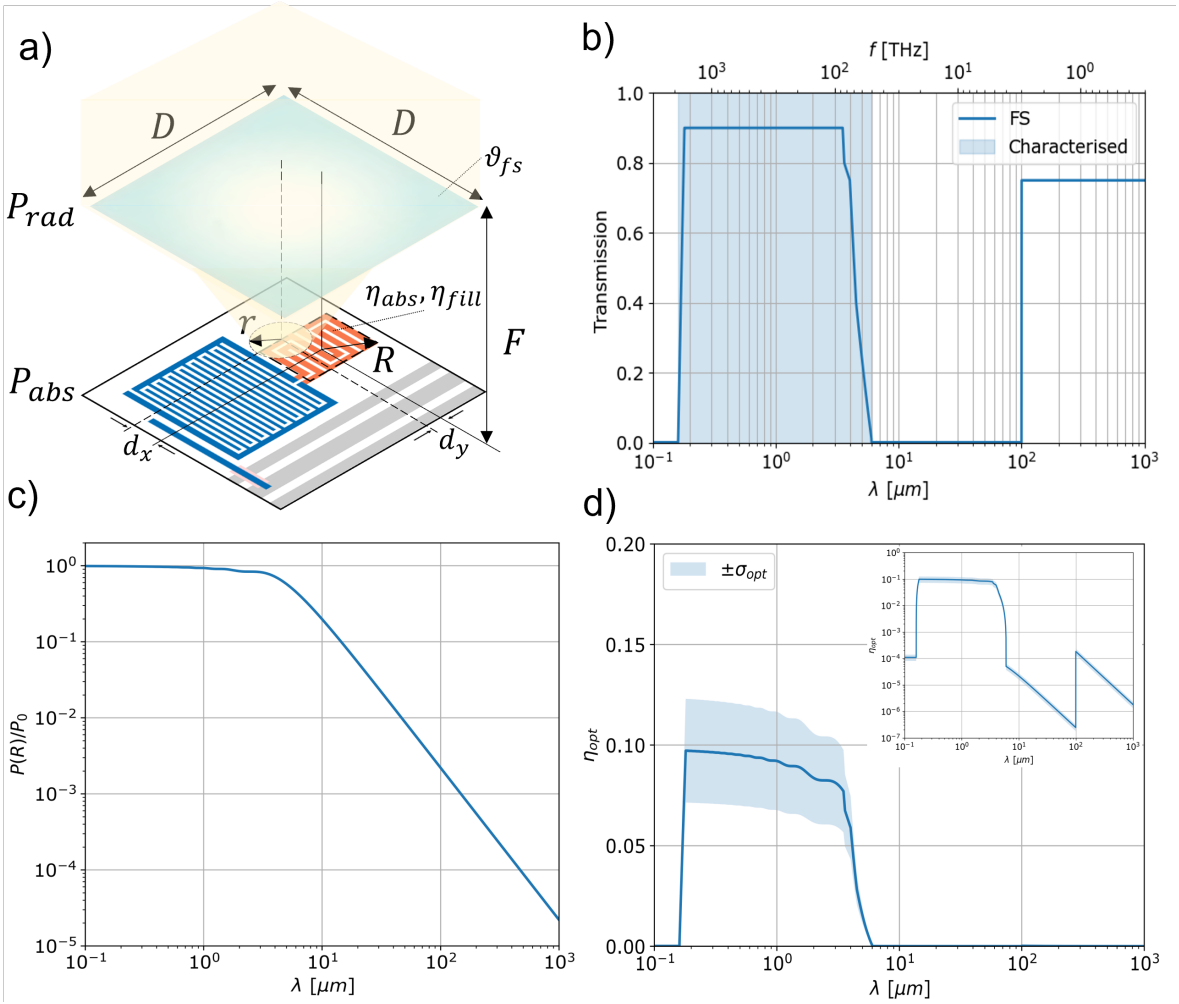

Figure 4.5: (a) Schematic overview of the various elements that influence the optical efficiency η_{opt}=P_{abs}/P_{rad} of the detector. P_{rad} is the power incident on the $D \times D$ lens with transmission ϑ_{fs} and focal length F. P_{abs} is the power absorbed in the β-Ta inductor with size $\sqrt{2}R \times \sqrt{2}R$. The β-Ta has an absorption efficiency η_{opt} and fill fraction η_{fill}. (b) The transmission ϑ_{fs} of the 1.25 mm thick, fused silica lens. (c) The relative enclosed power within radius R, η_{encl} as a function of wavelength λ. η_{encl} is obtained in the diffraction limited case when the intensity of the light on the inductor plane is described by the Airy pattern as a function of radius r, focal length F, aperture D and wavelength λ. We also incorporate uncertainties in the lens alignment: dx and dy. All of these factor combined give (d) the total η_{opt} as a function of λ. The inset shows a the same plot but with the y-axis on a logarithmic scale.

5

MKID Data Analysis

The homodyne readout, see section 4.1, delivers the raw data of the detector response in the I and Q coordinates as a function of time. These coordinates can be converted to a response in phase θ and amplitude A using the following relations:

$$A = \frac{X}{\langle X \rangle} \tag{5.1}$$

$$\theta = \pi - \tan^{-1}\left(\frac{Q}{I}\right) \tag{5.2}$$

with $X = \sqrt{I^2 + Q^2}$. A is normalised to 1. A π phase shift is applied to θ such that is has its axis of orientation in the negative I direction. Incident photons will cause a sudden increase of response, a pulse, and the height of the pulse is a measure for the energy of the photon, see Figure 3.1. An optimal filter is applied to obtain a more accurate estimation of the actual pulse heights by compensating for the frequency dependent noise. First, we explain how this optimal filter is applied and conclude with how we compute the resolving power of the detector. An overview of the data analysis process described in this chapter is visualised in Figure 5.3.

5.1. Optimal Filter

The optimal filter is a signal processing technique that computes a 'frequency weighted' average in the presence of coloured noise, i.e. noise that is frequency dependent. We apply an optimal filter to construct the best possible estimates of the pulse heights H for every pulse $D(f)$. As inputs it requires the normalized pulse model $M(f)$, the noise model $N(f)$, such that $D(f) = HM(f) + N(f)$. H is computed as following [49], [50]

$$H = \frac{\int_{-\infty}^{\infty} \frac{DM^*}{|N|^2} df}{\int_{-\infty}^{\infty} \left|\frac{M}{N}\right|^2 df} \tag{5.3}$$

In the discrete and finite domain $D(f)$ and $N(f)$ are equal to their power spectral density (PSD) estimates. In Figure 5.3b we have plotted the typical PSD estimates for the 1545 nm measurement. The effect of the optimal filter on the 1545 nm data is seen in panel d. The blue histogram gives the distribution of peak heights without optimal filter, whereas the red histogram gives the distribution after the optimal filter has been applied. The average of the distribution is slightly higher and so is the resolving power as the standard deviation has stayed the same.

In the following subsections we will explain how the noise and pulse models are obtained from the data.

Pulse Model

The *findpeaks* function in Matlab is used to detect the peaks of the photon pulses in the data. To obtain the most accurate indication of the detector performance we only want to analyse single-photon pulses:

the pulses that are due to the absorption of a single photon. We use the singe-sided, fast Fourier Transform (FFT) of the pulses to find $D(f)$. Similarly, we find $M(f)$ from the average, normalised pulse in time domain. How we find the photon pulses and filter for single-photon pulses is explained in the following paragraphs.

Selecting photon pulses
The *findpeaks* function accepts additional criteria to improve the selection of the desired peaks. Two criteria are used in this thesis: the *MinPeakHeight* (*MPH*) and *MinPeakProminence* (*MPP*). *MPH* sets a minimum height for the peaks, whereas *MPP* sets a minimum prominence. The prominence of a peak is the minimum vertical distance that the signal must descend on either side of the peak before either climbing back to a level higher than the peak or reaching an endpoint. Basically, it is a measure for the how much the peak 'stands out' compared to surrounding peaks.

Previously, the values of *MPP* and *MPH* would be chosen manually, but a method is presented here that provides a more objective way. This method involves making a 3D surface plot of the number of peaks N_{pks} found in the data while independently varying both the *MPP* and *MPP*. Two examples are shown in Figure 5.1 at 3.8 μm and 1545 nm data. Note the logarithmic scale of the Z-axis. Three general areas can be distinguished in the surface plot. These are related to three types of peaks present in the data: peaks originating from noise, peaks from photons and peaks from high-response outliers.

Peaks from noise These are in the area where N_{pks} is highest and where *MPH* and *MPP* are lowest. The peaks found here are mostly peaks from noise; the number of peaks from noise decreases rapidly for increasing *MPH* and *MPP*.

Peaks from photons The second area is where N_{pks} seems to stay relatively constant for a certain range of values before dropping off again. These peaks result from absorbed photons that are clearly distinguishable from the noise. A clear plateau is visible in the transition from the noise to the photon peaks. Values for *MPP* and *MPH* should be chosen from somewhere on this plateau. This is more challenging at 1545 nm than at 3.8 μm as the plateau is smaller, indicating that the pulses from photon are less distinguishable from noise.

Peaks from outliers The third area is starts at the second plateau where N_{pks} is lowest for the highest values of *MPP* and *MPP*. This area indicates the presence of very high response pulses in the data. These outliers are due to high energetic stray light or cosmic rays. These outliers are rejected by setting a response limit at 3 sigma above the average photon response.

The process of choosing the optimal *MPP* and *MPH* from this plot could be automated in future work. The values chosen for *MPP* and *MPP* are experiment specific and will be provided together with the results from the experiments.

Rising edge alignment
In order to obtain the pulse model for the optimal filter we need to align all the pulses. The pulses are aligned on their rising edge because this is the most accurate indication of the start of the pulse. Aligning on the rising edge means aligning at the point which is closest to half of the pulse maximum. However, the rising edge often comprises of just a few data points which makes it hard to find the point at half the maximum. Therefore, the data is upsampled to accurately find the rising edge. The upsampling is done using the *resample* function in Matlab. Generally, we increase the number of data points with a factor 8.

Removing overlapping pulses
We filter all the peaks that are too close to each other in order to remove overlapping pulses. However, sometimes pulses overlap and only one of the overlapping pulses is detected. These pulses are clearly visible when we plot all filtered and aligned pulses on top of on another. In Figure 5.2a we have highlighted the two examples of misaligned, overlapping pulses in yellow and orange. These pulses are aligned on the rising edge of their secondary pulse. A correctly aligned pulse is highlighted in red. We see that the overlapping pulses give a higher maximum response than the correctly aligned pulse which influences the results. These overlapping pulses are rejected using a filter that requires a manual input of the maximal height a pulse can have before the average rising edge. This process should be automated in future work.

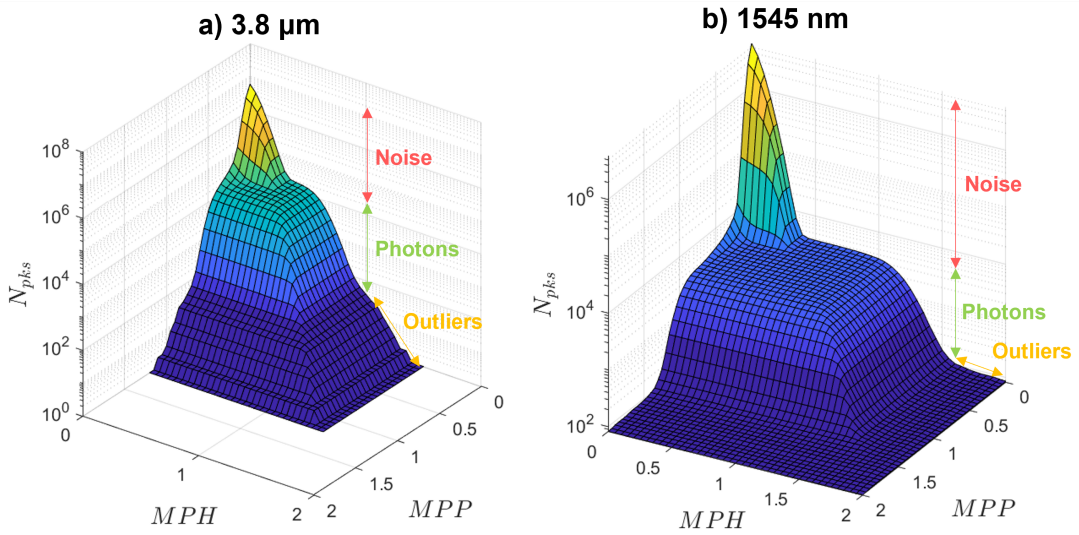

Figure 5.1: 3D surface plots of the number of peaks N_{pks} found with the *findpeaks* function in Matlab as a function of the peak selection attributes *MinPeakHeight* (*MPH*) and *MinPeakProminence* (*MPP*) for (left) 3.8μm data and (right) 1545nm data. Note the logarithmic scale of the y-axis. Three areas can be identified, at 1545 nm better than at 3.8 μm. Peaks from noise, peaks from photons and peaks from outliers. The latter can be high energetic stray light, cosmic rays or a response artifact. A clear plateau is visible in the transition from the noise to the photon peaks. Values for *MPP* and *MPH* should be chosen from somewhere on this plateau. This plateau is much smaller in size for at 3.8μm. This is because the lower energetic photons trigger a lower response. The smaller the plateau, the more challenging it becomes to distinguish photons from noise.

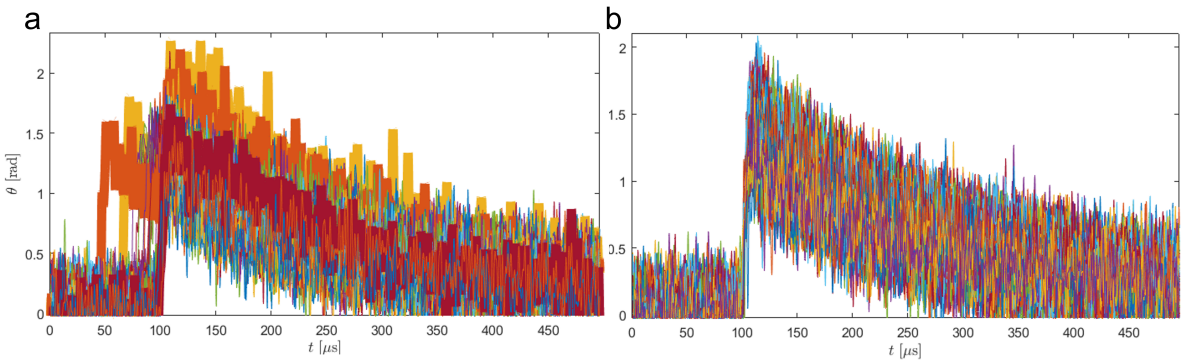

Figure 5.2: Illustration of the removal of overlapping pulses. (a) All pulses from a data set plotted on top of one another with a couple of misaligned pulses. Three pulses (yellow, orange and red)have been highlighted by a thicker line width. The yellow and orange pulses are two examples of overlapping pulses that are incorrectly aligned on the rising edge of their secondary pulse. The red pulse is an example of a correctly aligned pulse. (b) The same plot as in (a) but now with the overlapping pulses removed.

Noise Model

The noise is obtained from a 'dark' measurement, meaning that the radiation source is turned off. This does not mean that there is no background radiation or even pulses present in the data. Stray light and cosmic rays can still causes pulses in the dark data. Noise data is cut from in between the detected pulses. If there are many pulses present in the data the maximal obtainable bandwidth of the noise power spectral density estimate (PSD) decreases. We use the *pwelch* function in Matlab to compute the average PSD of the noise data. The periodogram is not a consistent estimator of the true PSD of a wide-sense stationary process. Therefore, Welch's technique is used which cuts the time series into overlapping segments of equal length, computes a modified periodogram for every segment and averages these to obtain an estimate of the power spectral density with reduced variance [51]. The noise model for the optimal filter, $N(f)$, is obtained from a 1000 noise segments with a segment length equal to the pulse window used for the pulse model.

5.2. Resolving power

The resolving power R can be computed with Equation 3.27 if we know how to convert the heights H to energies E. For this we assume to be in the small response limit, i.e. $\theta < 1.5$ rad, where the relation between H and E is simply linear, meaning

$$\delta E = \frac{|E|}{|H|}\delta H \tag{5.4}$$

This allows us to compute R with $\langle H \rangle$ and δH. The latter is obtained by applying a kernel density estimate to H and determining the FWHM of the estimate. If θ >1.5 rad, a different coordinate system can be used to correct for the non-linearity [18], [52]. However, in this thesis we constrain ourselves to the small response limit. The bin width of the distribution is important for the goodness of the estimate and is optimised using the method proposed by [53].

R_{SN} is computed similar to R but by substituting δH with δH_n: the FWHM of the noise response. δH_n is the fundamental resolution limit that is attainable by H as [49], [54], [55]:

$$\delta H_n = 2\sqrt{2\ln(2)}\left[\int_{-\infty}^{\infty} \frac{|M(f)|^2}{|N(f)|^2} df\right]^{-1/2} \tag{5.5}$$

which is obtained by computing the standard deviation in H that would be measured if no pulse were present, i.e. $D(f) = N(f)$. The factor $2\sqrt{2\ln(2)}$ is due to the conversion from the standard deviation to the FWHM. If we now substitute Equation 5.5 and Equation 5.4 we obtain:

$$R_{SN} = \frac{1}{2\sqrt{2\ln(2)}} \frac{\langle H \rangle}{\sigma_H} \tag{5.6}$$

Finally, the intrinsic resolving power, R_i, can be obtained using Equation 3.27 with R and R_{SN} known.

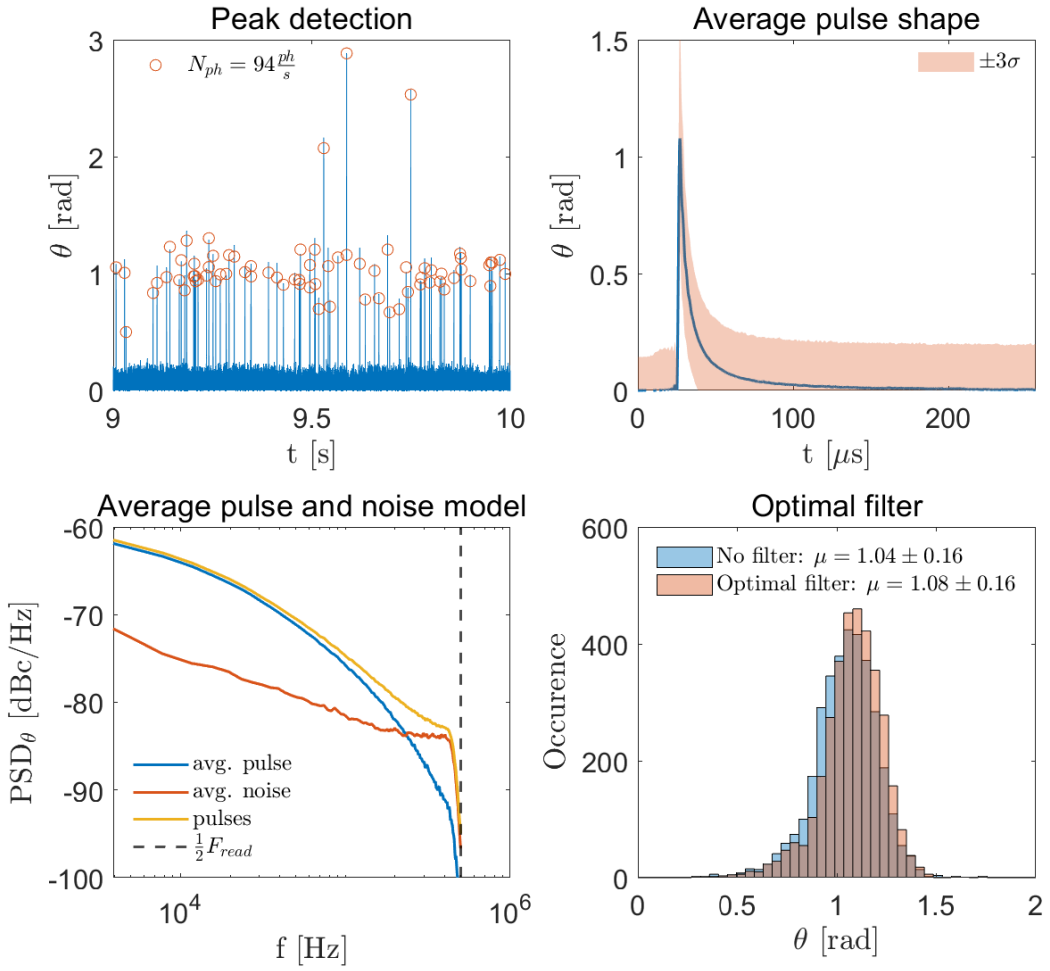

Figure 5.3: Overview of the data analysis process that is used for this thesis. The data is from a 1545nm measurement. (a) Single photon pulses are selected with the Matlab *findpeaks* function using the peak selecting attributes *MinPeakHeight* (*MPP*) and *MinPeakProminence* (*MPH*). (b) The average pulse shape in phase as a function of time t with its $\pm 3\sigma$ uncertainty. A pulsewindow of 256 μs has been used. (c) Typical power spectral density (PSD) estimates in phase as a function of frequency f. We plotted the PSD$_\theta$ estimate of the average pulse seen in panel (a) in blue, the average PSD$_\theta$ estimate of the noise in orange and the average PSD$_\theta$ estimate of all pulses in yellow. Note that the latter can be found by adding the two others. (d) The effect of the optimal filter on the distribution of pulse heights. The average of the distribution slightly increases when the optimal filter is applied, improving the resolving power of the detector.

6

Near-IR Detector Performance

In this chapter we present the results of measurements with the near-IR LEKID at 3.8 μm and 1545 nm. Firstly, we explain the experimental setup specific to the measurements in this chapter. Secondly, we compare the pulse rates of the different measurements and prove single-photon detection at 3.8 μm. Following on that, discuss the accuracy of our theoretical model in predicting the absorbed powers. Lastly, we compare the detector (and setup) performance at both wavelengths before summarising the most important conclusions.

6.1. Experimental Setup

The near-IR detector is located on LT192chip1. It is a hybrid, lumped element device with an NbTiN IDC and β-Ta inductor, see Figure 6.1. To increase optical coupling a fused silica microlens array on placed on top. The device is optimised for the optical and near-IR wavelenghts with resolving powers at these wavelengths of about 5 [18]. The resonance frequency of the detector is f_0=7.6538 GHz.

The optical filter configuration consists of 4 bandpass filters at 3.8μm (BP3.8), a neutral density filter of order 3 (ND3) and a germanium window, see Figure 6.1.

At 1545 nm we use a closed setup with a laser source and at 3.8 μm an open setup with a monochromator source, see section 4.1. The laserpower at 1545 nm is set to 50 nW with 46 dB attenuation, which is equal to 1.26 pW. The monochromator is set to 3800 nm. The width of the exit slit is set to 1 mm so we understand the bandwidth of the monochromator light to be 25.8 nm. This is well within the 209 nm full width bandwidth of the 3.8 μm bandpass filters.

6.2. Measured pulse rates

In Figure 6.2 an overview is presented of the different pulse streams for every measurements during an arbitrarily chosen time period of 1 s. The top row is from the 3.8 μm measurement at a temperature of T=27 mK and the bottom row is from the 1545 nm measurement at T=22 mK. The *laser on* measurements at 1545 nm are done at a slightly different temperature compared to the *laser off* measurement (T= 31 mK) because of technical difficulties with the cooler. However, the change from 22-31 mK should not matter for response or for the noise, so the comparison to 3.8 μm measurement is still valid. The peak selection criteria (see section 5.1) that were used were *MPH=MPP*=0.3, for both the 1545 nm and 3.8 μm data.

For the 3.8 μm data we see that the *monochromator off* measurement at 3.8 μm is not dark at all: on average 115 photons/s are present. We see an increase of 336 photons/s for the *monochromator on* measurement.

The *laser off* measurement at 1545 nm is not completely dark either; on average 2 pulses per second are seen to be present.

Nevertheless, we see from the *laser on* measurement that the laser adds 92 pulses per second on average. Only about 9% is rejected at 1545 nm versus 27% at 3.8 μm. This is because the pulse rate at 3.8 μm is almost 5 times higher, leading to more overlapping pulses.

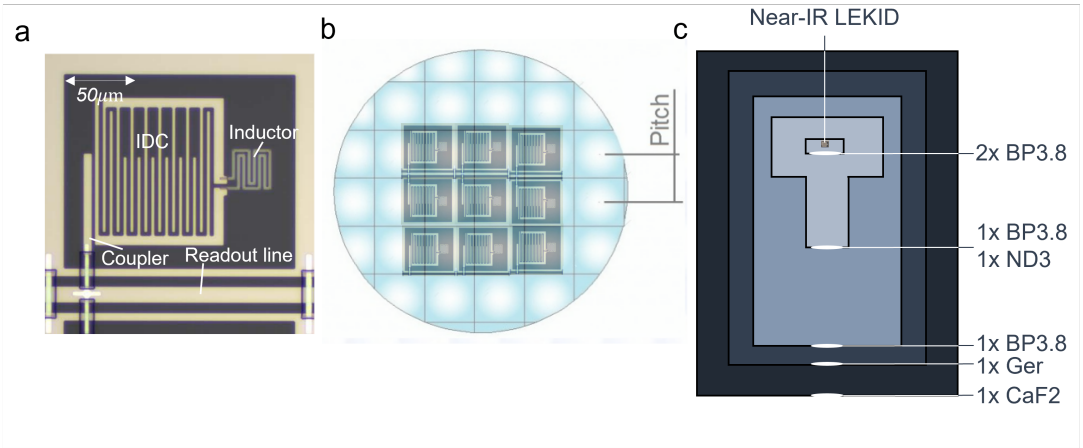

Figure 6.1: (a) Micrograph of a single near-IR LEKID [18]. The coupler is connected to the NbTiN coplanar waveguide (CPW) readout line with a galvanic contact. The resonator is made of a NbTiN interdigitated capacitor (IDC) and a meandering β-Ta inductor. The fingers and gaps of the IDC are 2 μm wide as is the inductor line. (b) The microlens array that is placed on top of the near-IR detector array. The array is made of 1.25 mm thick fused silica and has positive orthogonal lenses with pitch D=150$\pm$1 μm, radius 390 μm$\pm$5% and focal length F=850 μm$\pm$5%. (c) The optical filter configurations for the measurements at 3.8 μm. The corresponding filter transmission spectra are presented in Figure 4.4. All filters have a thickness of 1 mm except for the 6 mm thick, CaF_2 vacuum window.

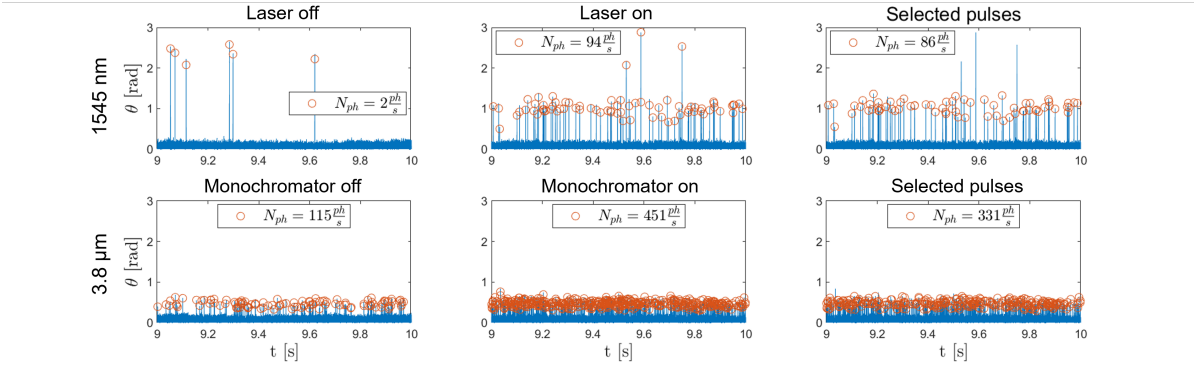

Figure 6.2: Overview of the pulse selection process for (top row) the 3.8μm and (bottom row) the 1545nm measurements. The peak selection criteria that were used were *MPH*=*MPP*=0.3 for both the 1545 nm and 3.8 μm data. The left column shows the data of the dark measurement with the monochromator/laser turned off. It is clearly visible that the 3.8μm setup is significantly less dark than the 1545nm setup. The middle column shows the increase in pulses when the monochromator/laser are turned on. The right column shows the decrease of selected pulses due to the filtering of cosmic rays, too tightly spaced pulses or multiple photon pulses.

We will now more clearly proof that the pulses we see in Figure 6.2 are indeed caused by 3.8 μm photons. For this purpose we plot the pulse height histogram fro three measurements: *monochromator off*, *monochromator on at set to 3800 nm* and *monochromator on and set to 3700 nm*. These histograms are plotted in Figure 6.3. We see nearly the same distribution of pulse heights when the monochromator is off and set to 3.7 μm. We also see a significant increase of pulses with the same heights when the monochromator is set to 3.8 μm. This proves the additional pulses we detect at 3.8 μm are generated by the monochromator as nothing else has changed between these measurements. We can also conclude that the pulses seen in the other distributions originate from the thermal background as these pulses have the same average pulse height. We can also conclude that the resolving power of the detector is not limited by the monochromator or the bandwidth of the bandpass filters. This is because the width of the distribution corresponds to a larger wavelength range of absorbed photons, assuming linearity between phase response and photon energy, than can be accounted for by the monochromator and bandpass filters.

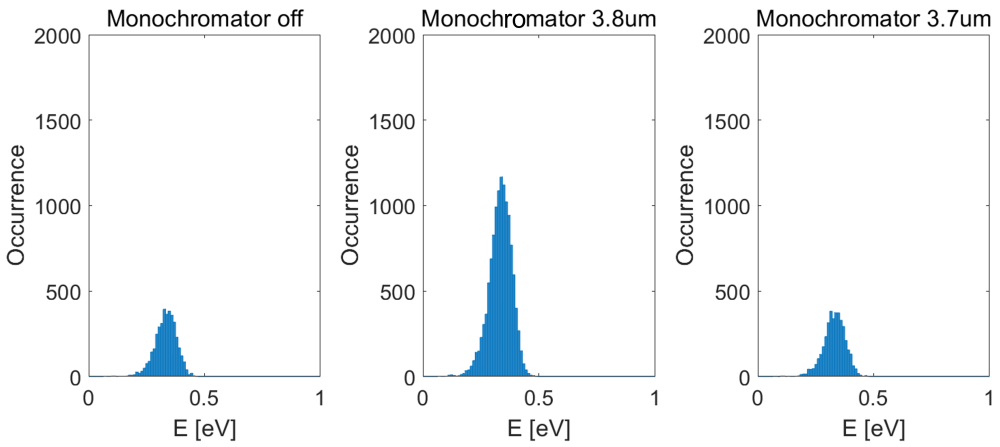

Figure 6.3: Histograms of the pulse heights for the experiments where (left) the monochromator was turned off, (middle) set to 3.8μm and (right) set to 3.7μm. The increase in the distribution for when the monochromator is set to 3.8μm proves that most pulses are caused by the absorption of 3.8μm photons and that the 3.8μm pulses in the left and right distributions originate from the thermal background.

6.3. Comparing to the theoretical model

The expected radiated and absorbed powers have been computed using the model described in section 4.2. The results from the model are presented in Table 6.1

In-band For the absorbed power in the in-band P_{abs}^{in} we expected to have a photon count rate of $N_{ph,in}$=570$\pm$239 photons/s. The experimental data reveals a photon count rate of 116 photons/s which is obtained by averaging over the 40s time stream with the monochromator turned off. The experimental result differs 4σ from the predicted outcome, so the model is not really accurate. However, the model can still be used as tool for designing the optical configuration of the setup.

Near-band We did not expect to see detectable pulses from the near-band as $P_{abs}^{near} \ll P_{abs}^{in}$. We can conclude this was true for our measurements even if the model is only correct to the order of magnitude.

Out-of-band We computed P_{abs}^{out}=3.4$\pm$1.4$\times10^{-19}$ W which would be factor 100 smaller than P_{abs}^{in}. This is the same order of magnitude as the upper limit we required in Figure 4.2: P_{abs}^{in}<9.9$\times10^{-19}$ W. If this is true to the order of magnitude, we can conclude that the number of quasiparticles generated by the background at any given moment is in the order a factor 1000 less than generated per photon at 3.8 μm.

The model should be made more accurate by implementing the factor that were left out, see the end of Figure 4.2. Furthermore, an effort should be made to characterise the thermal background more accurately, especially at 3.8 μm. Now we model the background as a perfect black-body located at the

vacuum window with a relative uncertainty of 20%. This should be re-iterated. It will also be helpful if we would measure and/or model the effect of cryogenic temperatures on the neutral density filters. This might also be a probable cause of the lower in-band power we measure.

Table 6.1: Overview of the relevant powers computed for the configuration that is seen in Figure 6.1. The theoretical model described in chapter 4 was used for this. We also show the in-band photon count rate $N_{ph} = P_{abs}/E_{ph}$. The uncertainties are $\pm 2\sigma$. A analysis of the different contributions to the uncertainty is presented in Table 4.1

	P^{in}	P^{near}	P^{out}	P^{tot}
P_{rad} [W]	$3.7\pm0.1\times10^{-16}$	$5.8\pm1.9\times10^{-21}$	$2.6\pm0.8\times10^{-15}$	$2.9\pm0.9\times10^{-15}$
$N_{ph,rad}$ [photons/s]	7140 ± 2304			
P_{abs} [W]	$3.0\pm1.2\times10^{-17}$	$4.0\pm1.7\times10^{-23}$	$3.4\pm1.4\times10^{-19}$	$3.0\pm1.2\times10^{-17}$
$N_{ph,abs}$ [photons/s]	570 ± 239			

6.4. Comparing detector performance

We now compare the performance of the detector at 1545 nm and 3.8 μm, see Figure 6.4 and Table 6.2. It is important to compare the quality factor Q as it is related to the responsivity. We calculate that the average response $\langle E \rangle$ decreases proportionally with photon energy when also correcting for the small difference in Q, Equation 3.26. This confirms that we are in the small response regime, see section 5.2.

We see that the internal quality factor Q_i is much higher at 3.8 μm than at 1545 nm. This is probably because there is additional stray light, as was noted in section 6.2. It is known that this radiation is comes from the laser fiber, even when the laser is turned off [56]. This was showed in a measurement where the pulses disappeared when tape was covering the end of the laser fiber. The is probably because the fiber comes from a 300 K environment without being attenuated at the colder temperatures stages. To get a better idea of the different noise contributions in both experiments we plot the PSD estimates for a larger bandwidth, see Figure 6.5. Both measurement are seen to have a lot of photon noise present. We investigate this by obtaining the quasiparticle lifetimes τ_{qp} from fitting $y = a\exp(-x/\tau_{qp})$ to the tail of the average pulses, see Figure 6.4. This gives a measure of the background power present in the detector [57]. Indeed, we find a longer lifetime at 3.8 μm than at 1545 nm, there must be more background radiation present in the 1545 nm measurement. We do see 50 Hz contribution in the 1545 nm PSD estimate. This probably has an electrical cause. Also, more contributions are seen at other frequencies. More research should be done into the origin of this stray light in the laser fiber and its effect on the measurements.

The stray light at 1545 nm is probably the cause of the resolving power R being lower than for other measurements with similar devices (R 5 [18]).

Nonetheless, we can conclude that measurements with this device at 8.5 μm will be pointless. R is expected to be more than a factor two lower at 8.5 μm than at 3.8 μm. This will be too low to reliably distinguish pulses.

Table 6.2: Near-IR detector performance at 1545 nm and 3.8 μm. The resonance frequency of the detector is 7.6538 GHz. The readout power is -104 dBm for both measurement. The temperature was 22 mK for the 1545 nm measurement and 27 mK for the 3.8 μm measurement.

	$\langle H \rangle$ [rad]	Q	Q_i	τ_{qp} [μs]	R	R_i	R_{SN}
1545 nm	1.1	2.54×10^4	1.98×10^5	52	3.5	3.7	9.9
3.8μm	0.5	2.51×10^4	5.78×10^5	86	3.2	4.1	5.0

6.5. Conclusion

We list our most important conclusions from our measurement with the near-IR LEKID:

- We have proven single-photon detection at 3.8 μm with a resolving power of about 3
- The measured in-band power was found to be 4σ below the theoretically predicted value. This makes the model only good for estimating powers to the order of magnitude.
- More background radiation was found to be present in the 1545 nm measurement than in the 3.8 μm measurement. This is caused by stay light coming through the laser fiber.This has lowered the resolving power found at this wavelength.

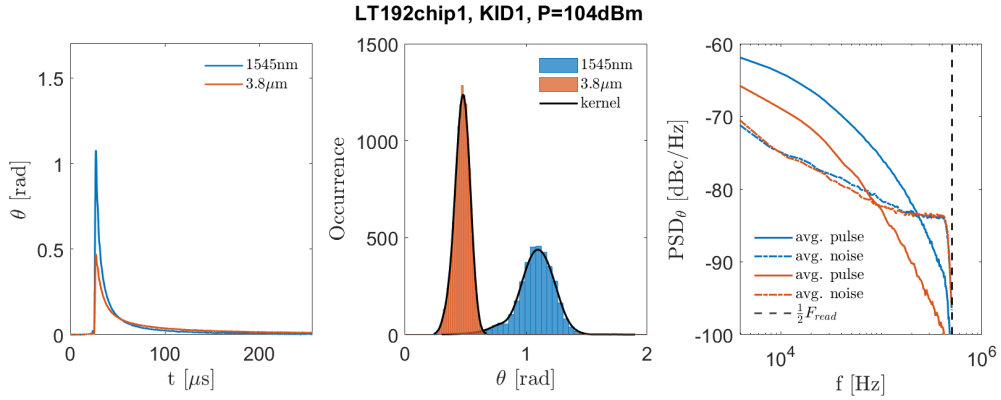

Figure 6.4: Near-IR detector performance at 1545 nm and 3.8 μm. The resonance frequency of the detector is 7.6538 GHz. The readout power -104 dBm. The temperature was 22 mK for the 1545 nm measurement and 27 mK for the 3.8 μm measurement. (left) The average pulse response in phase θ as a function of time t. A pulsewindow of 256 μs was used. (middle) The pulse height distribution resulting from the optimal filter and the kernel fit that is used to obtain the resolving power R. (right) The power spectral density (PSD) estimates of the average pulse and the average PSD estimate from 100 segments of noise. These PSD estimates are used to obtain the signal-to-noise resolving power R_{SN}, see Equation 5.6

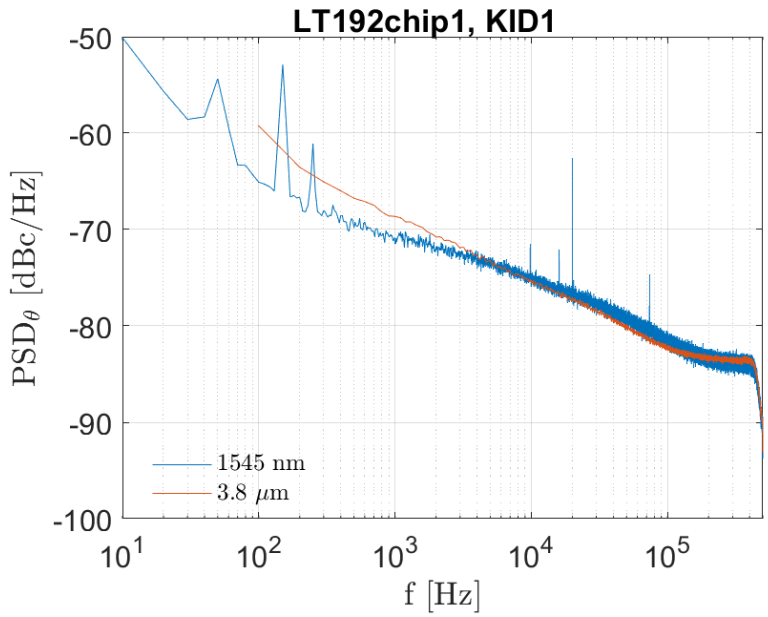

Figure 6.5: Noise power spectral densities (PSD) estimate of the near-IR detector for the 1545 nm measurement and the 3.8 μm measurement. The readout power is -104 dBm in both measurements. The temperature was 22 mK for the 1545 nm measurement and 27 mK for the 3.8 μm measurement. The bandwidth for the 3.5 μm measurement is less than for the 1545 nm measurement because pulses present in the noise limit the maximal obtainable window size for the PSD. Both measurement are seen to have similar photon noise present with slightly less for the 3.8 μm measurement. The roll-off corresponds to the τ_{qp} of both measurements, see Table 6.2. For the 1545 nm measurement the PSD has 50 Hz contribution which probably has an electrical cause. Also, contributions are seen at other specific frequencies for which the causes are unknown.

7

Far-IR Detector Performance

In this chapter we present the results of measurement done with the far-IR MKID at 1545 nm, 3.8 μm and 8.5 μm. These are the very first measurements we have ever done at 8.5 μm. Firstly, we will explain the experimental setup specific to these measurements. This includes a detailed description of the detector, the optical filtering configurations and radiation sources. Secondly, we present the results in two parts: the first part will compare a single detector across all three wavelengths and the second part will compare different detectors at the same wavelength. Lastly, we present our most important conclusions from this chapter.

7.1. Experimental setup

The general detector geometry of the far-IR MKIDs (LT218chip1) is seen in panel a and b of Figure 7.1. The far-IR MKID is designed as an ultra-sensitive, photon-integrating detector for 200 μm radiation through coupling with a leaky-slot antenna [16]. Nonetheless, it has also been able to detect single-photons at 38 μm [24] and based on the response at 38 μm it is even expected that it can do single-photon detection across the mid-IR for which the near-IR LEKID was not sensitive enough, see chapter 6. This makes the far-IR MKID a very relevant detector in our research.

However, it is important to understand that in the mid-IR the detector effectively functions as having an absorber design because the antenna does not couple mid-IR radiation. The radiation is directly absorbed in the aluminium THz line instead. So, the near- and far-IR detectors are both considered to be absorber designs for mid-IR wavelengths despite their differences. Our main goal here is to prove that MKIDs can do single-photon detection at 8.5 μm. Secondary to that, we want to investigate how these differences affect the detector performance in the mid-IR. The major differences between the near- and far-IR MKID are:

- the far-IR MKID has an Al absorber while the near-IR LEKID has a β-Ta absorber. This will affect the optical efficiency and the response of the detector.
- the absorber geometry is very different. For the far-IR MKID it is a straight line with only the very end in focus of the lens, while the near-IR LEKID has a square inductor at the focal point of the lens. This effects the optical efficiency.
- the far-IR MKID absorber is suspended on a SiN membrane, reducing phonon-loss
- the far-IR MKID has a IDC with larger structures, decreasing TLS noise
- the far-IR MKID has a 40 nm, β-Ta mesh which rejects THz stray radiation

It is highly uncertain what the exact radiation coupling will be across the mid-IR. It might be that long-wavelength background radiation will have a greater impact on the measurement than it had for the near-IR LEKID because the detector is optimised for those wavelengths. It may also be that we see pulses arising from photons that are absorbed in the SiN membrane because the detector is so sensitive. Therefore, we cannot construct a theoretical model of the optical efficiency of the MKID and therefore we focus only on the analysis of the detector response and sensitivity.

We compare three different detectors in this chapter: KID5, KID10 and KID21. We choose these detectors as they are one of the few that have a response within the small response limit. They also have three different absorber volumes (THz line, see Figure 7.1a). It will be interesting to see how this will affect the performance. We cannot compare all three detectors at all three wavelengths as they are not within the small response limit at all wavelengths, see section 5.2. We briefly describe each detector:

KID5 has a resonance frequency of f_0=2.74 GHz and the length of its THz line is 913 μm. The readout power is -115 dBm at 1545 nm and 8.5 μm and -113 dBm at 3.8μm. We compare the performance of this detector at all three wavelengths. Its average pulse response at 1545 nm is just about 1.5 rad. However, as many pulses also have heights above 1.5 rad, we should be careful in drawing definite conclusions about the resolving power. Peak selection at 1545 nm and 3.8 μm is done using *MPP=MPH=1* and at 8.5 μm using *MPP=MPH=0.7*.

KID10 has f_0=3.34 GHz, a THz line length of 663 μm and is read out with -116 dBm power. Its response at 1545 nm and 3.8 μm is too high so we only compare it to KID5 and KID21 at 8.5 μm. Peak selection has been done with *MPP=MPH=0.8*

KID21 has f_0=4.55 GHz, a THz line length of 113 μm and is read out with -103 dBm power. We compare this detector only at 3.8 and 8.5 μm. At 3.8 μm we use *MPP=MPH=0.7* and at 8.5 μm *MPP=MPH=0.5*

The optical filter configurations for the 3.8 μm and 8.5 μm measurements are both seen in Figure 7.1c. At 3.8 μm we have added an additional ND3 filter compared with the near-IR LEKID. At 8.5 μm we have replaced the BP3.8 filters with pairs of BP8.5 and CaF_2 filters, but at the sample stage there was only room for one CaF_2 filter. All filters are 1 mm thick, except for the 6 mm thick, CaF_2, vacuum window. The relevant filter spectra are seen in Figure 4.4. All measurements are done at a temperature between 99-102 mK.

The laser power for the 1545 nm measurement is set to 20 μW with 11 dB attenuation, equal to 1.59μW. For the 3.8 and 8.5 μm measurements the same slit and grating are used as described in section 6.1.

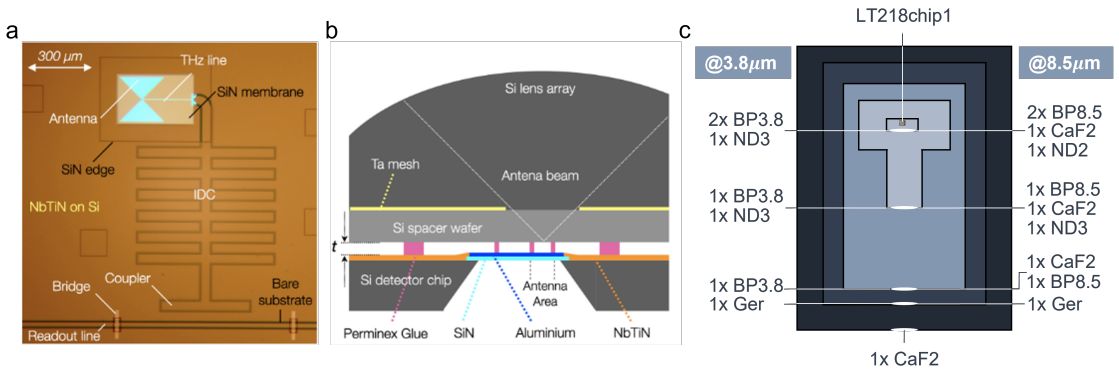

Figure 7.1: (a) Micrograph of a single detector, consisting of a NbTiN CPW line loaded with an IDC coupled, to the readout line via a coupling structure. Its shorted end consists of an aluminium CPW (THz line) that is 400 nm wide, 16 nm thick and has a length that can vary from 113 μm to 913 μm. The THz line is thought to function as a direct absorber for mid-IR radiation in our experiments, as the leaky-slot antenna cannot couple these short wavelengths. The THz line is suspended on a thin SiN membrane, which is highlighted by the backlighting in the micrograph. (b) Cross-sectional diagram of the detector assembly (not to scale). The detector chip, as depicted in panel a, is coupled to a Si lens array using a spacer wafer with a Ta absorbing mesh, with an opening aligned to the antenna to enable radiation coupling. The vacuum gap t is created using spin-on PermiNex® glue pillars as indicated. The graphs in panel a and b are adapted from [16]. (c) The optical filter configurations for the 3.8 μm and 8.5 μm experiments. The corresponding filter transmission spectra can be seen in Figure 4.4. All filters have a thickness of 1 mm except for the 6 mm thick, CaF_2 vacuum window.

7.2. Results

All the results in this chapter are presented in Table 7.1. We compare the detectors at their appropriate wavelengths as explained in the previous section. Additionally, we compare the results of an

alternative 3.8 μm measurement where we replaced the ND3 filter on the sample stage with an ND2 filter, see Figure 7.3c. We will zoom in on Table 7.1 part by part in the following subsections. Firstly, we will compare the performance of KID5 across all three wavelengths. Secondly, we compare the performance of KID5 and KID21 at 3.8 μm. Finally, we compare the performance of KID5, KID10 and KID21 at 8.5 μm.

Table 7.1: Far-IR detector performance at the different wavelengths. The resonance frequencies of KID5, KID10 and KID21 are 2.74, 3.34 and 4.55 GHz respectively. The absorber volumes are 5.84, 4.24 and 0.773 μm^3 respectively. Not all detectors are compared at all wavelengths because we require their response to be within the small response limit. Additionally, we compare the results of an alternative measurement at 3.8 μm where we replaced the ND3 filter on the sample stage with an ND2 filter, see Figure 7.3c.

		P_{read} [dBm]	$\langle H \rangle$ [rad]	Q	Q_i	τ_{qp} [μs]	R	R_i	R_{SN}
1545 nm	*KID5*	-115	1.43	3.79×10^4	2.74×10^5	287	3.85	3.90	25.4
3.8 μm	*KID5*	-113	1.55	3.67×10^4	4.61×10^5	268	8.05	9.02	17.8
	KID5, ND2	-115	1.59	3.48×10^4	2.06×10^5	147	5.82	7.80	8.73
	KID21	-103	1.46	7.81×10^3	1.13×10^4	27	8.18	9.75	15.04
8.5 μm	*KID5*	-115	0.84	3.96×10^4	3.63×10^5	203	3.73	4.80	5.94
	KID10	-116	1.13	3.00×10^4	2.88×10^5	84	4.26	5.03	8.01
	KID21	-103	0.75	6.55×10^3	1.07×10^4	29	4.51	5.43	8.12

Comparing the same detector across all wavelengths

Firstly, we investigate the absorbed powers at the different wavelengths. The photon pulse rates for the laser/monochromator off, on and the selected pulses for all three experiments are seen in Figure 7.2. We list some noteworthy observations:

- the 1545 nm and 3.8 μm setups have no distinct pulses present in the laser/monochromator off measurements, while the 8.5 μm setup still has an average pulse rate of 62 ph/s.
- The monochromator only adds about 1 ph/s on average at 3.8 μm. This is due to the low monochromator power and heavy ND filtering. We increase the measuring time at 3.8 μm from 40 s to 200 s to increase the number of photons. However, about 200 photons is still a fairly little amount for accurate statistics. Measurements were also done with less attenuation, see Figure 7.5 and Table 7.1. This led to more photons but also increased noise levels significantly, worsening the resolving power.
- The monochromator does not add any power at 8.5 μm, the slight difference in detected photons is just a deviation from the average. This confirms our expectations, see section 4.1.
- The 1545 nm laser is seen to add 154 ph/s at 1.59 μW power where it added 92 ph/s at 1.26 pW power for the near-IR LEKID. The difference in power is approximately a factor 10^6. So, it seems that the detector is very inefficient at 1545 nm. The monochromator adds 1 ph/s on average at 3.8 μm, where it added 336 ph/s for the near-IR LEKID. However, this corresponds with the increased attenuation due to the additional ND3 filter. So, at 1545 nm we have ended up with a similar absorbed power as for the near-IR LEKID, while we have increased the radiated power significantly. However, at 3.8 μm the absorbed power has scaled with the radiated power. This might be due to the optical coupling being different at different wavelengths. No definite conclusions can be made about the optical efficiency as long as we do not know more about the optical coupling.
- Furthermore, we see that 40% of the 1545 nm and 50% of the 8.5 μm pulses are rejected. This appears to happen for different reasons. For the 1545 nm data this is because a pulses are either too closely spaced to one another or have secondary peaks. Not much improvement can be made here with respect to the data analysis. If we want to increase the number of singe-photon pulses, we could increase measurement time and/or reduce laser power.

At 8.5 μm this is different as the majority of pulses are simply poorly aligned and are then rejected, see section 5.1. The poor alignment is due to the pulses having a long pulse decay time and low response. If the pulse is long and has low response, it is very likely that the noise in the pulse creates a higher peak somewhere else in the pulse instead of right at the start of the pulse. If the peak is detected somewhere else in the pulse, the pulse often gets misaligned. This should be improved upon in further work. The rejection is not thought to be biased towards a specific pulse height, such that the selected pulses are still deemed representative for the detector performance

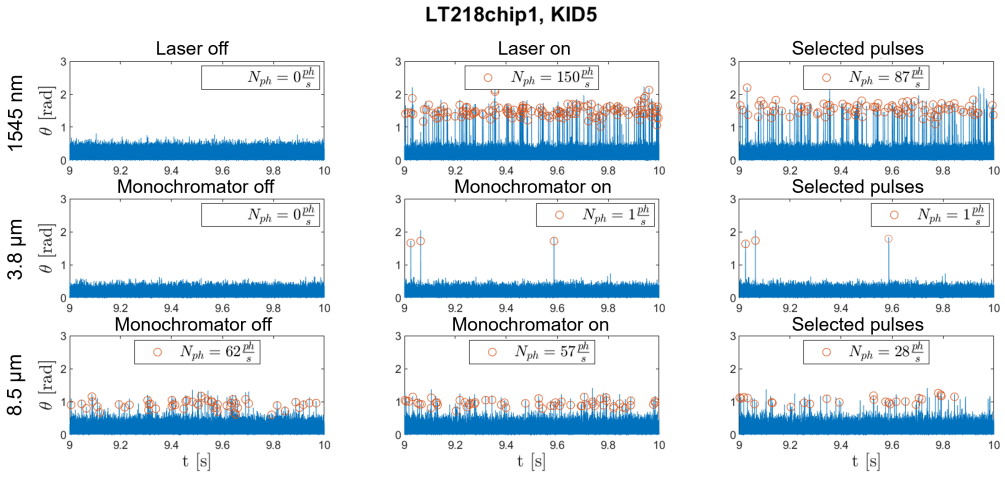

Figure 7.2: Overview of the detected and selected pulse rates for KID5 located on the LT218chip1. The readout power is -115 dBm at 1545 nm and 8.5 μm and -113 dBm at 3.8μm. Peak selection at 1545 nm and 3.8 μm is done with *MPP=MPH=1* while at 8.5 μm with *MPP=MPH=0.7*. The rows from top to bottom are the 1545nm, 3.8μm and 8.5μm measurement. The columns from left to right are the monochromator/laser off measurement, the monochromator/laser on measurement and the pulses selected after filtering.

We now compare the resolving powers for KID5 at the three different wavelengths, see Table 7.1. We have plotted average pulse shapes, the pulse height distributions and the optimal filter models in Figure 7.3 and in Table 7.1. We also compare an alternative filter configuration where we replaced the ND3 filter on the sample stage with an ND2 filter, see Figure 7.5. We list the most important observations:

- Q is limited by Q_c and fairly similar at all wavelengths.
- The amplifier noise only varies slightly across wavelengths, consistent with the slight difference in P_{read}.
- At 3.8 and 8.5 μm we see a growing contribution of a frequency dependent noise in the noise PSD. The nature of this noise is further investigated in Figure 7.4 where we have increased the bandwidth of the PSD. We see that the frequency dependent noise seen in Figure 7.3c is the roll-off of the photon noise. The photon noise increases significantly at 3.8 and 8.5 μm compared to 1545 nm. The roll-off of the photon noise corresponds with the different τ_{qp} in Table 7.1. We conclude that we have significantly more background radiation present at 3.8 μm compared to 1545 nm even though no pulses are detected. Additionally, we confirm the photon noise hypothesis when we replace the ND3 filter at the sample stage with a ND2 filter, see Figure 7.1c. This increases the contribution of the photon noise significantly, lowering the lifetime, see Figure 7.5 and Table 7.1. We also use our theoretical model of the setup (see Figure 4.2) to compute the difference in radiated power at 3.8 and 8.5 μm. It shows almost a factor 14 increase in radiated power on the detector. This increase is mostly in the in-band region. This confirms the fact that we see a lot of photons in the *monochromator off* measurement at 8.5 μm and the increase of photon noise.
- Surprisingly, we see similar average pulse heights at 1545 nm and 3.8 μm where we expected it to decrease with more than a factor 2. The difference in P_{read} is little and not expected to be

the cause of this. We suspect that the pulse response at 1545 nm is lower than it should be because the response between 3.8 and 8.5 μm does scale linearly with photon energy. Probably connected to this is the worse R at we find at 1545 nm compared to 3.8 μm; R is 8 at 3.8 μm and 4 at 1545 nm. We do note that the uncertainty in R is greater at 3.8 μm than for the other wavelengths as the distribution is made with much fewer pulses. The non-linearity of the pulses might also be limiting the resolving power at 1545 nm. Another coordinate system should be used to incorporate the non-linearity of the response, see section 5.2. Another plausible cause might be that at 1545 nm more photons are absorbed in the SiN membrane. The thin, SiN membrane traps phonons making it more likely that pair-breaking energy from elsewhere in the membrane is transferred to the absorber line. This would lead to a greater variation in pulse heights, reducing R. Reasons why we see more of these pulses at 1545 nm might be the difference in optical coupling and/or the higher photon energy.

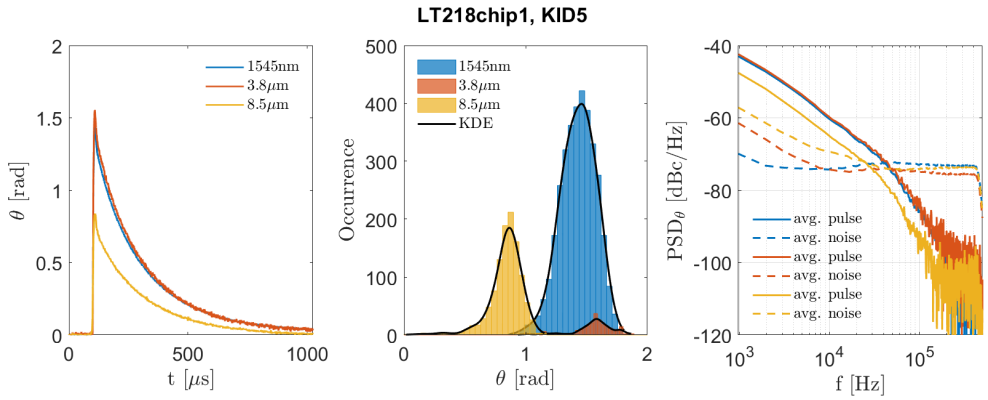

Figure 7.3: Overview of the detector performance of KID5 located on the LT218chip1. The readout power is -115 dBm at 1545 nm and 8.5 μm and -113 dBm at 3.8μm. Detector temperatures are in between 99-102 mK. The performance is compared at 1545 nm, 3.8 μm and 8.5 μm with (left) the average pulse response in phase as a function of time, (middle) the pulse height distributions in phase and the kernel density estimate and (right) the average pulse and noise power spectral densities in phase (PSD$_\theta$). The frequency dependent noise contribution seen in the right panel is due to the roll-off of the photon noise.

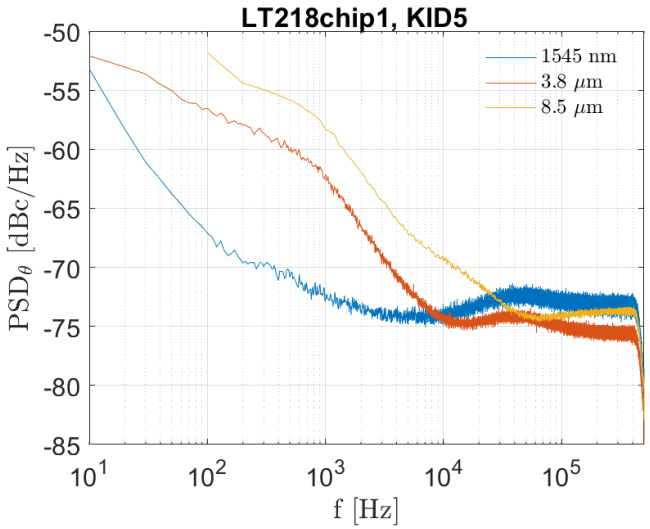

Figure 7.4: Noise power spectral densities in phase (PSD$_\theta$) of KID5 located on the LT218chip1 at 1545nm, 3.8 μm and 8.5 μm. The readout power is -115 dBm at 1545 nm and 8.5 μm and -113 dBm at 3.8μm. Detector temperatures are in between 99-102 mK. The bandwidth at 8.5 μm is less than for the other because pulses from background radiation limit the maximal obtainable window size for the PSD. Pulse rejection has been applied with *MPP=MPH=1* at 1545 nm and 3.8 μm. At 8.5 μm we have applied *MPP=MPH=0.6*. The roll-off of the photon noise corresponds with the different τ_{qp} seen in Table 7.1.

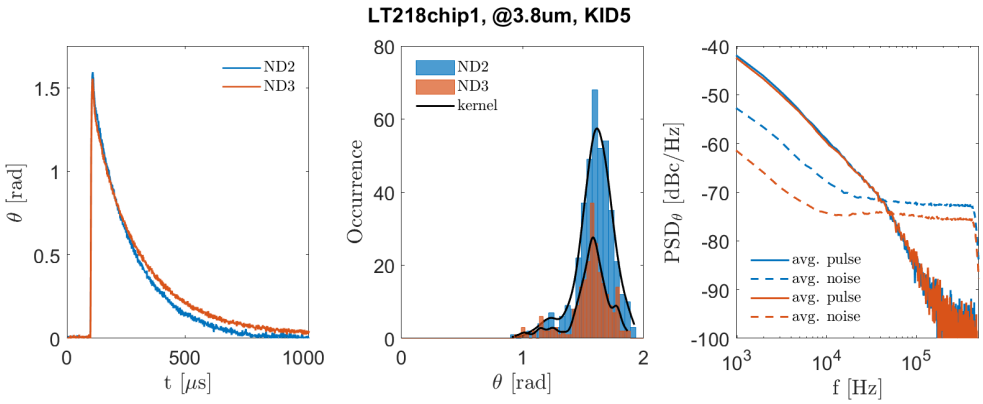

Figure 7.5: Overview of the detector performance of KID5 located on the LT218chip1 at 3.8 μm for two different filter configurations. The first configuration is equal to Figure 7.1c and is labeled *ND3*. The second configuration has a ND2 filter at the sample stage instead of the ND3 filter and is labeled *ND2*. The readout power is -115 dBm for *ND2* and -113 dBm for *ND3*. Detector temperatures are in between 99-102 mK. (left) The average pulse response in phase as a function of time. The pulses have the same average height but *ND2* has a shorter τ_{qp}.(middle) The pulse height distributions in phase. We see an increase in the number of pulses for *ND2*, just as we would expect. For both configurations the number of pulses is quite low. This causes a larger uncertainty in the resolving power R which is obtained from the kernel density estimate. (right) The average pulse and noise power spectral densities in phase (PSD$_\theta$). We see that the pulse PSD$_\theta$ is similar but the noise PSD$_\theta$ has increased significantly for *ND2*.

Comparing different detectors at the same wavelength

We compare the performance of KID5 and KID21 at 3.8 μm in Figure 7.6 and KID5, KID10 and KID21 in Figure 7.7. The results are presented in Table 7.1. We list noteworthy observations:

- Both at 3.8 μm and 8.5 μm we see that τ_{qp} inversely scales with the absorber volume V. This is not what is expected from theory. The shorter lifetimes indicate the increase of the quasiparticle density n_{qp} in the detector. However, it is unclear how the volume would effect n_{qp}. The same phenomenon has been observed in [16], but not in the Appendix of [58] with similar aluminium absorber MKIDs.
- We see that at both 3.8 and 8.5 μm the average pulse heights of KID5 and KID21 are similar, even though their volumes differ a factor 8. However, we also see that Q has decreased a lot: almost a factor 5 at 3.8 μm and a factor 6 at 8.5 μm. This compensates the response for the decrease in volume, see Equation 3.26. Another effect might be the changing kinetic induction fraction α_k due to parasitic inductance in the IDC [16]. The smaller volume KIDs have a larger IDC and smaller α_k, lowering the response.
- R does not vary significantly across the detectors per wavelength. We find an average R of 8.1 at 3.8 μm and 4.2 at 8.5 μm.

7.3. Conclusions

In this chapter we have analysed the performance of the far-IR MKID at 1545 nm, 3.8 μm and 8.5 μm. The far-IR MKID has not been designed for these wavelengths, but as it is an extremely sensitive device, it has been able to show that single-photon detection is possible at 8.5 μm and it is highly probable that it can do that at 18.5 μm as well. This means that we potentially have a device that can do single photon counting across the entire mid-IR regime (5-20 μm). We list some other important conclusions from the data analysis:

- No conclusions can be drawn about the optical efficiency of the far-IR MKID at all the wavelengths measured here. This should be measured when we make dedicated devices for these wavelengths.
- We have found that the 1545 nm measurement has the least amount of photon noise present. This increases for 3.8 μm and even further for 8.5 μm. The theoretical model also showed a large increase in radiated power on the detector when comparing the setup at 8.5 μm to the one at 3.5 μm.

- Surprisingly, we find a higher resolving power at 3.8 μm than at 1545 nm. Also, the average pulse height is similar at both wavelengths. It is unclear why this might be.
- We find that the quasiparticle lifetime τ_{qp} varies with the absorber volume, as was observed by [16].

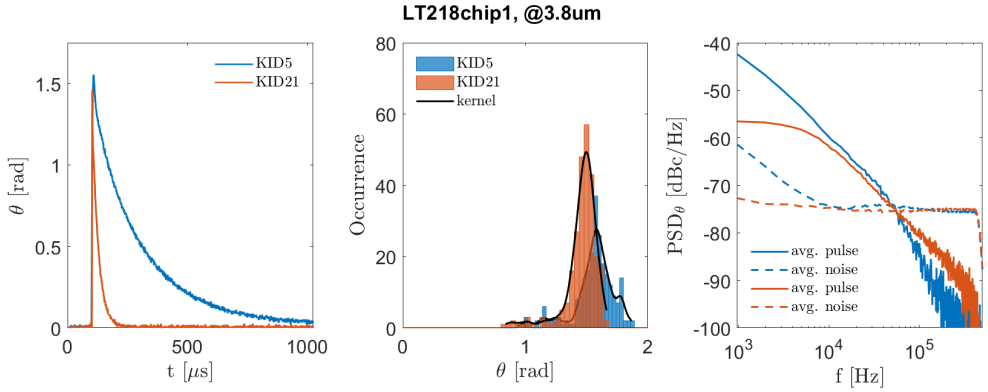

Figure 7.6: Performance of detectors KID5 and KID21 compared at 3.8 μm. P_{read} is -113 dBm for KID5 and -103 dBm for KID21. Detector temperatures are in between 99-102 mK. (left) The average pulse shape in phase as a function of time for both detectors. (middle) The pulse height histogram for both detectors and their kernel density estimate (KSD) that is used to obtain the FWHM of the distribution. (right) The power spectral densities (PSD) of the average pulse and noise model for both detectors.

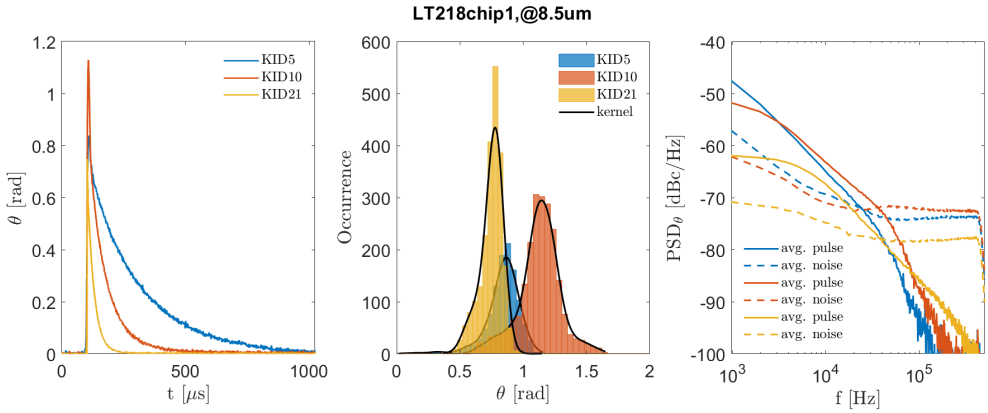

Figure 7.7: Performance of detectors KID5, KID10 and KID21 compared at 8.5 μm. P_{read} is -113, -116 and -103 dBm respectively. Detector temperatures are in between 99-102 mK. (left) The average pulse shape in phase as a function of time for both detectors. (middle) The pulse height histogram for both detectors and their kernel density estimate that is used to obtain the FWHM of the distribution. (right) The power spectral densities (PSD) of the average pulse and noise model for all three detectors.

8

MKID Spectrometer for LIFE

In chapter 6 we found that the near-IR LEKID could do single photon detection up to 3.8 μm. However, its low resolving power made it not possible for single photon detection at much longer wavelengths. In chapter 7 we have experimentally demonstrated that MKIDs can be made sensitive enough for photon counting in the mid-IR band, but the devices used there were very inefficient at these wavelengths. To increase efficiency we investigate if and how we can design the near-IR LEKID such that can do single photon detection across the mid-IR. We investigate the extreme case: single photon counting at 18.5 μm. We construct a model for the signal-to-noise ratio based on the geometry of the MKID. We validate the model with simulations and optimise the geometry for optical efficiency and sensitivity. We start this chapter by posing a general instrument design to constrain our model.

8.1. Spectrometer Design

The general detector design mostly depends on the type of instrument. This can be either be a camera or spectrometer, see Figure 8.1. A camera requires a 2D detector array limiting the detector size by the pixel pitch in two dimensions. A spectrometer only requires a 1D array and only limits the detector size in a single dimension. The other dimension might have a practical limit too, dependent on how the light couples from the dispersive optics, but this is assumed not to constrain our model.

The LIFE initiative will require a spectrometer as the instrument. The spectrometer will consist of multiple spectral channels each covering different parts of the mid-IR bandwidth. For each of these channels we could optimise the detector design such that is works best for that bandwidth. In this chapter we focus on the longest wavelength, 18.5 μm to see if a detector design is realistic across the whole mid-IR bandwidth. There are no specific requirements known yet for the dimensions of the spectral pixels. In our optimisation we constrain ourselves to spectral pixels 25×25 μm^2 in size. This causes the width of the IDC to be limited at 50 μm. The absorber part of the detector is designed as two parallel, straight lines. We use straight lines because having angles in the inductor will cause the current density to increase when it goes around corner [59]. This might cause the critical current to be reach sooner than in a straight line. The critical current is the current density that breaks the superconducting state, analogous to the critical temperature. Therefore, we design the absorber such that all turns are made in NbTiN which has a higher critical current.

8.2. Detector Geometry Optimisation

We want to have a detector that is as sensitive and efficient as possible. Perfectly efficient means that we absorb all of the photons incident on the spectral pixel. Perfectly sensitive means that every absorbed photon leads to a detected pulse while having no false counts. The requirements on optical efficiency and dark current that are posed by the LIFE initiative are presented in section 2.1. We desire a theoretical model that can calculate the optical efficiency and sensitivity given a detector design. We present a model in this chapter based on the geometrical dimensions of the detector. Other aspects like material properties or general design are not considered as they require very different optimisation approaches. The model is based on the near-IR LEKID, see section 6.1. This detector has a lumped element design and a β-Ta absorber. Three detector metrics are important in the optimisation: optical

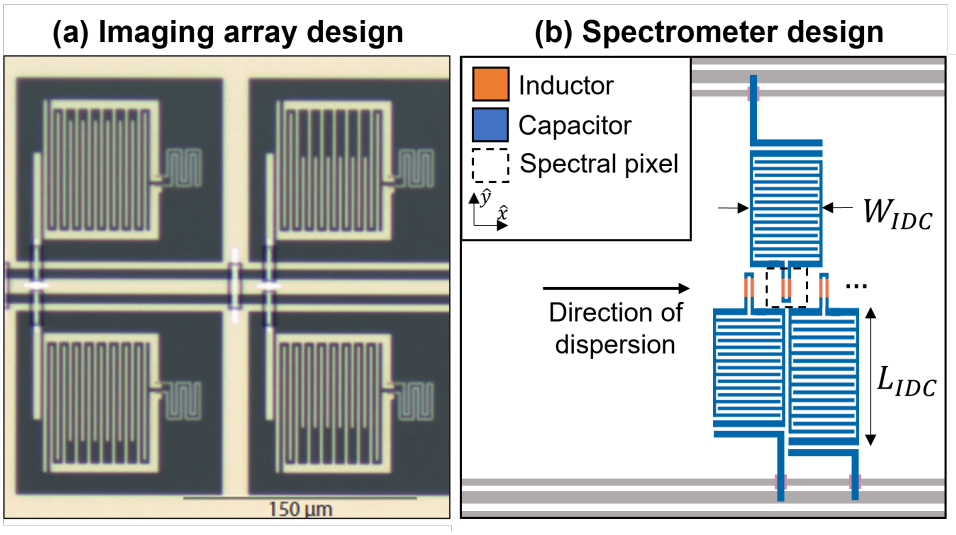

Figure 8.1: Visualisation of the general difference in instrument design for (a) an camera and (b) spectrometer. The camera has a 2D array design constraining the pixel dimensions in two dimensions by the pixel pitch. The spectrometer is a 1D array pf spectral pixels in the direction of the dispersed light. The detector design is based on the β-Ta/NbTiN, lumped element, near-IR LEKID, see section 6.1

efficiency, signal and noise. All these metrics depend differently on the geometry of the detector. Generally speaking, the optical efficiency depends on the absorption surface A, the signal depends on the inductor volume V and the noise scales with the cross sectional area of the inductor, see Figure 8.2a. The exact geometry dependency of every metrics is further explained in their respective subsection. Additionally, there exists a practical constraint in the optimisation: the readout frequency of the detector. The readout frequency, and therefore the resonance frequency f_0 should be between 2-8 GHz. This is because of the readout electronics; no low-noise amplifiers are available for frequencies >8 GHz and amplifiers and amplifiers <2 GHz will be too slow for single-photon counting.

We make a back-of-the-envelope calculation of what general detector geometry we would require at 18.5 μm to do single photon detection. This is important in designing the model for our simulations. From Equation 3.26 we estimate that we need to decrease V with the same factor as we lose in photon energy; this is about a factor 12 between 1545 nm and 18.5 μm. In order to keep the same resonance frequency we have to increase the capacitance C with the same factor, see Equation 3.9. So, we generally need a very different detector as compared to the near-IR LEKID. The general detector model we use in the simulations is seen in Figure 8.2b. Some parameters are unchanged in the simulations while others are varied. The constant parameters are: W=50 μm, $L_{coupler}$=46 μm, g=d=s=2 μm and $L_{overlap}$=42μm.

Optical efficiency

The optical efficiency, η_{opt}, is defined by the ratio of the absorbed power to the total incident power on the pixel. A lot of different parameters influence η_{opt}, some are seen in Figure 4.2 but there are many more, depending on the specific optical design. In the optimisation exercise done in this chapter we only focus on the parameters that are clearly influenced by the geometry of the detector. Therefore, we will first optimise the detector geometry with respect to the signal and noise and then reflect on what this means for η_{opt} and the general optical design.

Signal

The signal of the detector is given by the responsivity. The responsivity scales with the kinetic induction fraction α_k, the volume of the inductor V, and the photon energy E_{ph}

$$\theta \propto \frac{\alpha_k E_{ph}}{V} \tag{8.1}$$

The volume depends trivially on the dimensions through $V = twl$, with t the thickness of the inductor. The kinetic induction fraction is defined as $\alpha_k = L_k/L$ with L_k the kinetic and L the total inductance of

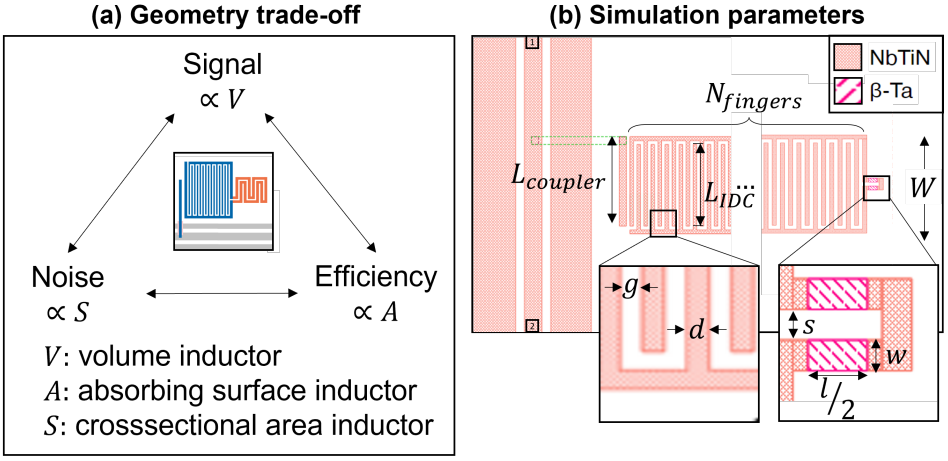

Figure 8.2: (a) A simplistic visualisation of the trade-off that exist between the signal, noise and optical efficiency of a detector. All three metrics depend differently on the geometry of the detector. Important geometry parameters are the volume V, absorbing surface A and cross sectional area S of the inductor. (b) Schematic view of the detector model that is used in the simulations with the relevant parameters indicated. W is the width of the IDC and $L_{coupler}$ is the length of the coupler. $N_{fingers}$ is the number, d the width and L_{IDC} the overlap of the IDC fingers. g is the gap between the IDC fingers. The inductor is parameterised by the width w length l of the inductor line. The inductor lines are separated by s.

the detector. E_{ph} does not depend on geometry, however we will use this dependency later on when we compare the response at 18.5 μm to the response at 1545 nm.

In theory, especially when having a very large capacitor, the total inductance of the detector does not only originate from the inductor part of the detector, but also from the capacitor. The complete definition of the inductance of a detector is then given by

$$L = L_k + L_g = (L_k^i + L_k^c) + (L_g^i + L_g^c) \tag{8.2}$$

where L_g is the geometrical inductance and the superscripts indicate whether it is the inductance is of the inductor, i, or capacitor, c. Simulations are done in Sonnet and compared to analytical models to determine each of these individual contributions to L. We will now discuss the different contributions to L seen in Equation 8.2 based on the results from simulations seen in Figure 8.3.

L_k^c The kinetic inductance clearly depends on the detector geometry as following [60], [61]

$$L_k \approx \frac{\hbar}{\pi\Delta}\frac{l}{w}\frac{\rho}{t} = \frac{\hbar R_s}{\pi\Delta}N_{sq} = L_{sq}N_{sq} \tag{8.3}$$

with $R_s = \rho/t$ being the normal state sheet resistance, obtained from the resistivity, ρ, and $N_{sq} = l/w$ being the number of squares. For the NbTiN we use t=120 nm and R_s=11 Ω resulting in L_{sq}=0.918 pH/sq. For β-Ta we use t=60 nm and R_s=39.8 Ω, giving L_{sq}=54.6 pH/sq. So, L_k^c is a factor 60 lower L_k^i for the same N_{sq}. Therefore, we assume in our model that $L_k^c \approx 0$, but we have not yet been able to show that this is also true for very large IDCs. Additional simulations should be done for purpose.

L_k^i: In Figure 8.3a we plot L_k^i as a function of N_{sq}. L_k^i is obtained in two steps by simulating f_0 for both a detector with a PEC and a β-Ta inductor while keeping the geometry the same. For the PEC inductor holds $L_k^i = 0$ such that $L^{PEC} \approx L_g^i + L_g^c$. L_k^i can now be computed from the difference in f_0 when the capacitance C is known. The analytical model proposed by [62] is used for this. L_{sq} should be equal to the slope of a straight line fitted to the data. We find a slope of $\hat{L}_{sq}$=55.4 pH/sq which is sufficiently close to the true value and thereby confirms the models for the C and L_k^i. The slight difference in L_{sq} is most likely caused by simulation inaccuracies and rounding errors.

L_g^i: In our simulations we design the inductor as two parallel lines that connect both sides of the IDC.

The geometrical inductance for two coplanar flat lines, that are separated by s, is given by [63]

$$L_g^i(w,l) = \frac{\pi l Z}{c \ln\left[2\frac{1+(1-\eta_i^2)^{1/4}}{1-(1-\eta_i^2)^{1/4}}\right]} \forall \ 0 < \eta_i < \sqrt{2}/2 \tag{8.4}$$

with $\eta_i = \frac{s}{s+2w}$, $Z = Z_0/\sqrt{(1+\hat{\epsilon_r})/2}$ the impedance of the medium between the inductor lines and c the speed of light in vacuum. We use an average relative permittivity $\hat{\epsilon_r} = (\epsilon_s + 1)/2$ as the lines are in between vacuum (ϵ_r=1) and the c-plane Sapphire substrate (ϵ_s=11.6).

L_g^c: In Figure 8.3b we plot L^{PEC} as a function of l for different w. We observe an offset b in L^{PEC} that is independent from w and l. As L_g^i does depend on w and l we conclude that $b \approx L_g^c$ =984 pH. This is confirmed in Figure 8.3c where we plot $L^{PEC} - b$ as a function of w for different l and see that $L^{PEC} - b \approx L_k^i(w,l)$. Furthermore, see that $L_g^i \ll L_g^c$ for this geometry. We assume that L_g^c linearly scales with $N_{fingers}$ if $N_{fingers}$ is large. $N_{fingers}$ is assumed large when C scales linearly with $N_{fingers}$: $N_{fingers}$ >50.

We now have all the elements to construct a model for the signal θ depending on the geometric dimensions of the detector.

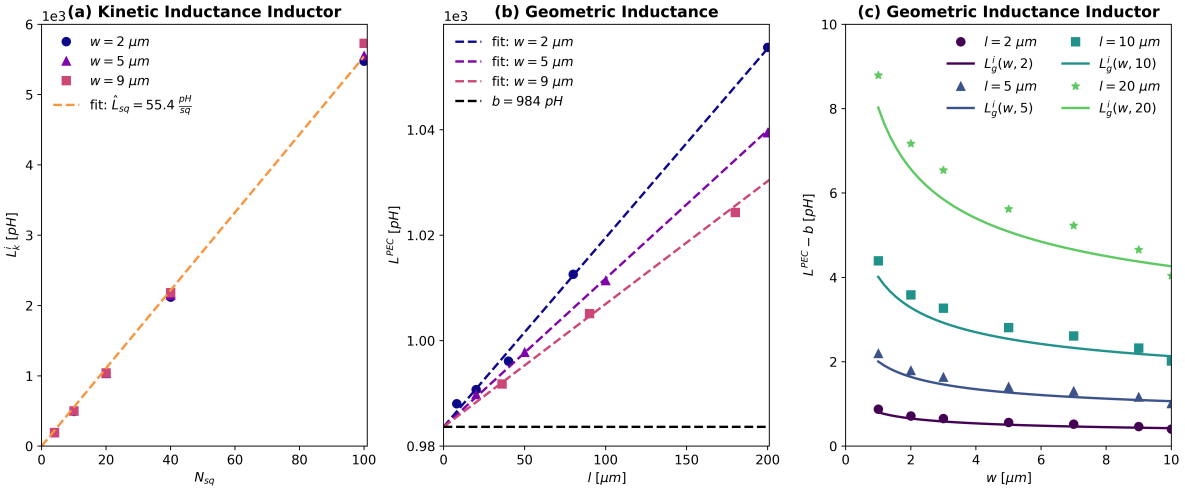

Figure 8.3: Simulations were done for a variety of inductor widths, w, and lengths, l, to estimate all the contributions to the total inductance L, see Equation 8.2. The IDC used in the simulations is characterised by $N_{fingers}$=204, L_{IDC}=42 μm and g=d=2 μm, see Figure 8.2. (a) The kinetic inductance of the inductor L_k^i as a function of the number of inductor squares $N_{sq} = w/l$. L_k^i is obtained from two simulations with the same detector geometry: one with a lossless PEC inductor and the other with a β-Ta inductor. The difference in resonance frequency allows us to compute L_k^i. We fit a straight line through the data and find $\hat{L}_{sq}$=55.4 pH/sq.(b) L^{PEC} as function of l for different w. L^{PEC} is the detector inductance when having a PEC inductor. We fit straight lines to the data and obtain the same offset b in L^{PEC} for all w. b has a value of 984 pH. (c) $L^{PEC} - b$ as a function of w for different l. The solid lines are obtained from the analytical expression for the geometrical inductance of the inductor L_g^i, see Equation 8.4. The data clearly shows the same dependencies on w and l as the model suggests but for larger l a discrepancy starts to appear.

Noise

The main noise sources in the resonator are the TLS and amplifier noise. The amplifier noise scales inversely with the readout power of the resonator

$$N_{ampf} \propto \frac{1}{P_{read}} \tag{8.5}$$

and the TLS noise scales inversely with the square root of the internal power [36]

$$N_{TLS} \propto \frac{1}{\sqrt{P_{int}}} \tag{8.6}$$

The value of N used here is the power spectral density of the noise with no frequency dependence taken into account. The internal and readout power are linearly related through the quality factor of the resonator

$$P_{int} = \frac{1}{\pi}\frac{Q^2}{Q_c}P_{read} \approx \frac{Q_c}{\pi}P_{read} \tag{8.7}$$

where the approximation is only valid when losses in the resonator are small, i.e. $Q_i \gg Q_c$, such that $Q \approx Q_c$. The readout power is constant at $P_{read} = \frac{V_s^2}{4Z_0}$ with $Z_0(\approx 50\ \Omega)$ the characteristic impedance of the readout line and V_s the source voltage. The quality factors are obtained from the simulated $|S_{21}|$ resonance dip resonance dip with $Q = f_0/FWHM$ and $Q_i = Q/S_{21}^{min}$. Q_C is obtained with Equation 3.11.

So, both the amplifier and the TLS noise go down when the readout power is increased, however there is a limit to the internal power that can be applied before bifurcation. An internal power that is too high will cause the resonator to exhibit a non-linear response. For sufficiently high power the resonator can occupy two stable states, which is called bifurcation.

We define, j^*, as the maximal current density that can exist inside the inductor before bifurcation. This value is dependent on material properties and therefore constant in this optimisation. A theoretical relation relating j and P_{int} is derived using the magnetic energy in the resonator, $E_m = \frac{1}{4}L|I|^2$, the internal power, $P_{int} = 2\omega_0 E_m$, and current density as $j = I/wt$. We obtain the relation

$$j = \frac{1}{wt}\sqrt{\frac{P_{int}}{\omega_0 L}} \tag{8.8}$$

This assumes that at resonance the same current is present in the IDC as in the inductor. It is also assumed that the current in the inductor is uniform over its cross sectional area, $S = wt$. This assumption is valid if the magnetic penetration depth, or London penetration depth, λ_L, is greater than the dimensions of the conductor, i.e. $\lambda_L \gg w, t$[39]. If $\lambda_L \ll w, t$ for all the different geometries within this optimisation, a skin-effect would occur where the current mostly resides at the edge of the conductor. However, λ_L then still is independent from the size of the conductor and j would thus only differ a constant factor from the uniform current assumption, making the optimisation still valid. Only when $\lambda \sim w, t$ this is not true and would make the optimisation invalid.

We need to validate Equation 8.8 before we can use it in our optimisation. Therefore, we obtain the maximum current in the inductor, $\tilde{j}_{max}$, from simulations in Sonnet and compare this value to j which we analytically compute with Equation 8.8. In our simulation we independently vary four different parameters: w, N_{sq}, C and $L_{coupler}$. The results are seen in Figure 8.4. If we fit a straight line to the data from all graphs combined we obtain the blue dotted line. The solid blue line represents the relation as stated by Equation 8.8. We notice that nearly all data points lie very close to the blue dotted line. So, we can conclude that the following relation is valid

$$j_{max} \propto \frac{1}{wt}\sqrt{\frac{P_{int}}{\omega_0 L}} \tag{8.9}$$

when w, N_{sq}, C and $L_{coupler}$ are varied. However, there is a constant factor difference between j and $\tilde{j}_{max}$. As of this moment it is not clear what the cause is of this factor, however as it is constant it is not of influence on our model.

C is changed by varying $N_{fingers}$. However, if $N_{fingers}$ >50, C linearly scales with $N_{fingers}$. The relation obtained from fitting a straight line (dotted blue line, $y \propto x$) to all the blue data points that are seen in (d) differs a constant factor from the theory (solid blue line, $y = x$).

When we limit $\tilde{j}_{max} = j^*$, which is constant for all LEKID geometries, we can extract a relation for, P_{int}^*, the maximal power that can be applied before bifurcation

$$P_{int}^* \propto f_0 L(wt)^2 \tag{8.10}$$

Now we can obtain the relation between the minimal noise levels before bifurcation, N^*, and the internal power. For the amplifier noise this is

$$N_{ampf}^* \propto \frac{Q^2}{Q_c P_{int}^*} \propto \frac{1}{(wt)^2}\frac{Q^2}{Q_c}\frac{1}{f_0 L} \tag{8.11}$$

and for TLS noise

$$N^*_{TLS} \propto \frac{1}{wt}\sqrt{\frac{1}{f_0 L}} \tag{8.12}$$

The amplifier noise is dependent on Q_c. We do not know how to compute Q_c analytically from the detector geometry. Other variables factor in, such as the width of the coupling bar and its separation from the IDC. Q_c is a design choice and should be simulated separately. The total noise equivalent power is given by

$$N = \sqrt{N^2_{ampf} + N^2_{TLS}} \tag{8.13}$$

8.3. Results and discussion

We now have a model for the signal and noise of our detector. Let us combine the optimisation of the signal and noise by optimising the signal-to-noise resolving power

$$R_{SN} \propto \frac{\theta}{\sqrt{N}} \tag{8.14}$$

We normalise by the value for R_{SN} that we find for the near-IR LEKID at 1545 nm, R'_{SN}. We do this to know how R_{SN} changes relative to R'_{SN}. This requires computing the response θ', amplifier noise N'_{ampf} and TLS noise N'_{TLS} for the near-IR detector at 1545 nm. We compute θ' using Equation 8.1 with values $\alpha'_k = 1, V = 2 \times 218 \times 0.06\ \mu m^3$ and $E'_{ph} = hc/1545nm$. N'_{ampf} and in N'_{TLS} are computed using Equation 8.11 and Equation 8.12 with values f_0=7.6 GHz, w=2 μm and $L = L_k = 109 \times L_{sq}$. We assume that all other parameters are kept constant between the near-IR LEKID and our model here.

We study two separate cases, one where the detector is TLS noise limited and one where it is amplifier noise limited. We have four optimisation parameters; w, l, t and C. The results of our model are seen in Figure 8.5 with in (a) the resonance frequency f_0, in (b) The relative, amplifier noise limited signal-to-noise: $R_{SN_{ampf}}/R'_{SN_{ampf}}$ and in (c) the relative, TLS noise limited signal-to-noise: $R_{SN_{TLS}/R'_{SN_{TLS}}}$. All of them are plotted as a function of inductor length l. Five lines are visible in every graph. We identify the purple line as the 'default' line with parameters w =2 μm, C =0.47 pF and $t = 60$ nm. The other lines (blue, green, yellow) have the same values, except that one parameters has been varied. This gives us insight in what the effect is of individually changing the parameters:

- all the parameters influence the amplifier and the TLS noise limited relative signal-to-noise in the same general way: decreasing the value of the parameter increases R_{SN}/R'_{SN}. However, the effect is larger for the TLS noise limited case.
- decreasing w from 2 to 1 μm (blue line) gives the largest increase in R_{SN}/R'_{SN}, followed by decreasing t from 60 to 40 nm (yellow line). Decreasing C from 0.47 pF to 0.35 pF (green line) has the smallest effect.
- decreasing t and w decreases f_0, while decreasing C increases f_0.

In both the TLS and amplifier noise limited cases we see that R_{SN}/R'_{SN} < 1 for all l. This means that the signal-to-noise will decrease with respect to what we had at 1545 nm with the near-IR LEKID. However, this is the case if only one parameters is changed. We also plot the black line, for which all parameters have been decreased with respect to their default values. This greatly increases the signal-to-noise.

So, let us try and answer the main question of this chapter: *can we make a realistic LEKID design at 18.5 μm?*

The signal-to-noise at 1545 nm was about 10, see Table 6.2. Assuming we want to maintain this value even at 18.5 μm, and assuming we are in the TLS noise limited case, we would require a inductor with dimensions $1 \times 15 \times 0.04\ \mu m^3$ and a 0.35 pF IDC. This would give us a resonance frequency of f_0=6.2 GHz. In the amplifier noise limited case with the same design, the R_{SN} would decrease a factor 2. This design is not unrealistic to manufacture. The greatest challenge is rather its optical efficiency. It is a very small inductor with only 15 μm^2 of absorbing surface. If we assume that we have the same

optical design at 18.5 μm as at 1545 nm, see Figure 4.5, then the optical efficiency will decrease a lot as the absorbing surface has decreased and the diffraction increased. Future research can look to other options to increase the optical efficiency. Some suggestions are given in chapter 9.

In future work the model presented here could also be applied on a design with a Aluminium inductor. Al has a longer quasiparticle lifetime than β-Ta and this might improve the signal-to-noise. However, probably at the cost of optical efficiency.

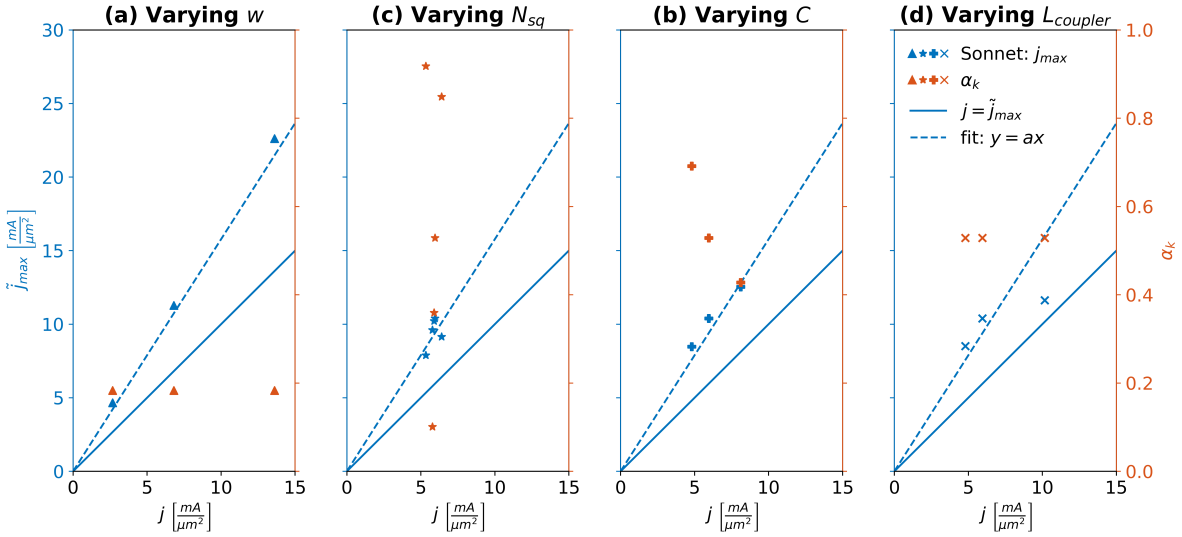

Figure 8.4: The relation between j and $\tilde{j}_{max}$ visualised for four different cases. j is the current density in the inductor analytically calculated with Equation 8.8. $\tilde{j}_{max}$ is the maximum current density in the inductor obtained from Sonnet simulations. The blue markers and lines in all graphs correspond with $\tilde{j}_{max}$ when read from the left y-axis. Every blue marker has a corresponding orange marker, displaced in y, that gives the value of the kinetic induction fraction α_k when read from the right y-axis. The solid blue line represents the relation $j = \tilde{j}_{max}$. The dotted blue line is a fit of a straight line, $y = ax$, to all the blue data points combined from all four graphs. The solid and dotted blue lines are exactly the same in all graphs. As nearly all blue data point lie close to the dotted line we can conclude that the relation $j \propto \tilde{j}_{max}$ is valid. We find that having a 50 μm coupler along the width of the IDC (see Figure 8.2) did not couple enough power to the resonator to obtain the FWHM necessary for determining Q. Instead, a coupler is used that runs alongside the back of the IDC with a length of 200 μm. In (a) the width of the inductor, w, is varied (f.l.t.r w=[5, 2, 1]μm) with a constant number of inductor squares, $N_{sq} = 4$. In (b) w=2 μm and N_{sq} is varied from 2 to 200 and α_k from 0.1 to 0.9. We see that $\tilde{j}_{max}$ is unaffected by the change in N_{sq}. In (c) the inductor size is kept constant while the size of the IDC is varied by changing the number of fingers (f.l.t.r $N_{fingers}$=[100, 200, 300]). In (d) the length of the coupler $L_{coupler}$ was varied. (f.l.t.r $L_{coupler}$=[300, 150, 75]μm). We can conclude that the current density is independent from α_k. All other dimensional parameters regarding the readout, coupling, and material thicknesses were constant in all simulations

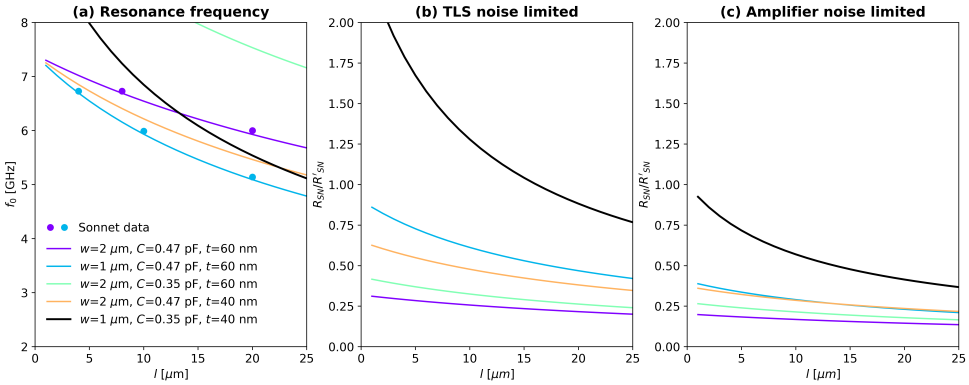

Figure 8.5: Results of the geometric detector model. We vary four different parameters in all graphs: the inductor length, l, inductor width w, inductor thickness t and IDC capacitance C. The legend shows how these parameters are varied for all four graphs. For the blue, green and yellow lines only 1 parameter was changed with respect to the 'default', purple line. For the black line all parameters have been varied. (a) The resonance frequency f_0 as a function of l. Also, data from simulations in Sonnet has been plotted to show the accuracy of the model. These are the dots that have a corresponding color according to the values used in the simulation. (c) The relative signal-to-noise resolving power, R_{SN}/R'_{SN} in case the noise of the detector is limited by the TLS noise. R'_{SN} is the value of R_{SN} at 1545 nm for the near-IR LEKID, see chapter 6. (c) R_{SN}/R'_{SN} in case the detector is limited by the amplifier noise.

9

Discussion and Conclusion

The main objective of this thesis is to investigate how the near- and far-IR MKIDs perform in the mid-IR such that we know what developments are necessary to design a MKID spectrometer for the LIFE initiative. We have done measurements with two different devices. First, we have the near-IR LEKID with a β-Ta inductor designed for imaging arrays in the optical and near-IR regime, see chapter 6. This device has shown single-photon detection at 1545 nm. Second, we have the far-IR MKID with Al inductor, which is designed to be extremely sensitive to radiation at 200 μm but also has shown single photon detection at 38 μm, see chapter 7. We have compared the performance of these devices in the mid-IR at 3.8 and 8.5 μm.

Based on the performance of the near-IR LEKID we have also devised a model to estimate whether a realistic design can be made at 18.5 μm that is sufficiently sensitive for single-photon counting.

A secondary objective of the thesis was to develop an accurate measurement setup for MKIDs in the mid-IR that would enable single photon-counting at 3.8 and 8.5 μm. For this purpose a model has been made to help characterise the setup. The accuracy of the model has been compared with measurements.

Let us now reflect on the progress we have made with this. Firstly, we discuss the mid-IR measurement setup and its theoretical model. Secondly, we summarise the MKID performance in the mid-IR. Lastly, we discuss several improvement to increase MKID performance in the mid-IR.

Mid-IR measurement setup and model

The energy necessary to break Cooper pairs in a superconductor is very low such that photons up to the mm regime can still break Cooper pairs. This means that the radiation emitted by any object with a finite temperature could add to the background noise of our superconducting MKIDs. Especially, objects at room temperature emit most of their radiation in the mid-IR with the peak of their spectral radiance at 10 μm.

Different setups have been designed for the experiments at different wavelengths, see Figure 4.2. At 3.8 and 8.5 μm the radiation source was external to the cryostat and optical filters were used to obtain the desired radiation. We specifically optimised the optical filter configuration for each experiment conducted at a different wavelength or with a different detector. We also did measurement at 1545 nm using a laser as a reference.

The thermal background is either more of a blessing or a curse depending on the wavelength. The thermal background is a curse at 3.8 μm as it adds background noise to the external monochromator source. For the near-IR LEKID we find that there is more background radiation present at 1545 nm than at 3.8 μm. However, this is because of stray light entering the setup through the laser fiber even when the laser is turned off. Measurement with the the far-IR MKID showed that there was more background radiation present at 3.8 μm. Nonetheless, with both detectors we were able to prove single photon detection at 3.8 μm.

At 8.5 μm the thermal background is more of a blessing. This because the monochromator lacks the spectral radiance at this wavelength making the thermal background our only source of radiation. Single photon detection at 8.5 μm could still be done because this wavelength is closer to the peak

spectral radiance of the thermal background, making the optical filtering more convenient. Single photon detection at 8.5 μm has only been possible with the far-IR MKID as the near-IR LEKID lacked the sensitivity. We find that there was more background radiation present at 8.5 μm than 3.8 μm.

A setup has already been designed for measurements at 18.5 μm. At this wavelength a cryogenic black-body can be used as a source rather than the thermal background. The cryogenic black-body emits a well characterised radiation spectrum depending on its temperature. This can be used to shift the peak of spectral radiance of the spectrum to the desired wavelength. Also, tilted filter holders have been designed and manufactured that might improve the background radiation in the setup. This will be done in future work.

We designed a theoretical model of our setup to aid in characterising it. Important in this is that not all the radiation has the same effect on the detector. The setup should be characterised to such an extend that we know what power is absorbed by the detector at what wavelength. Three distinct wavelength regimes have been implemented in the model for this purpose: the in-band, the near-band and the out-of band. The in-band is our desired wavelength. The near-band is the band that still leads to detectable photon pulses. The out-of-band is the continuous background radiation present in the measurements. We also implemented a model to estimate the optical efficiency of the near-IR LEKID, which is used to calculate the absorbed power in the detector. Measurements showed absorbed powers 4σ lower than predicted by the model. The optical efficiency differs greatly with wavelength due to diffraction and the transmission of the fused silica lens, see Figure 4.5.

The model has only been applied quantitatively on the near-IR LEKID. The far-IR MKID has been designed for very different wavelengths and too little is known about the optical coupling in the mid-IR to construct a model for it.

MKID performance in the mid-IR

The LIFE detector requirements are presented in Table 2.1, performance results of the near-IR LEKID in Table 6.2 and of the far-IR MKID in Table 7.1. The results are obtained from analysing the phase response data of the near- and far-IR detectors. We apply an optimal filter to the detected pulses to improve the measured resolving power. The far-IR MKID has the better resolving power at 3.8 μm. It is also the first, detector to show single-photon detection at 8.5 μm. It is also expected that it can show single-photon detection at 18.5 μm. Not per se with the detectors that we have measured in this thesis. These detectors were chosen because they had the lowest responses of all detectors. Most other detectors had photon responses that were too high for our data analysis, but they will likely give a good response at 18.5 μm. So we can conclude that it is possible to do single-photon counting with MKIDs across the mid-infrared. However, at this point in time we do not have sufficient information to compare the optical efficiencies and dark current of our detectors. The focus should thus be to design a dedicated device for the mid-IR, as the detectors used in our measurement are both optimised for a different bandwidth. The measurements of this thesis should be done again but this time with these dedicated devices. With this new devices we could do measurements for the dark current. However, we currently lack the setup to determine the optical efficiency in the mid-IR. The setup that is currently used at 3.8 and 8.5 μm has shown to add thermal background radiation which limits the performance of the detector. We cannot reliably measure the optical efficiency of the detector with such a setup. The cryogenic black-body setup at 18.5 μm will be able to do this, but we lack such a characterised setup for the lower wavelengths. The possibility of using mid-IR lasers should be investigated.

Outlook: LIFE spectrometer

In order to develop a MKID spectrometer for the LIFE initiative we have to improve upon the optical efficiency and sensitivity of the detectors. Ideally we would use the a β-Ta absorber of the near-IR detector as this has a higher optical efficiency. However, the near-IR detector was designed for the optical/near-IR and lacks sensitivity for wavelengths higher than 3.8 μm.

We have constructed a model based on the near-IR detector to assess whether the near-IR design is feasible to be applied at 18.5 μm. The model purely focuses on optimising the geometry of the detector. We constrained our optimisation by posing a spectrometer design and limiting the spectral pixels to 25×25 μm^2, see Figure 8.1b. From the model we conclude that a design that is similar in performance to the near-IR LEKID is realistic (i.e. can be manufactured) at 18.5 μm. This assumes that the detector is TLS noise limited at 1545 nm. The performance would decrease a factor 2.5 for

the same design if the detector is amplifier noise limited. More work is necessary to determine by which noise the detector is mostly limited and how a possible combination of noises effect the model. Generally true is that the detector design would require a very small inductor and large IDC. This is mainly because parasitic inductance in the IDC lowers the response by diluting the kinetic induction fraction. More research in necessary to investigate the effect on the optical efficiency of such a small detector. However, it is not necessary for a single device to cover the whole mid-IR bandwidth. The LIFE spectrometer will consist of multiple spectral channels. So, the general detector design can differ for each of these channels. Within the channels the geometry of the detectors can again be optimised per spectral pixel.

We list some other research directions that can advance the performance of MKIDs in the mid-IR

- using phonon capturing membranes in combination with a β-Ta absorber. This might increase the sensitivity of the detector similar to the far-IR detector
- embedding the detector into an optical stack that increases optical coupling to free space. This technique has shown to greatly increase the absorption efficiency for TiN [48].
- increasing the structure size of the IDC in the near-IR design similar to the far-IR design. This will lower TLS noise.
- redesigning the lens for the mid-IR. The currently used fused silica has poor transmission for wavelengths >4 μm. Materials like ZnSe and KBr have much better transmission for these wavelengths.
- optimising the Al inductor geometry for the longer wavelengths. Al absorber designs have shown to reach absorbing efficiencies of 70-80% at 10 μm by optimising the shape of the meandering inductor [23].
- implementing parallel plate capacitors (PPCs). Research into PPCs is relevant as they are a much smaller alternative for IDCs. Large IDCs will reduce the response by diluting the kinetic induction fraction. PPCs can in theory However, PPCs also tend to increase the TLS noise [56].

Bibliography

[1] National Academies of Sciences, Engineering and Medicine, *Pathways to discovery in astronomy and astrophysics for the 2020s.* Washington, DC: The National Academies Press, 2021, (2-18)–(2-20).

[2] A. Wolszczan and D. A. Frail, "A planetary system around the millisecond pulsar PSR1257+12," *Nature*, vol. 355, pp. 145–147, 1992.

[3] "NASA Exoplanet Archive." (2022), [Online]. Available: `https://exoplanetarchive.ipac.caltech.edu/index.html` (visited on 10/01/2022).

[4] N. M. Batalha, "Exploring exoplanet populations with NASA's Kepler Mission," *Proceedings of the National Academy of Sciences*, vol. 111, no. 35, pp. 12 647–12 654, 2014.

[5] E. A. Petigura, A. W. Howard, and G. W. Marcy, "Prevalence of Earth-size planets orbiting Sun-like stars," *Proceedings of the National Academy of Sciences*, vol. 110, no. 48, pp. 19 273–19 278, 2013.

[6] A. Silburt, E. Gaidos, and Y. Wu, "A statistical reconstruction of the planet population around Kepler solar-type stars," *The Astrophysical Journal*, vol. 799, no. 2, p. 180, 2015.

[7] B. S. Gaudi, S. Seager, B. Mennesson, and et al., "Habitable Exoplanet Observatory (HabEx) Mission Concept Study Final Report," Tech. Rep., 2020.

[8] The LUVOIR Team, "The LUVOIR Mission Concept Study Final Report," Tech. Rep., 2019.

[9] S. P. Quanz, M. Ottiger, E. Fontanet, *et al.*, "Large Interferometer For Exoplanets (LIFE): I. Improved exoplanet detection yield estimates for a large mid-infrared space-interferometer mission," *arXiv preprint arXiv:2101.07500*, 2021.

[10] F. Dannert, M. Ottiger, S. P. Quanz, *et al.*, "Large Interferometer For Exoplanets (LIFE): II. Signal simulation, signal extraction, and fundamental exoplanet parameters," *Astronomy & Astrophysics*, vol. 664, no. A22, 2022.

[11] B. S. Konrad, E. Alei, D. Angerhausen, *et al.*, "Large Interferometer For Exoplanets (LIFE): III. Spectral resolution, wavelength range and sensitivity requirements based on atmospheric retrieval analyses of an exo-Earth," Tech. Rep., 2021.

[12] J. Kammerer, S. P. Quanz, F. Dannert, *et al.*, "Large Interferometer For Exoplanets (LIFE): VIII. Detecting rocky exoplanets in the habitable zones of Sun-like stars," *arXiv preprint arXiv:2210.01782*, 2022.

[13] A. Endo, K. Karatsu, Y. Tamura, *et al.*, "First light demonstration of the integrated superconducting spectrometer," *Nature Astronomy 2019*, vol. 3, no. 11, pp. 989–996, 2019.

[14] A. Monfardini, A. Benoit, A. Bideaud, *et al.*, "A dual-band millimeter-wave kinetic inductance camera for the iram 30 m telescope," *Astrophysical Journal, Supplement Series*, vol. 194, no. 2, 2011.

[15] J. Baselmans, J. Bueno, S. J. Yates, *et al.*, "A kilo-pixel imaging system for future space based far-infrared observatories using microwave kinetic inductance detectors," *Astronomy & Astrophysics*, vol. 601, A89, 2017.

[16] J. J. A. Baselmans, F. Facchin, A. P. Laguna, *et al.*, "Ultra-sensitive THz microwave kinetic inductance detectors for future space telescopes," *Astronomy & Astrophysics*, vol. 665, A17, 2022.

[17] P. J. De Visser, S. A. De Rooij, V. Murugesan, D. J. Thoen, and J. J. Baselmans, "Phonon-Trapping-Enhanced Energy Resolution in Superconducting Single-Photon Detectors," *Physical Review Applied*, vol. 16, no. 3, 2021.

[18] K. Kouwenhoven, D. Fan, E. Biancalani, *et al.*, "Resolving Power of Visible to Near-Infrared Hybrid β-Ta/NbTiN Kinetic Inductance Detectors," *arXiv preprint arXiv:2207.05534*, 2022.

[19] A. B. Walter, N. Fruitwala, S. Steiger, *et al.*, "The MKID exoplanet camera for Subaru SCExAO," *Publications of the Astronomical Society of the Pacific*, vol. 132:125005, no. 1018, 2020.

[20] S. R. Meeker, B. A. Mazin, A. B. Walter, *et al.*, "DARKNESS: a microwave kinetic inductance detector integral field spectrograph for high-contrast astronomy," *Publications of the Astronomical Society of the Pacific*, vol. 130:065001, no. 988, 2018.

[21] B. A. Mazin, S. R. Meeker, M. J. Strader, *et al.*, "ARCONS: A 2024 Pixel Optical through Near-IR Cryogenic Imaging Spectrophotometer," *Publications of the Astronomical Society of the Pacific*, vol. 125, no. 933, pp. 1348–1361, 2013.

[22] L. Novotny, P. Bharadwaj, and B. Deutsch, "Optical Antennas," *Advances in Optics and Photonics, Vol. 1, Issue 3, pp. 438-483*, vol. 1, no. 3, pp. 438–483, 2009.

[23] J. Perido, J. Glenn, P. Day, *et al.*, "Extending KIDs to the Mid-IR for Future Space and Suborbital Observatories," *Journal of Low Temperature Physics*, vol. 199, no. 3-4, pp. 696–703, 2020.

[24] J. Baselmans, *internal communications*.

[25] T. Currie, B. Biller, A.-M. Lagrange, *et al.*, "Direct Imaging and Spectroscopy of Extrasolar Planets," *arXiv preprint arXiv:2205.05696*, 2022.

[26] F. Selsis, L. Kaltenegger, and J. Paillet, "Terrestrial exoplanets: diversity, habitability and characterization," *Physica Scripta*, vol. 2008:014032, no. T130, 2008.

[27] L. Kaltenegger, "How to characterize habitable worlds and signs of life," *Annual Review of Astronomy and Astrophysics*, vol. 55, pp. 433–485, 2017.

[28] R. N. Bracewell, "Detecting Nonsolar Planets by Spinning Infrared Interferometer," *Nature*, vol. 274, pp. 780–781, 1978.

[29] P. Jerram and J. Beletic, "Teledyne's high performance infrared detectors for space missions," in *International Conference on Space Optics—ICSO 2018*, SPIE, vol. 11180, 2019, pp. 1270–1279.

[30] D. B. Reynolds, D. H. Seib, S. B. Stetson, T. Herter, N. Rowlands, and J. Schoenwald, "Blocked impurity band hybrid infrared focal plane arrays for astronomy," *IEEE Transactions on Nuclear Science*, vol. 36, no. 1, pp. 857–862, 1989.

[31] T. L. Roellig, C. W. McMurtry, T. P. Greene, T. Matsuo, I. Sakon, and J. G. Staguhn, "Mid-infrared detector development for the Origins Space Telescope," *Journal of Astronomical Telescopes, Instruments, and Systems*, vol. 6:041503, no. 4, 2020.

[32] M. E. Ressler, H. Cho, R. A. Lee, *et al.*, "Performance of the JWST/MIRI Si: As detectors," in *High Energy, Optical, and Infrared Detectors for Astronomy III*, SPIE, vol. 7021, 2008, pp. 224–235.

[33] M. Dorn, C. McMurtry, J. Pipher, *et al.*, "A monolithic 2k x 2k LWIR HgCdTe detector array for passively cooled space missions," in *High Energy, Optical, and Infrared Detectors for Astronomy VIII*, SPIE, vol. 10709, 2018, pp. 52–60.

[34] M. S. Cabrera, C. W. McMurtry, W. J. Forrest, J. L. Pipher, M. L. Dorn, and D. L. Lee, "Characterization of a 15-μm cutoff HgCdTe detector array for astronomy," *Journal of Astronomical Telescopes, Instruments, and Systems*, vol. 6:011004, no. 1, 2019.

[35] R. Barends, "Photon-detecting superconducting resonators," PhD thesis, Delft University of Technology, 2009.

[36] J. Gao, J. Zmuidzinas, A. Vayonakis, P. Day, B. Mazin, and H. Leduc, "Equivalence of the Effects on the Complex Conductivity of Superconductor due to Temperature Change and External Pair Breaking," *Journal of Low Temperature Physics 2008 151:1*, vol. 151, no. 1, pp. 557–563, 2008.

[37] R. L. Kautz, "Picosecond pulses on superconducting striplines," *Journal of Applied Physics*, vol. 49, no. 1, pp. 308–314, 1978.

[38] B. A. Mazin, "Microwave kinetic inductance detectors," PhD thesis, California Institute of Technology, 2005.

[39] P. De Visser, "Quasiparticle dynamics in aluminium superconducting microwave resonators," PhD thesis, Delft University of Technology, 2014.

[40] A. Kozorezov, A. Volkov, J. Wigmore, A. Peacock, A. Poelaert, and R. den Hartog, “Quasiparticle-phonon downconversion in nonequilibrium superconductors,” *Physical Review B*, vol. 61:11807, no. 17, 2000.

[41] U. Fano, “Ionization Yield of Radiations. II. The Fluctuations of the Number of Ions,” *Physical Review*, vol. 72, no. 1, p. 26, 1947.

[42] A. G. Kozorezov, J. K. Wigmore, D. Martin, P. Verhoeve, and A. Peacock, “Electron energy down-conversion in thin superconducting films,” *Physical Review B - Condensed Matter and Materials Physics*, vol. 75:094513, no. 9, 2007.

[43] N. Zobrist, N. Klimovich, B. Eom, *et al.*, “Improving the dynamic range of single photon counting kinetic inductance detectors,” *Journal of Astronomical Telescopes, Instruments, and Systems*, vol. 7:010501, no. 1, 2021.

[44] C. Müller, J. H. Cole, and J. Lisenfeld, “Towards understanding two-level-systems in amorphous solids: insights from quantum circuits,” *Reports on Progress in Physics*, vol. 82, no. 12, p. 124 501, 2019.

[45] “THz Materials.” (2022), [Online]. Available: `https://www.tydexoptics.com/products/thz_optics/thz_materials/` (visited on 11/07/2022).

[46] I. A. Kaplunov, A. I. Kolesnikov, G. I. Kropotov, and V. E. Rogalin, “Optical Properties of Single-Crystal Germanium in the THz Range,” *Optics and Spectroscopy*, vol. 126, no. 3, pp. 271–274, 2019.

[47] I. A. Kaplunov, G. I. Kropotov, V. E. Rogalin, and A. A. Shakhmin, “Optical properties of some crystalline fluorides in the terahertz region of the spectrum,” *Optical Materials*, vol. 115:111019, 2021.

[48] S. Hähnle, K. Kouwenhoven, B. Buijtendorp, *et al.*, “Superconducting Microstrip Losses at Microwave and Submillimeter Wavelengths,” *Physical Review Applied*, vol. 16:014019, no. 1, 2021.

[49] K. D. Irwin, “Phonon-mediated particle detection using superconducting tungsten transition-edge sensors,” PhD thesis, Stanford University, 1995.

[50] A. Szymkowiak, R. Kelley, S. Moseley, and C. Stahle, “Signal processing for microcalorimeters,” *Journal of Low Temperature Physics*, vol. 93, no. 3, pp. 281–285, 1993.

[51] P. Welch, “The use of fast Fourier transform for the estimation of power spectra: A method based on time averaging over short, modified periodograms,” *IEEE Transactions on Audio and Electroacoustics*, vol. 15, no. 2, pp. 70–73, 1967.

[52] N. R. Zobrist, “Improving the Resolving Power of Ultraviolet to Near-Infrared Microwave Kinetic Inductance Detectors,” PhD thesis, University of California, Santa Barbara, 2022.

[53] H. Shimazaki and S. Shinomoto, “A Method for Selecting the Bin Size of a Time Histogram,” *Neural Computation*, vol. 19, no. 6, pp. 1503–1527, 2007.

[54] S. Moseley, J. C. Mather, and D. McCammon, “Thermal detectors as x-ray spectrometers,” *Journal of Applied Physics*, vol. 56, no. 5, pp. 1257–1262, 1984.

[55] M. E. Eckart, “Measurements of X-ray selected agn and novel superconducting X-ray detectors,” PhD thesis, California Institute of Technology, 2007.

[56] P. De Visser, *internal communications*.

[57] S. de Rooij, “Quasiparticle Dynamics in Optical MKIDs: Single Photon Response and Temperture Dependent Generation-Recombination Noise,” MSc thesis, 2020.

[58] S. A. De Rooij, J. J. Baselmans, V. Murugesan, D. J. Thoen, and P. J. De Visser, “Strong reduction of quasiparticle fluctuations in a superconductor due to decoupling of the quasiparticle number and lifetime,” *Physical Review B*, vol. 104:L180506, no. 18, 2021.

[59] J. R. Clem and K. K. Berggren, “Geometry-dependent critical currents in superconducting nanocircuits,” *Physical Review B*, vol. 84:174510, 2011.

[60] A. J. Annunziata, D. F. Santavicca, L. Frunzio, *et al.*, “Tunable superconducting nanoinductors,” *Nanotechnology*, vol. 21, no. 44, 2010.

[61] P. D. Mauskopf, “Transition Edge Sensors and Kinetic Inductance Detectors in Astronomical Instruments,” *Publications of the Astronomical Society of the Pacific*, vol. 130:082001, 2018.

[62] R. Igreja and C. Dias, “Analytical evaluation of the interdigital electrodes capacitance for a multilayered structure,” *Sensors and Actuators A: Physical*, vol. 112, no. 2-3, pp. 291–301, 2004.

[63] C. R. Paul, *Inductance: Loop and Partial*. John Wiley & Sons, 2011.